UNIVERSITY OF CALIFORNIA, IRVINE

Enhanced Detection of Drug-induced Cardiotoxicity in Human Stem Cell-Derived Cardiomyocytes Using Optical Flow, Biomimetic Substrates, and Machine Learning

DISSERTATION

submitted in partial satisfaction of the requirements for the degree of

DOCTOR OF PHILSOPHY

in Biomedical Engineering

by

Eugene Lee

Dissertation Committee:
Professor Michelle Khine, Chair
Assistant Professor Anna Grosberg
Professor William C. Tang

2017

DEDICATION

To

My parents Hua Chau Lee and Meh Whei Pan

Table of Contents

LIST OF FIGURES

LIST OF TABLES

ACKNOWLEDGEMENTS

I would like to express my deepest gratitude to my academic advisor Professor Michelle Khine for all of her guidance and support throughout my graduate studies. Michelle is the epitome of a natural leader as she greatly and constantly inspires those around her. She has fostered an atmosphere of creativity, passion, and open-mindedness in the lab. But most importantly, she genuinely cares about her students' well-being and future. I cannot think of a time where she was not available when I needed her advice. I feel truly honored to be a member of the Khine lab.

I would like to thank all of my committee members: Dr. Anna Grosberg, Dr. Aaron P. Esser-Kahn, Dr. Elizabeth Read, Dr. Peter Taborek, and Dr.William C. Tang. They have provided advice, constructive criticism, and thoughtful advice on my work. In addition, I would like to thank all of my collaborators: Dr. Risi Kondor for introducing me to the field of machine learning, Dr. Steven C. George and Yosuke Kurokowa for our project in comapring brightfield and machine learning to fluorescence-based methods, Dr Ulric J. Lund and Robin Tu for their advice in statistics, Dr. Ronald A. Li, Dr. Kevin Costa, and Dr. David Tran for our projects including the creation of drug models to predict a cardioactive compound's mechanistic action.

I would like to thank all the members of the Khine lab past and present. I am extremely grateful to Dr. Aaron Chen for introducing me to the stem cell thrust of the lab and encouraging me to pursue my graduate studies in this field. I would also like to recognize all of my undergraduates that have helped me through the years: Roger Tu, Kevin Santiago, Nancy Nguyen, Sahil Bahkta, Truc Dinh, and Lucy Zhuang. Lab has always felt like home with my labmates as another family. Besides making scientific advancements, we have had a lot of fun and laughs. I have always benefitted from everybody's perspectives.

I would also like to thank all the friends that I have made during my time at UCI, in particular those in the 2012 incoming BME class. My transition in moving to Irvine from the East coast was made easy by these friends. I hope we continue to carry on our annual traditions and enjoyment of playing quirky games. I am excited for what the future awaits for all of us.

I would like to thank Haiying Wang for her love, support, care, and optimism through the last four years. She has always made me smile, especially through the tough times in research. She continues to broaden my view on life through our many adventures and experiences. Words cannot truly express my utmost appreciation for her; but I know that I cannot wait for all the adventures that lie ahead of us.

Lastly, I would like to express my deepest appreciation and gratitude for my family. I would not have had any of these opportunities if not for my parents and their dedication, sacrifices, and unconditional support. Thank you Mom and Dad. While it is not enough, this thesis and presented work are dedicated to them. I would also like to thank Mr. and Mrs. Pitts for their involvement and impact in my life. I would also like to thank my uncles, aunts, and all my cousins for making my graduate years more light-hearted and enjoyable.

I am truly grateful for all the people I have met along the way. I would not be here today without their help and support.

CURRICULUM VITAE

Eugene Lee

2017 **PhD**, University of California, Irvine
Biomedical Engineering
Thesis: Enhanced Detection of Drug-induced Cardiotoxicity in Human Stem Cell-Derived Cardiomyocytes Using Optical Flow, Biomimetic Substrates, and Machine Learning

2015 **MS**, University of California, Irvine
Biomedical Engineering

2010 **BS**, Johns Hopkins University
Biomedical Engineering

PUBLICATIONS

E.K. Lee[1], D.D. Tran[1], W. Keung, P. Chan, G. Wong, K.D. Costa, R.A. Li, M. Khine **Machine learning of human pluripotent stem cell-derived engineered cardiac tissue contractility for automated drug classification** *In preparation*

E.K. Lee[1], Y. Kurokawa[1], R. Tu, S. George, M. Khine **Machine learning plus optical flow: A simple and sensitive method to detect cardioactive drugs** Scientific Reports. 5(2015)

A. Chen[1], E. Lee[1], R. Tu, K. Santiago, A. Grosberg, C. Fowlkes, M. Khine **Integrated platform for functional monitoring of biomimetic heart sheets from human pluripotent stem cells** Biomaterials. 35(2014)

M. Chu[1], T.T. Nguyen[1], E.K. Lee, J.L. Morival, M. Khine **Plasma free reversible and irreversible microfluidic bonding** Lab on a Chip. 17(2017)

S. Lin, E.K. Lee, N. Nguyen, M. Khine **Thermally-induced miniaturization for micro- and nanofabrication: progress and updates** Lab on a Chip. 14(2014)

J. Nokes, R. Liedert, M. Kim, A. Siddiqui, M. Chu, E.K. Lee, M. Khine **Reduced Blood Coagulation on Roll-to-Roll, Shrink Induced Superhydrophobic Plastics** Advanced Healthcare Materials. 5(2016)

ORAL PRESENTATIONS

E. Lee, A. Wong, L. Zhang, R. Li, M. Khine "Integrating Machine Learning and Biomimetic Wrinkles for High-throughput Screening of Drug-Induced Cardiotoxicity in hPSC-derived Cardiomyocytes," Society for Laboratory Automation and Screening 2016, San Diego, California, January 2016

S. Lin, E. Lee, J. Pegan, H. Sharma, and M. Khine "SMART (Shrink Manufacturing Advanced Research Tools)," Transducers 2015, Anchorage, Alaska, June 2015

E. Lee, Y. Kurokawa, S. George, M. Khine, "Optical Flow Paired with Machine Learning for Increased Detection of Drug-induced Cardiotoxicity in Human Induced Pluripotent Stem Cell Derived Cardiomyocytes," 15th Annual UC Systemwide Bioengineering Symposium, Irvine, California, June 2014

POSTER PRESENTATIONS

E. Lee, Y. Kurokawa, R. Tu, S. George, M. Khine, "Microplatform to Identify Drug-Induced Cardiotoxicity in IPS-Derived Cardiomyocytes with Bright-Field Imaging and Machine Learning," Center for Advanced Design and Manufacturing of Integrated Microfluidics (CADMIM) Annual Meeting, Irvine, California, March 2015

E. Lee, Y. Kurokawa, R. Tu, S. George, M. Khine, "Microplatform to Identify Drug-Induced Cardiotoxicity in IPS-Derived Cardiomyocytes with Bright-Field Imaging and Machine Learning," EMBS Micro and Nanotechnology in Medicine Conference, Oahu, Hawaii, December 2014

E. Lee, Y. Kurokawa, R. Tu, S. George, M. Khine, "Optical Flow Paired with Machine Learning for Increased Detection of Drug-induced Cardiotoxicity in Human Induced Pluripotent Stem Cell Derived Cardiomyocytes," Biomedical Engineering Society, San Antonio, Texas, October 2014

E. Lee, A. Chen, R. Tu, K. Santiago, A. Grosberg, C. Fowlkes, M. Khine, "Platform for Functional Monitoring of Biomimetic Heart Sheets Derived from Human Pluripotent Stem Cells," Center for Advanced Design and Manufacturing of Integrated Microfluidics (CADMIM) Annual Meeting, April 2014

E. Lee, A. Chen, R. Tu, K. Santiago, A. Grosberg, C. Fowlkes, M. Khine, "Platform for Functional Monitoring of Biomimetic Heart Sheets Derived from Human Pluripotent Stem Cells," 1st Annual Unmet Clinical Needs in Cardiovascular Medicine Symposium, Irvine, California, November 2013

HONORS AND AWARDS

2016 Tony B. Academic Travel Award, Society for Laboratory Automation and Screening Conference
2014 Honorable Mention, NSF Graduate Research Fellowship
2014 2nd place, Beall Student Design Competition, UCI
2014 Reviewer's Choice award: Poster Presentation, Biomedical Engineering Society Conference
2014 Most Fundable Venture, Paul Merage School of Business Plan Competition, UCI
2014 Finalist, Orange County Social Entrepreneurship
2013 Fellow, Cardiovascular Applied Research and Entrepreneurship Training Program (NHLBI T32)

ABSTRACT OF THE DISSERTATION

Enhanced Detection of Drug-induced Cardiotoxicity in Human Stem Cell-Derived Cardiomyocytes Using Optical Flow, Biomimetic Substrates, and Machine Learning

by

Eugene Lee

Doctor of Philosophy in Biomedical Engineering

University of California, Irvine, 2017

Professor Michelle Khine, Chair

Current preclinical screening methods are ineffective at detecting cardiotoxicity: 30% of drug attritions are attributed to drug-induced cardiotoxicity. With recent advancements in stem cell technologies, human pluripotent stem cells-derived cardiomyocytes (hPSC-CM) can now provide a physiologically relevant *in vitro* model of the myocardium. Availability of such cells has led to the emergence of various platforms that utilize them. However, current platforms still encounter challenges that deter their adoption for commercial use. One issue is hPSC-CMs exhibit fetal-like phenotypes; screening with them leads to unpredictable results that don't accurately represent cardiotoxicity in adults. Another persistent challenge is the need to develop a simple and reliable method to measure key electrophysiological and contractile parameters. In addition, analytical approaches need to be created for accurate and automated detection of cardiotoxicity from platform readouts. In this thesis, strategies that collectively form a platform are described to address these issues.

Alignment of hPSC-CMs has been shown to regulate sarcomere orientation, produce stronger contractile forces, and cause anisotropic action potential propagation. We demonstrate that biomimetic substrates with topographical alignment cues (uniaxial and multi-scale 'wrinkles') can be fabricated by using pre-stressed thermoplastic shrink film. These wrinkles recapitulate the anisotropic nature of the

ECM of the native myocardium. When aligned on these substrates, hPSC-CMs exhibited a more sensitive response to cardioactive compounds than their unaligned counterparts.

Using brightfield microscopy and optical flow, contractility of hPSC-CMs exposed to compounds can be monitored in a non-invasive and inexpensive manner. Furthermore this brightfield technique was readily applied to cardiac constructs of various tissue geometries, ranging from 2D monolayers to 3D cardiac organoids. For improved and automated analysis, we mated the brightfield technique with supervised machine learning. The machine learning provides a singular quantitative index that summarizes the impact of multiple parameters, and thus simplifies the assessment of drug effects on hPSC-CMs. Through the evaluation of several cardioactive drugs with dissimilar effects, this paired method was comparable – and even superior to – a fluorescence-based detection scheme common in commercially available systems. The machine learning was further leveraged for the analysis of a cardiac tissue strip platform. A model of drug classes was created and successfully predicted the mechanistic action of an unknown cardioactive compound.

CHAPTER 1: Introduction

1.1 Motivation

The current state of drug development is inefficient, prolonged, and costly. Only 1 out of every 5,000 compounds available at the drug discovery stage will achieve Food & Drug Administration (FDA) approval, which averages about 14 years at a cost of $1.5 billion.[1] A significant proportion of the overall cost for drug development is attributed to withdrawal of drugs in clinical phases or post-FDA approval, 30% of which is related to cardiotoxicity.[2] For example, the diuretic drug cisapride's undetected cardiotoxic effects resulted in 175 deaths and 386 cases of serious ventricular arrhythmia before it was removed from the market in 2000.[3] This suggests that the current methods of drug screening for detecting cardiotoxicity are ineffective.

The advent of human pluripotent stem cell-derived cardiomyocytes (hPSC-CMs) creates the possibility of a better in vitro model of the human myocardium for various applications including drug screening.[4–7] However human pluripotent stem cell-derived cardiomyocytes (hPSC-CM) exhibit embryonic-like phenotypes in terms of electrophysiological properties, contractility, and structural development.[8,9] Different phenotypes may result in disparate drug responses and affect the accuracy of hPSC-CM as an in vitro model.

Another challenge in the adoption of hPSC-CMs for drug screening purposes is the shortcomings of current detection assays. Invasive methods, such as patch clamping, are traditionally limited to single cell analysis, and have proven difficult for high-throughput applications. Attempts to incorporate patch-clamping into high-throughput and commercial use are limited by cell membrane quality.[10] In addition, the instability of the seals prevents extended or longitudinal studies.[11,12] Fluorescence-based optical methods such as voltage and calcium sensitive dyes provide non-invasive means to observe electrophysiological properties of hPSC-

CMs.[13] However, these dyes can impact cell function, and therefore are not suitable for prolonged studies. Furthermore, both dyes and genetically encoded indicators are subject to photobleaching effects.[14,15] Microelectrode arrays (MEA) have high-throughput capabilities, but require a cluster of CMs for accurate electrical signals.[16,17] Similarly, impedance-based measurements offer non-invasive, high-throughput methods of drug screening, but are limited to monolayer cell cultures.[18,19]

While these methods of operation may vary, the readouts of systems are predominantly composed of an array of parameters that describe the behavior or shape of individual contractile events. Combining this with the number of experimental conditions (e.g. various pacing frequencies or drug concentrations) can yield high-dimensional datasets that make it difficult to draw comprehensive conclusions. In addition, as these platforms are meant for high-throughput use, the analysis needs to be automated. Such requirements indicate that traditional methods of pre-selecting one or a few parameters for statistical analysis may not be adequate. By selectively examining a few parameters independently of one another, there is a risk of not detecting information that differentiates the behavior of normal hPSC-CMs from those exposed to cardioactive compounds. Thus, this works aims to enhance the detection of drug-induced cardiotoxicity in hPSC-CMs by addressing the challenges faced by current screening platforms.

1.2 Overview of dissertation

The dissertation is structured as follows. Chapter 2 highlights the combination of brightfield microscopy, optical flow and post-processing techniques to monitor contractile behavior of cardiomyocytes when exposed to cardioactive compounds. In Chapter 3, the effects of biomimetic wrinkled substrates on cell alignment and hPSC-CM response to cardioactive

compounds are discussed. In Chapter 4, we demonstrate a method to adapt the brightfield technique and biomimetic substrates for high-throughput capabilities. This method entails a chemical approach that patterns multiple islands of cardiomyocytes onto the surface of a single substrate. Chapter 5 examines the application of supervised machine learning, in particular Support Vector Machines, to the automated analysis of data generated from cardiotoxicity screening platforms. The algorithms are able to determine if a compound is cardioactive and also, create a drug classification model that can predict an unknown cardoactive compound's mechanistic action. In Chapter 6, the brightfield technique is applied to 3D cardiac organoids and provides spatial information that is not available in current pressure readouts. This information may be beneficial in the screening of compounds that disrupt electrical propagation on cardiac surfaces. We conclude with a discussion of future directions of this work in Chapter 7.

CHAPTER 2: Brightfield acquisition of human stem cell-derived cardiomyocytes

2.1 Introduction

The shortcomings of current assays to quantify contractile behavior of cardiomyocytes have been one of main challenges in the adoption of human pluripotent stem cell-derived cardiomyocytes (hPSC-CMs) for the screening of drug-induced cardiotoxicity. Brightfield microscopy provides a possible solution as it is non-invasive and allows for long-term monitoring of cardiomyocytes. In addition, brightfield acquisition requires minimal and inexpensive equipment that is suitable for high-throughput use. The concept of using image-based analysis to quantify cardiomyocyte beating dynamics has been explored by various research groups.[7,20,21] However, these studies have all required the need for custom cell culture apparatuses. More recently, research groups have investigated brightfield-based methods that are widely applicable to both standard cell culture apparatuses, such as a 384-well cell culture plates, and custom ones.[22–29] These respective methods have all demonstrated the feasibility of tracking the contractile behavior of cardiomyocytes and extracting out quantitative parameters to describe the apparent motion. Maddah *et al*. validated the practicability of using brightfield microscropy to monitor contractile behavior of cardiomyocytes in various setups: monolayer, cardiosphere and single cell.[30] There are primarily two strategies in achieving image-based analysis: (i) methods that derive signals based on pixel differences or derivatives between frames and (ii) methods that derive signals based on generated motion vectors.

Our platform leverages the benefits of brightfield microscopy and employs a vector-based analysis, optical flow paired with post processing techniques. The rationale behind this

choice will be apparent in the following sections of this chapter. In addition, this chapter will explore two post processing techniques to augment the information derived from the optical flow-generated vectors. Lastly, our brightfield technique does not require custom cell culture apparatuses and can be applied to various tissue formats, ranging from monolayers to 3D cardiac models.

2.2 Optical flow

Optical flow is often defined as the distribution of apparent velocities of the brightness patterns of an image. When applied to a video or sequences of image frames, velocities of objects in the video can be estimated. Optical flow makes two key assumptions: 1) apparent brightness of moving objects is constant between frames and 2) the movement of each image pixel is small.[31] Based on those assumptions, in a regular two dimensional image, the image brightness constancy equation (**Eq. 1**) can be derived:

$$\boldsymbol{I(x, y, t) = I(x + \Delta x,\ y + \Delta y, t + \Delta t)} \qquad (1)$$

$\boldsymbol{I}$ represents the intensity.

Given the intensity is constant, the total derivative of **Eq 1** can be set to 0, resulting in **Eq. 2**:

$$\boldsymbol{\frac{dI(x(t),y(t),t)}{dt} = \frac{\partial I}{\partial x}\frac{dx}{dt} + \frac{\partial I}{\partial y}\frac{dy}{dt} + \frac{\partial I}{\partial t} = 0} \qquad (2)$$

Eq. 2 can be re-written with $\boldsymbol{\frac{\partial I}{\partial x}}$ as $\boldsymbol{I_x}$, $\boldsymbol{\frac{\partial I}{\partial y}}$ as $\boldsymbol{I_y}$, $\boldsymbol{\frac{\partial I}{\partial t}}$ as $\boldsymbol{I_t}$, $\boldsymbol{\frac{dx}{dt}}$ as u, and $\boldsymbol{\frac{dy}{dt}}$ as v (**Eq. 3**)

$$\boldsymbol{I_x u + I_y v + I_t = 0} \qquad (3)$$

Where u and v represent the displacement or vector in the x- and y-direction.

As seen in **Eq. 3**, u and v represent two unknown variables that cannot be solved with only one equation. Another constraint or equation would be necessary. This requirement is commonly referred to as the aperture problem.[32]

One of the most common solutions to the aperture problem is using the Horn-Schunck (HS) method.[33] The HS method assumes smoothness among the image, meaning that areas of a moving object will tend to move together. As a result, optical flow fields with small gradients should be preferred to those with large gradients or distortions in the image. This is primarily implemented with introducing two energy terms: e_s as departure from smoothness and e_c as the optical flow constraint equation term. The goal of the HS method is then to minimize the linear combination of $e_s + \lambda e_c$ in order to solve for u and v, the optical flow field.

2.3 Quantification of contractile behavior

2.3.1 Optical flow analysis

To demonstrate the use of optical flow in quantifying contractile behavior of hPSC-CMs, brightfield videos of monolayer cardiomyocytes in an open perfusion microincubator were captured with QIClick CCD camera under two conditions: 1) 7 frames per second (fps) at a resolution of 1392x1040 pixels and 2) 20 fps at a resolution of 696x520 pixels. The images of the videos were then processed with an optical flow algorithm, which generated vectors that were representative of the hPSC-CM motion.[34,35] The implemented optical flow algorithm was developed by Sun et al. and is based on the Horn-Schunck method described in Section 2.2. The algorithm resulted from the optimization of the HS method with the combination of common image processing techniques. Sun et al. showed that the HS method could be improved by three modifications: 1) changing the penalty function from HS penalty, $\rho(x) = x^2$ to the Charbonnier

penalty, $\rho(x) = (x^2 + \epsilon^2)^{\alpha}$, where $\alpha \leq 0.5$, 2) implementing a spline-based interpolation scheme and 3) using a median filter that examines and incorporates non-local terms.[34]

When the magnitudes of the generated vectors were plotted over time, the vectors were able to capture both the contraction and relaxation phase of a contractile event. For each beat, there were two distinct peaks that were followed by a resting phase if the beating frequency was low enough. To ensure that optical flow and its generated vector could assess changes to contractile behavior of cardiomyocytes, human embryonic stem cell-derived cardiomyocytes (hESC-CMs) were exposed to E-4031, a known human Ether-à-go-go-Related (hERG) K^+ channel blocker. The plot of vectors' normalized displacements (relative magnitude) distinctly showed a delayed extension of specifically the relaxation phase when 30 nM of E-4031 was administered to hESC-CMs (**Figure 2.1 A**). This extension was expected as the inhibition of the hERG K^+ channel, which contributes to the rapid repolarization of the cardiomyocytes, prolongs the QT interval.[35]

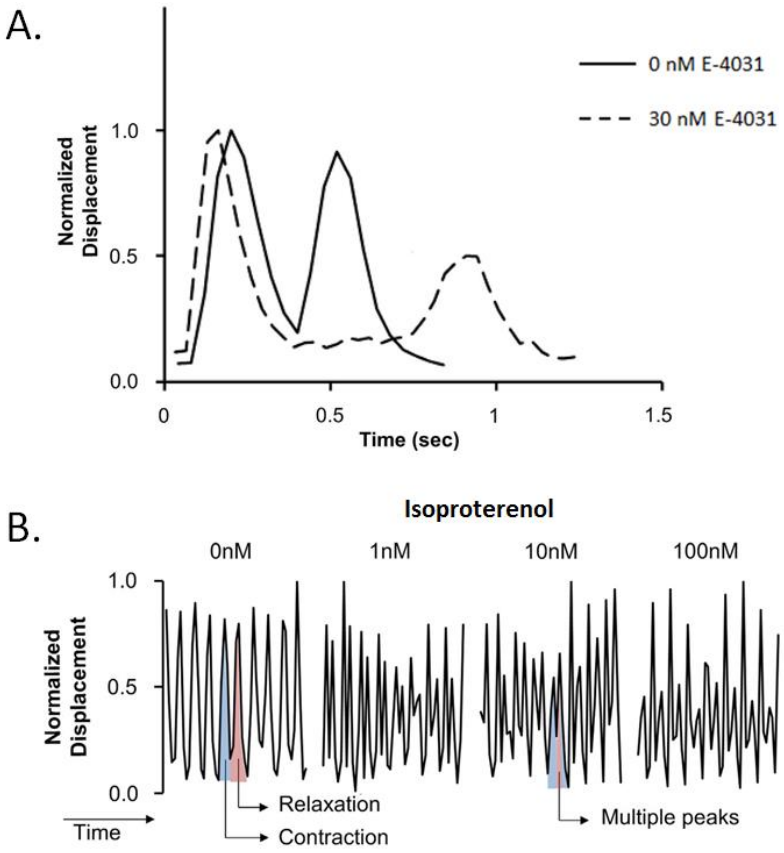

Figure 2.1 Optical flow vectors capturing cardioactive effects. A) Drug screen of E-4031, a potassium channel blocker known for prolonging the QT interval by delaying the rapid repolarization in cardiomyocytes. Solid line is without E-4031, and dashed line is with 30 nm of E-4031. An extended relaxation curve was seen when 30 nM of E-4031 was applied. B) Drug screen of isoproterenol, a β-adrenergic agonist. The blue color represents contraction peak, and red color represents relaxation peak. At higher concentrations of isoproterenol, such as 10 nM, multiple phases were embedded within a perceived singular peak.

2.3.2 Post optical flow contraction analysis

As a means to quantify matrices containing the x- and y-axis components of generated vectors and subsequent changes to hPSC-CMs when exposed to cardioactive compounds, an in-house MATLAB software was created for post optical flow contraction (pOFC) analysis. The goal of the software was to compute duration, frequency, synchronicity, orientation, and acceleration of each contraction or contractile event.

To begin this post optical flow contraction (pOFC) analysis, the user will need to input a noise threshold, degree of error, time interval, and starting frame number into the guided user interface. The noise threshold refers to the cutoff value; if the maximum value in the grid of cells is below the cutoff, it is considered to be noise, and is assigned a value of zero. As seen in **Figure 2.2A**, the degree of error represents the flexibility in determining the stage of a contraction (i.e. contraction vs. relaxation). The time interval is the time between each consecutive frame. The starting frame number allows user to eliminate partial contractions.

After the inputs have been submitted, the software calculates the occurrences of contraction and relaxation in each individual grid for the entire movie duration. Instead of the magnitude values, categorical variables are used when determining the number of contraction and relaxation occurrences in each grid. The cells within the grids are either contracting (represented by a value of 1), relaxing (a value of −1), or at rest (a value of 0). To determine when cells are at rest, a resting threshold is calculated for each individual grid using the following equation: Resting Threshold = Minimum Trough + 0.25 × (Maximum Peak − Minimum Trough). If the magnitude vector for a given time frame in a grid is below the resting threshold, then the cells within that grid for that specific time frame are deemed at rest. With the input of the starting frame number, the software searches for the first sign of a contraction and assigns the grid a value of 1 for that time frame. The vector direction of the same grid in subsequent time intervals is then compared to the previous time interval. If the direction of the vector is opposite of that in the previous frame and within the degree of error, and has a magnitude value above resting threshold, the cells in the grid are identified as in the relaxing stage, a value of −1.

A complete occurrence is defined as a contraction, relaxation and resting phase in sequence for each grid. If a grid does not have a complete occurrence throughout the entire video acquisition, then the grid is deemed insignificant and not considered in any of the calculations. The grid size is set such that any local cluster of beating cells is represented by multiple grids. After the software converts all grids into categorical values and filters out insignificant grids, the average duration and average frequency of each grid are calculated (**Figure 2.2B**). The frequency is defined as the number of complete occurrences per second. The duration of a complete occurrence is defined as the time between the first time interval where contraction occurs and the last time interval that exhibits relaxation. The software measures synchronicity among the occurrences of grids with the phase difference analysis. This analysis is done by taking the most popular pattern of occurrences and calculating the difference between this pattern and all the other patterns. The orientation of the grids is measured by computing the ratio between the sum of magnitudes for all y-axis components (of optical flow vectors) and the sum of magnitudes of all x-axis components over all time frames. The software also determines the acceleration of each grid by calculating the change of displacement over the change of time.

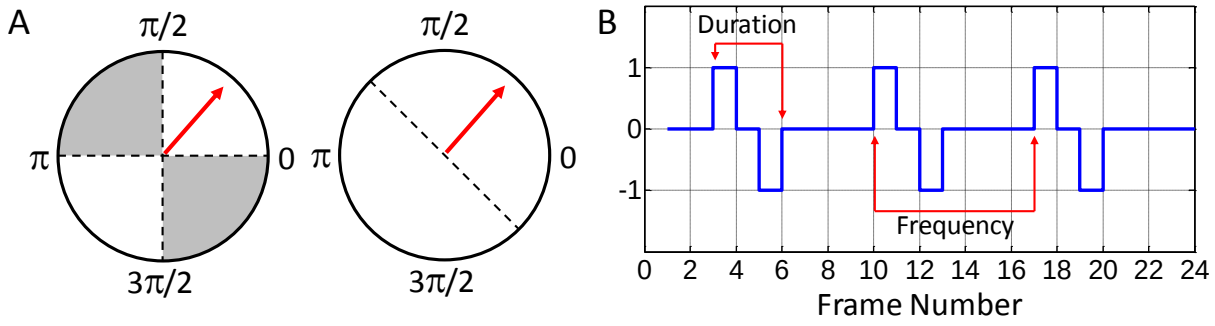

Figure 2.2 Post optical flow contraction analysis. A) Degree of error represents the flexibility in determining whether a subsequent contraction/expansion occurrence has the same or opposite direction of the reference vector, the previous occurrence, or is simply noise. The direction of all vectors is represented by plotting the real parts of arctangent of the x- and y-vectors on a unit circle. For example, if the degree of error is π/4 (right image in A) and the reference vector (RV) indicated in red represents a grid in the contraction stage, a subsequent vector (SV) that represents the next time frame and is in the direct opposite quadrant would mean the grid is now in the relaxation stage (assuming all values are

above resting threshold). However, if the SV lies in the gray quadrants, they are deemed noise. If the s.v. is in the same quadrant as the RV, then the grid is still in the contraction phase. For a degree of error of $\pi/2$ (left image in A), SVs have to be regarded as the same or opposite when compared to the RVs. All analysis performed in this paper uses a degree of error of $\pi/2$. B) A cell contraction and relaxation plot using categorical variables (contractions =1; rest = 0; relaxations = -1).The duration of a complete occurrence is measured by the number of time intervals in between the first time interval that exhibits contraction and the last time interval that exhibits relaxation prior to the resting phase. The frequency is defined as the number of complete occurrences per second. This value is derived by taking the inverse of the time difference between the first time interval of a complete occurrence and the first time interval of the subsequent complete occurrence. However, it should be noted that if there are *n* complete occurrence within a grid, only *n-1* frequencies can be calculated. The frequency of the last complete occurrence cannot be calculated as the start of the subsequent occurrence is unknown.

2.4 Principal component analysis

2.4.1 Motivation

Solely looking at change in the magnitude of vectors has limitations in characterizing the contractile behavior of hPSC-CMs. One of the main shortcomings is that multiple phases of the cardiomyocyte contraction can embedded within a single peak in the average vector displacement trace. This exact scenario was seen when a monolayer of hESC-CMs was exposed to isoproterenol, a β-adrenergic agonist (**Figure 2.1B).** Upon the administration of 10 nM of isoproterenol, one of the corresponding peaks in the normalized displacement (change in magnitude of vectors) had multiple phases within it.[35] This issue was resolved by using the aforementioned post-processing analysis in Section 2.3, which leveraged the change in vector orientation to correctly categorize each data point into one of three states: contraction, relaxation, or resting phase. However using categorical variables combined with user-dependent thresholds, noise and degree of error, there is a possibility of oversimplifying and distorting the original signal, resulting in the abnormal contractile behavior of hPSC-CMs being overlooked. Hence, additional post optical flow processing techniques were explored.

2.4.3 PCA background

Principal component analysis (PCA) is a statistical technique that can reduce the dimensionality of data sets through the generation of principal components. Each principal component is a linear combination of the data set's variables that accounts for the variance within the data. The first principal component has the maximum variance, while subsequent principal components are uncorrelated to previous components and attempt to account for remaining variation.[36] PCA can be achieved through the eigen-decomposition of the covariance matrix.[37] Assuming the data (*D, which is comprised of a M*x*N* matrix) is centered, the covariance matrix *C* can be calculated (**Eq. 4**):

$$C = \frac{DD^T}{N-1} \quad (4)$$

Once calculated, the eigen-decompostion entails the calculation of the eigenvalues, λ_i, and eigenvectors, v_i, in which the following needs to be satisfied (**Eq. 5**)

$$CV_i = \lambda_i v_i \quad (5)$$

This can be further expressed in a matrix form, where V is the matrix of eigenvectors (**Eq. 6**):

$$CV = V\Lambda \quad (6)$$

in which Λ represents the diagonal matrix of eigenvalues (**Eq. 7**)

$$\Lambda = \begin{pmatrix} \lambda_1 & 0 & 0 & \cdots \\ 0 & \lambda_2 & 0 & \cdots \\ & & \ddots & \\ \cdots & \cdots & 0 & \lambda_N \end{pmatrix} \quad (7)$$

We can then re-write **Eq. 3** as following (**Eq. 8**) where V^T is equal to V^{-1} as C is symmetric.

$$C = V\Lambda V^T \quad (8)$$

To calculate the principal components from this, we can set up our projection matrix, P (**Eq. 9**).

$$P = \begin{pmatrix} v_1^T \\ v_2^T \\ \vdots \\ v_{N-1}^T \end{pmatrix} \quad (9)$$

The principal components will then be the multiplication of P^T to the original data set, in which the corresponding values of k^{th} ($k < N$) principal component will be the k^{th} row of the multiplied matrix.

2.4.4 Implementation of PCA to generated vectors

The issue described in Section 2.4.2. was corrected through the application of PCA on the vectors generated from the optical flow algorithm. This implementation consisted of two primary steps, in which PCA was used initially for spatial analysis of the images. The vectors representing each pixel were first decoupled into their corresponding x-and y-axis components. PCA was then specifically applied to a matrix that consisted of these components over all frames of the video acquisition. The norms of the 1^{st} PCA value were then sorted in order of highest to lowest. The lowest number in the first quartile was then regarded as the mask threshold. As seen in **Figure 2.3A**, this mask segmented regions of interests that had large motion or changes in vector magnitude. This segmentation further increased the signal-to-noise ratio by reducing background noise from non-moving sections. With the regions of interest identified, another PCA was done on the x- and y-axis components with respect to time of the selected area for a temporal analysis. When the norm of the 1^{st} PCA values were plotted out, a contractile profile was generated in which the contraction and relaxation peaks of cardiac beats were automatically discerned without any user input (**Figure 2.3B**).

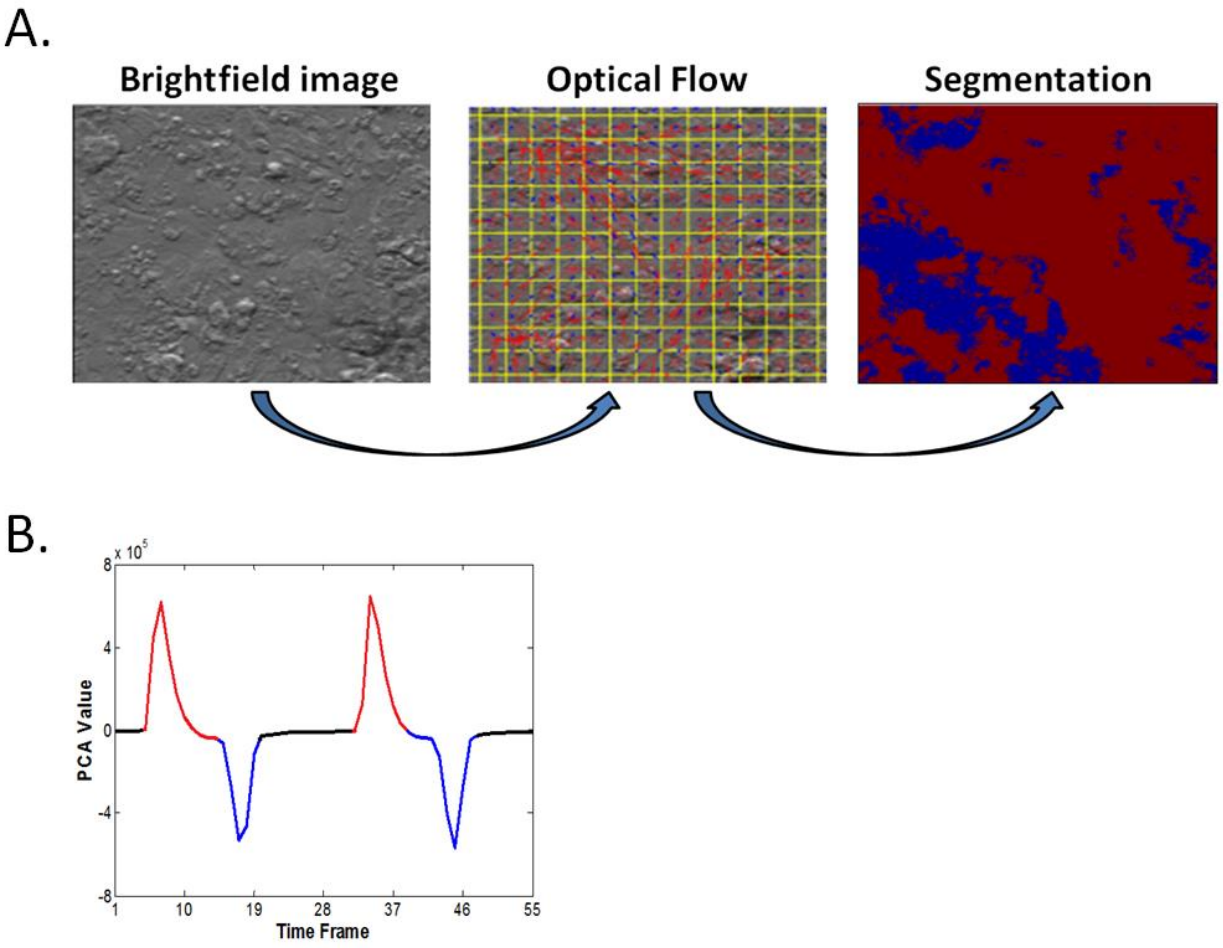

Figure 2.3 Principal component analysis of optical flow vectors A) Brightfield videos of contracting cardiomyocytes are analyzed as images via optical flow. Vectors are generated to represent the motion of the cells. By performing the PCA analysis with respect to the spatial aspect of the videos, a segmentation mask is generated that indicates areas of motion. B) After segmenting regions of interest with the mask, PCA is performed with respect to the temporal aspect of the video. A contractile plot is generated in which the contraction and relaxation phases were automatically discerned (contraction phase indicated in red and positive PCA values and relaxation phase indicated in blue and negative PCA values).

2.5 Summary

In our collective platform, a vector-based strategy using optical flow, was chosen as we have demonstrated that the directional component of a vector can be crucial in the analysis of cardiomyocyte motion. When looking at just the magnitude of pixel differences or vector displacement, a contractile beat is assumed to be represented by two distinct peaks (one representing the contraction phase and one representing relaxation).[26,28] As mentioned previously, the ability to discern between the two phases can be achieved if a resting phase is present. However, if the beating frequency of the cells is increased, multiple phases can be embedded into one singular peak as we have shown (**Figure 2.1B**).[35] Thus, methods that analyze both the magnitude and directional components of vectors should provide more detailed information. The described method of optical flow paired with PCA analysis is able to achieve this in an automated fashion, while requiring minimal equipment. Finally this brightfield method is applicable to longitudinal studies and various experimental designs, ranging from monolayers to 3D cultures (Chapter 6).

CHAPTER 3: Biomimetic materials for maturation of hPSC-CMs

3.1 Introduction

Regardless of methodology to quantify human pluripotent stem cell-derived cardiomyocytes (hPSC-CMs), there is a concern that the immaturity of hPSC-CMs will lead to less-than-perfect predictability of a compound's cardiotoxicity. hPSC-CMs exhibit fetal-like phenotypes, ranging from their gene expression to electrophysiological properties to cell morphology (e.g. lack of T-tubules).[8,9,38–42] Such differences in phenotype have already resulted in disparate effects of cardioactive compounds when comparing *in vitro* data to those of *in vivo*. For example, studies have shown that hPSC-CMs may elicit a minimal to non-existent response to certain positive inotropic compounds, such as beta-adrenergic agonists.[43,44]

As a result, multiple strategies have been employed in hopes of maturing hPSC-CMs for improved detection of cardiotoxicity. Such techniques include electrical stimulation after cardiac differentiation, a tri-culture including fibroblasts and endothelial cells, or the forced expression of selective proteins.[45–48]

A simple and chemical-free approach for hPSC-CM maturation involves the alignment of cardiomyocytes to recapitulate the anisotropic nature of the extracellular matrix (ECM) of the native myocardium. The alignment of hPSC-CMs alone has been shown to align sarcomere structures, produce stronger contractile forces, and cause anisotropic action potential propagation.[20,49] All these changes suggest aligned hPSC-CMs would become more physiologically relevant for drug screening purposes. It should be noted that while the ECM of the native myocardium as a whole possesses an anisotropic nature, there is variability in the spatial arrangement, topography, and fiber bundle thickness among the ECM components. As an example, collagen, one of the most abundant proteins in the ECM, self-assembles fibrils with

diameters on the scale of 20 nm – 1.2 μm. These fibrils continue to form fibers with thicknesses that are several orders of magnitude higher.[50] While cells have been aligned on surfaces with patterns of anisotropic features, the majority of these fabricated topographies have a repetitive and relatively homogenous size range.[51–53] These narrow ranges and low variability do not emulate the multi-scale topography of the ECM. Thus, the Khine lab has fabricated a biomimetic substrate with anisotropic multi-scale wrinkle features that attempts to mimic the vast topography of the ECM. This chapter explores the impact of these biomimetic substrates on hPSC-CM response to cardioactive compounds.

3.2 Biomimetic wrinkled substrates

The Khine lab has previously developed a method to create biomimetic substrates with anisotropic multi-scale wrinkle features in a fast and robust manner.[54] To fabricate these substrates, films of pre-stressed polyethylene (PE) were oxidized with a plasma machine to create a stiff surface layer. When the film was shrunk (90% in length) through the application of heat, the stiffness mismatch between the surface and the bulk of the material caused the film to buckle and create multi-scale wrinkles. To generate anisotropic wrinkles, two parallel ends of the film were constrained during the heating process as seen in **Figure 3.1A**. Upon shrinking, a hierarchy of features is formed with major depths and wavelengths along with minor depths and wavelengths, demonstrating the multi-scale nature of the topography (**Figure 3.1B**).[54] The scale of these depths and wavelengths can be tuned with relative ease by controlling the exposure time in the plasma machine. Shrunk PE substrates that are plasma treated for 5 minutes have wrinkle ranges of 60 nm to 3 μm, similar to that of natural ECM fibrils. In addition, a 1:200 dilution of Matrigel was coated onto the substrates. Atomic force microscopy measurements indicated that

the protein coating necessary for cell adhesion did not obscure the features of the wrinkles (**Figure 3.1C**) Human embryonic stem cells, aortic smooth muscle cells, and mouse embryonic fibroblasts have all been aligned on these substrates.[54]

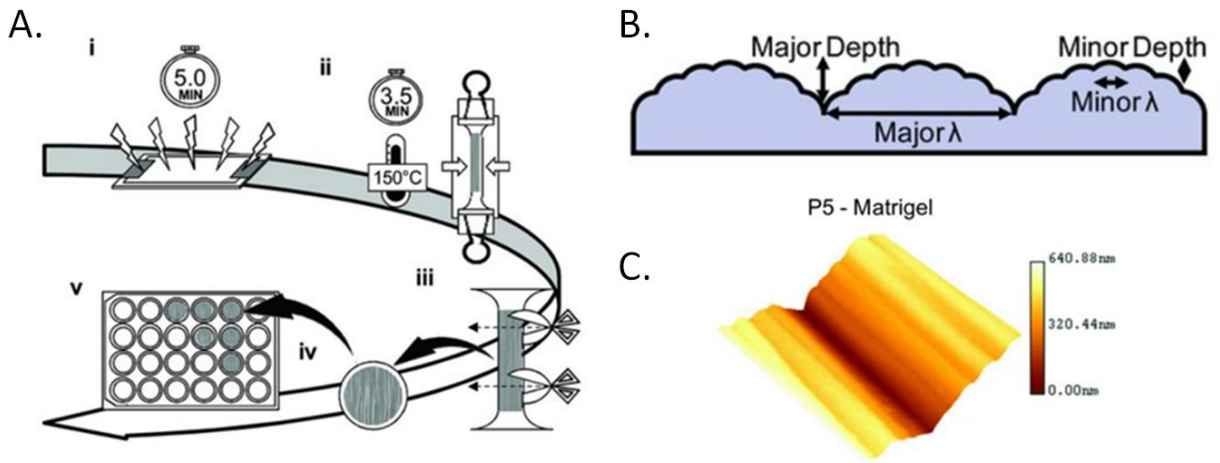

Figure 3.1 Fabrication of multi-scale anisotropic wrinkled substrates A) i) Pre-stressed polyethylene film is treated O_2 plasma to create a stiff oxidized surface ii) The film is then constrained on opposite sides and shrunk. Due to stiffness mismatch between surface and the rest of the film, anisotropic wrinkles are formed with micro- and nano-scale topography. iii) The wrinkled film can then be cut into a desired shape. iv) The film is then mounted onto a glass cover slip and v) can be inserted into standard cell culture plates. B) Schematic of hierarchical features. Micro- and nano-scale features are present and dependent on time of plasma treatment. C) Atomic force microscopy image of substrate that was plasma treated for 5 minutes. The image demonstrates the multiscale topography of the biomimetic wrinkles was retained upon Matrigel coating. The scan distance was 5 x 5 μm^2. Adapted from Chen, A. et al. Shrink-film configurable multiscale wrinkles for functional alignment of human embryonic stem cells and their cardiac derivatives. *Adv. Mater.* **23**, 5785–91 (2011) with permission from John Wiley and Sons.

3.3 Alignment of hPSC-CMs on wrinkled substrates

To evaluate the effect of the substrate's multi-scale topography, human embryonic stem cell-derived cardiomyocytes (hESC-CMs) with both αMHC-mCherry-Rex-Blar and αMHC-Puror -Rex-Neor constructs (courtesy of the Mercola lab) were seeded onto three types of substrates: 1) flat, 2) 8 µM lined (mask created via photolithography), and 3) wrinkled substrates (formed by method described in Section 3.2).[35,55] The 8 µM lined substrates (8 µM width with 8 µM gap in between) represented substrates with topographies that had a repetitive and relatively

homogenous size range. hESC-CMs were differentiated with a protocol developed by Laflamme et al.[56] Unlike the study in Section 3.2, where cells were directly seeded onto the PE film, poly-dimethylsiloxane (PDMS) stamps were first molded to capture the inverse features of the original PE film. Subsequently the original features were then transferred into poly-styrene (PS) substrates via hot-embossing with PDMS stamps. PS was the material of choice as standard cell culture apparatuses (e.g. tissue culture-treated well plates) use it for its bio-compatibility and optical clarity. To enhance protein adhesion and sterilize the surface, the substrates underwent UVO treatment for 8 minutes, prior to fibronectin coating. Finally cells were seeded onto the various substrates at a density of $5x10^5$ cells/mL.

To quantify alignment, cells were stained for α-actinin, f-actin, and nuclei 24 hours after initial seeding as seen in **Figure 3.2A**. For analysis of f-actin stains, alignment was specifically defined as the percent of f-actin aligned to within ±15° to the direction parallel to the line or wrinkled patterns. To calculate this, images of labeled actin were filtered to estimate the image gradient at each pixel location using a Gaussian derivative (sigma=2pixels). The distribution of orientations was estimated by computing a histogram of gradient orientations where the contribution of each pixel was weighted by the gradient magnitude. These weights limited the contribution of pixels in low contrast regions of the image where the gradient orientation estimate was uncertain. The orientation histogram was computed for n=12 disjoint 300x300 pixel subwindows in each image. The standard deviation is computed across the subwindows. For the hESC-CMs, 20 ± 2, 35 ± 0.5, and 42 ± 1% of the cells aligned on flat, line, and wrinkled substrates, respectively (**Figure 3.2B, left panel**). The alignment efficiency of hESC-CMs grown on the wrinkles was about 20% higher than those grown on the line.

The analysis of α-actinin stained images corresponded to the alignment and organization of sarcomeres. An algorithm developed by Bray et al. was used for ridge detection to determine the sarcomere structures in images.[57] Based on the pseudo vectors produced by the algorithm, the orientational order parameter (OOP) was calculated.[20] An OOP value of 0 represents a complete randomized organization, and a value of 1 represents a perfect organization of structures. For the hESC-CMs, the OOPs were 0.06 $\pm$ 0.01, 0.17 $\pm$ 0.02, and 0.25 $\pm$ 0.02 for cells aligned on flat, line, and wrinkled substrates, respectively (**Figure 3.2B, right panel**). The OOP of the hESC-CMs cultured on the wrinkled substrates is close to the OOP measured in primary rat ventricular cardiomyocytes (~0.45) cultured on anisotropic fibronectin patterns.[58] These results both indicate that wrinkled substrates aligned the cardiomyocytes more efficiently than the control substrates, flat and 8 μM lined.

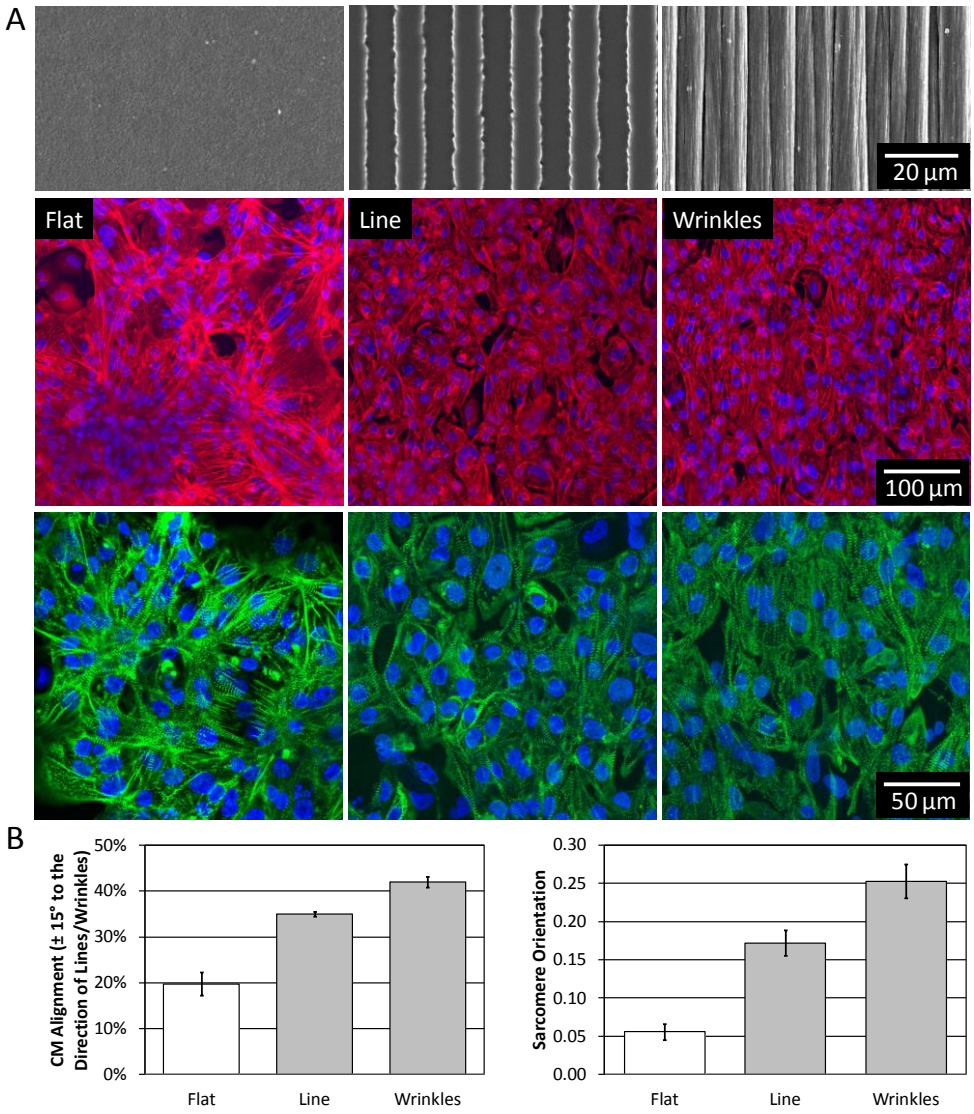

Figure 3.2 Alignment of hESC-CMs on various substrates A) (top panel) Scanning electron microscope images of flat, line, and wrinkled substrates at 1000× magnification. (middle panel) Fluorescent images of f-actin of hESC-CMs aligned on various topographies. The images were taken at 20× magnification. (lower panel) Fluorescent images of α-actinin of hESC-CMs aligned on various topographies. The images were taken at 40× magnification. B) (left panel) Quantification of the f-actin alignment efficiency. Bar graph showed the percent f-actin alignment. (right panel) Quantification of the sarcomere alignment efficiency using orientation organization parameter.

3.4 Drug response of hPSC-CMs cultured on biomimetic wrinkles

While the wrinkled substrates demonstrated the best alignment of cardiomyocytes among the three substrates, the effects on hESC-CM response to cardioactive compounds were evaluated by screening E-4031, a hERG K^+ channel blocker, and isoproterenol, a β-adrenergic agonist. For all screens, drug compounds were added in a serial manner to achieve cumulative concentrations. E-4031 was tested at 0, 1, 3, 10, and 30 nM, while isoproterenol was tested at 0, 0.1, 1, 10, and 100 nM. All cardoactive effects and changes in hESC-CM behavior were captured with brightfield microscopy and analyzed with the optical flow technique and post optical flow contraction (pOFC) analysis described in Section 2.3.1 and 2.3.2. Again, the pOFC was able to compute key contractile parameters: 1) duration of contractile duration, 2) beating frequency, 3) synchronicity of monolayer, 4) orientation (the sum of magnitude for all y-axis components and the sum of magnitude of all x-axis components), and 5) acceleration. Cardiac cells from all surfaces exhibited increased contractile duration when treated with 10 nm E-4031; however, only those grown on the wrinkles responded to 3 nm of E-4031 as indicated by reduction in the contractile orientation. The concentrations of 3 and 10 nm of E-4031 are comparable to the published IC_{50} in hERG channel assay (7 nm).[59,60]

Isoproterenol is a known chronotropic, dromotropic, and inotropic agent to cardiac cells. This drug was originally developed for treating asthma; however, arrhythmia is a known serious adverse effect.[61] Three trials of isoproterenol were conducted in which each three cardiac cell ages were evaluated. Cells were around differentiation days 20, 40, and 60 for trials 1, 2, and 3, respectively. After administration of the drug compound, all cells exhibited increase in contractile frequency and acceleration on all surfaces regardless of cell ages (**Figure 3.3, Table**). The drug also affected the contractile duration (all three trials), synchronicity (all three trials),

and orientation (trial 2 and 3 only) of cells grown on the wrinkles; these differences were not evident in the flat and line substrates. While hESC-CMs demonstrated immature properties, providing these cells with topographical cues that are similar to those in the native heart might force the cells to behave as a more mature tissue. Therefore, a more evident contractile response to the drug treatment for those grown on the wrinkles can be quantified compared to the other two surfaces.

The topographical effects on CMs could also be inferred from these sets of experiments. Most of the contractile parameters were similar between cells grown on the flat and wrinkles at differentiation day 40 and 60. However, at differentiation day 20, the cells grown on the wrinkles were more responsive to the drug than those grown on both flat and line surfaces (**Figure 3.3**, bar graphs). Since isoproterenol is known for affecting calcium ion channels, these results could imply that the expression and development of ion channels of cells grown on the wrinkles might be more effective than those grown on the other surfaces in the earlier post differentiation period.

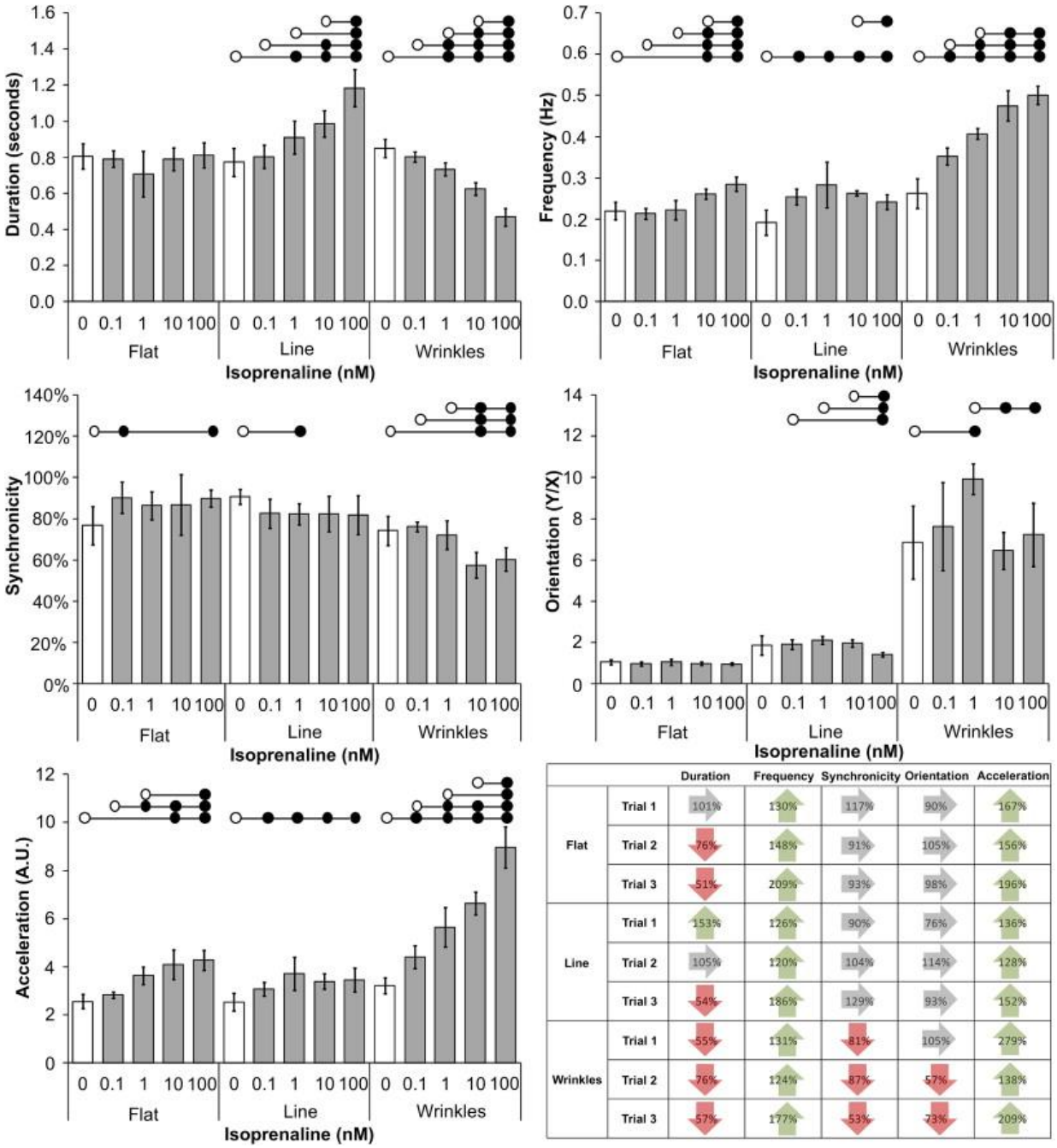

Figure 3.3 Effects of isoproterenol (also known as isoprenaline and referred to as such in this figure) on cardiac cells growing on various topographies. Bar graphs summarized results from trial that evaluated the drug effects on cells at differentiation day 20. The table summarized the changes in contractile parameters between 0 and 100 nM isoprenaline in all trials. The values are the percent changes compared to the 0 nM condition. Green up arrow indicated an increase, gray horizontal arrow indicated no change, and red down arrow indicated a decrease in the values associated with the corresponding parameters.

3.5 Summary

Biomimetic substrates with anisotropic and multi-scale wrinkles can be fabricated from pre-stressed plastics with relative ease. These substrates induced better alignment in cardiomyocytes than the control substrates, flat and homogenously lined surfaces. The sensitive responses of cells seeded on the wrinkled surfaces in both the E-4031 and isoproterenol screening suggest that the alignment of cardiomyocytes alone is not enough; instead, the multi-scale topography ranging from the micro- to nano-scale is crucial and may induce more mature ion channel development in cardiomyocytes. The use of these biomimetic substrates may be beneficial in the screening for cardiotoxicity as the cardiomyocytes may respond more similar to those found in the native myocardium. Unlike other techniques that aim to mature hPSC-CMs for more physiologically relevant phenotypes, the use of these substrates is chemical-free and is relatively inexpensive. The wrinkled features are not limited to PS and can be transferred into any material that can be hot-embossed or molded. These biomimetic substrates can be easily integrated with other methods to further address the fetal-like qualities of hPSC-CMs for drug screening purposes.

CHAPTER 4: Adaptation of wrinkled substrate for high-throughput screens

4.1 Introduction

A key criterion in whether a detection platform is implemented for the screening of cardiotoxicity is its suitability for medium to high-throughput use. Typically, target based or biochemical assays can achieve screens of 10,000 compounds per assay per day through automation and small volume formats. While using mammalian cell-based assays has more limitations, cardiotoxicity screening platforms that are commercially available and use hPSC-CMs are already incorporating 96 to 1536 wells plate formats.[62] In terms of the biomimetic substrates, the study in Chapter 3 Section 3.4 used the substrates and cells in a manner that was inefficient for throughput. To form one confluent monolayer on the substrate (cut in the shape of a 15 mm circular glass coverslip), a density of $5x10^5$/mL was needed. However, within the field of view for the microscope (10x objective on Nikon TE 300), less than 1% of the surface area (~0.59 mm^2 of 353.25 mm^2) was being recorded at a given time. Taking acquisitions of multiple locations across the substrate cannot be considered as multiple independent samples. Because the cardiomyocytes were in a confluent monolayer, they beat synchronously, were electrically linked, and must be treated as one sample.

While it is possible that the biomimetic substrates can be configured for the bottom of 96 well or 384 well plate, concerns over the effects of evaporation and gas-exchange on cell behavior arise when lower-assay volumes are involved. [63] Thus, for the platform developed by the Khine lab, an alternative approach was taken to adapt the biomimetic substrates for high-throughput use. To increase throughput, islands of cardiomyocytes with micron-range dimensions are selectively patterned onto a single surface, allowing for multiple independent

samples to be present within a substrate. In addition, without the need for a physical barrier (e.g. wall of a well), the islands can be placed within close proximity such that multiple samples can be captured within one video acquisition. Such acquisition would increase throughput by reducing overall processing time required by the optical flow. This chapter details the chemical approach that is taken to achieve this patterning and the corresponding characterization of formed islands.

4.2 Micropatterning islands of cardiomyocytes

4.2.1 Surface Modification

A popular approach to selectively pattern proteins onto surfaces is microcontact printing. The basis of this approach is to load an 'ink' (solution containing desired proteins to be transferred) onto the surface of an elastomeric stamp and then, apply the stamp face down onto final substrate with a select amount of force. If the substrate has a surface that is more energetically favorable than the surface of the stamp, the proteins will transfer in the areas where the stamp and substrate make contact.[64,65] The surface energy of either the stamp or substrate can be modified to alter protein adsorption or transfer efficiency with techniques, such as plasma- or UV-treatment and fluorine based silanization.[64,66]

Microcontact printing was initially attempted to selectively pattern proteins on the wrinkled substrates. However, mixed results were achieved as the quality of the transfers was highly variable. One of the major issues was that wrinkled substrates have a heterogeneous surface with varying depths. Typically microcontact printing is performed on flat and homogenous surfaces, which allow the micro-features of the stamp to form a reversible seal. With the heterogeneous surfaces of the wrinkled substrates, the total surface area of contact

between the stamp and substrate was decreased, forming a weaker seal and allowing the stamp to slide. As a result, the resolution of the transfers was poor and in certain cases, the proteins would appear smeared. In addition, another factor in the variability of protein transfer was the amount of force applied to the stamp. While identical weights were used in each print, alignment of the center of the weights to that of the stamp was difficult. Thus, a disproportionate amount of force was applied to different areas of the stamp. This issue can be resolved, but would require the need for custom apparatuses. Therefore another method was south with the ability to pattern heterogeneous surfaces, reproducibility, and even distribution of protein among selected areas.

Ribeiro et al. demonstrated that using a process with 3-glycidoxypropyltrimethoxysilane (GPTMS), an organosilane, proteins necessary for cell adhesion can be covalently bonded onto surfaces, even those with high surface hydrophobicity (e.g. polydimethylsiloxane).[67] Surfaces are activated by the bombardment of O_2 plasma, which introduces polar functional groups that allows for linkage to the trimethoxysilane group of GPTMS.[68] An advantage of the plasma treatment is that the activation across the surface is relatively uniform. In their study, Ribeiro et al. were able to culture neonatal mouse cardiomyocytes on laminin coated polydimethylsiloxane (PDMS) posts.[67]

We leveraged this GPTMS process and combined it with stencil lithography to create a method that is capable of patterning on heterogeneous surfaces with relative uniformity. As seen in **Figure 4.1A**, we first created a shadow mask using a CO_2 laser cutter (VLS2.30). The mask was a polymer film (Grafix Arts, Frisket Film) with a removable single-sided adhesive that was left minimal residue. After laser cutting, the mask was applied to the surface of the substrate. For the demonstration of this select patterning using the GPTMS approach, we used PDMS substrates that were molded with the wrinkled features. The GPTMS process is not limited to

only PDMS, but it can be applied to glass, thermoplastics or anything that can be activated by O_2 plasma treatment. An advantage of using PDMS or a silicone based polymer is that the stiffness can be tuned by blending polymers or altering the ratio of base to curing agent. To ensure that the wrinkled features of the PDMS substrates were the same as the PS ones, the original PDMS stamps meant for hot-embossing were used. Typically molding PDMS from a PDMS template is challenging as the new silicone mixture may chemically bond with the template. To prevent this, the template was coated with 5% pluronic acid, a surfactant, prior to the molding step. The fidelity of the wrinkles were found to be similar to those of the PS substrates with no statistical difference among the roughness parameters calculate by a 3D laser scanning microscope (Keyence VK-X110). The mask and substrate were then O_2 plasma treated (Plasma Etch PE-50) for 3 minutes. Afterwards, the mask was removed and the substrate was then incubated in a methanol solution of 20% GPTMS. Following methanol and deionized water washes, the substrate was dried with an air gun. To ensure dryness and sterilization, the substrates were autoclaved. Next, to prevent non-selective protein adsorption, non-functionalized areas were blocked with 5% pluronic acid for an hour (Pluronic F-127). Finally after phosphate buffer saline washes, the substrate was prepared for select protein coating.

Aside from uniform protein deposition onto heterogeneous surfaces, this organosilane and stencil lithography approach provides other advantages that make it suitable for high through-put use. GPTMS, like many organosilanes, is stable at room temperature and in ambient environment unlike plasma treatment, which only has temporary effects. This stability gives it a shelf-life suitable for manufacturing and potential commercial needs. As seen in one of the steps, the GPTMS is thermally stable at the temperature range for autoclaving, allowing for convenient

sterilization. Finally as the process laser cuts the shadow masks, the dimensions of the micro-islands can be changed with ease and without the need for a clean room.

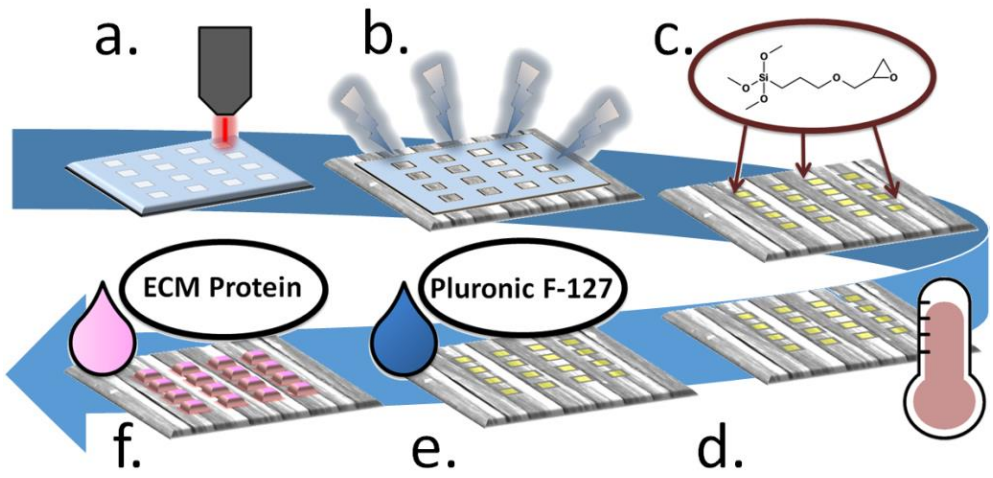

Figure 4.1 Organosilane approach to selectively pattern cardiomyocytes A) A shadow mask is created by laser cutting a film with reversible and single-sided adhesive. B) After mask is applied to wrinkled surfaces, select areas are activated via O_2 plasma treatment. C) Substrate is then incubated in an organosilane solution, 20% GPTMS in methanol. 4) Afterwards, substrate is autoclaved for sterilization. 5) A surfactant, Plurnoic F-127, is used to block for potential non-selective protein adsorption. 6) Substrate is then coated with proteins for cell adhesion.

4.2.2 Characterization of Patterns

Prior to coating ECM proteins and seeding cardiomyocytes on the wrinkled substrates, we conducted a feasibility test with tetramethylrhodamine isothiocyanate (TRITC)-conjugated streptavidin ($\lambda_{excitation}$ = 550 nm, $\lambda_{emission}$ = 570 nm) as a model protein to demonstrate covalent attachment. As seen in **Figure 4.2A** (left panel), we first designed a mask with a square array of 81 total islands. Each island was a square with 500 µM sides and was 500 µM apart from all neighboring islands. Following the GPTS treatment as described in the previous section with the square array mask, a flat PDMS substrate was incubated with 10 µg/mL of streptavidin-TRITC for an hour at room temperature. When we imaged the substrates with an upright epifluorescence microscope (Olympus BX-53), we were able to affirm that arrays of proteins patterned as

squares were present. In **Figure 4.2A** (right panel), we do see that the edges of the squares were cragged and this could be attributed to the quality of laser cutting the frisket film. If perfectly smoothed lines are desired, a precise shadow mask can be machined from rigid materials such as metal; however the trade-off is that machining would be more expensive with a greater turnaround time for mask adjustments. Once it was established that proteins patterns could be deposited on flat surfaces, we repeated the process on the heterogeneous wrinkled substrates. From the images as seen in **Figure 4.2B**, we again patterned down proteins in a square array format. In **Figure 4.2C**, we see that the anisotropic features were preserved as they were identifiable.

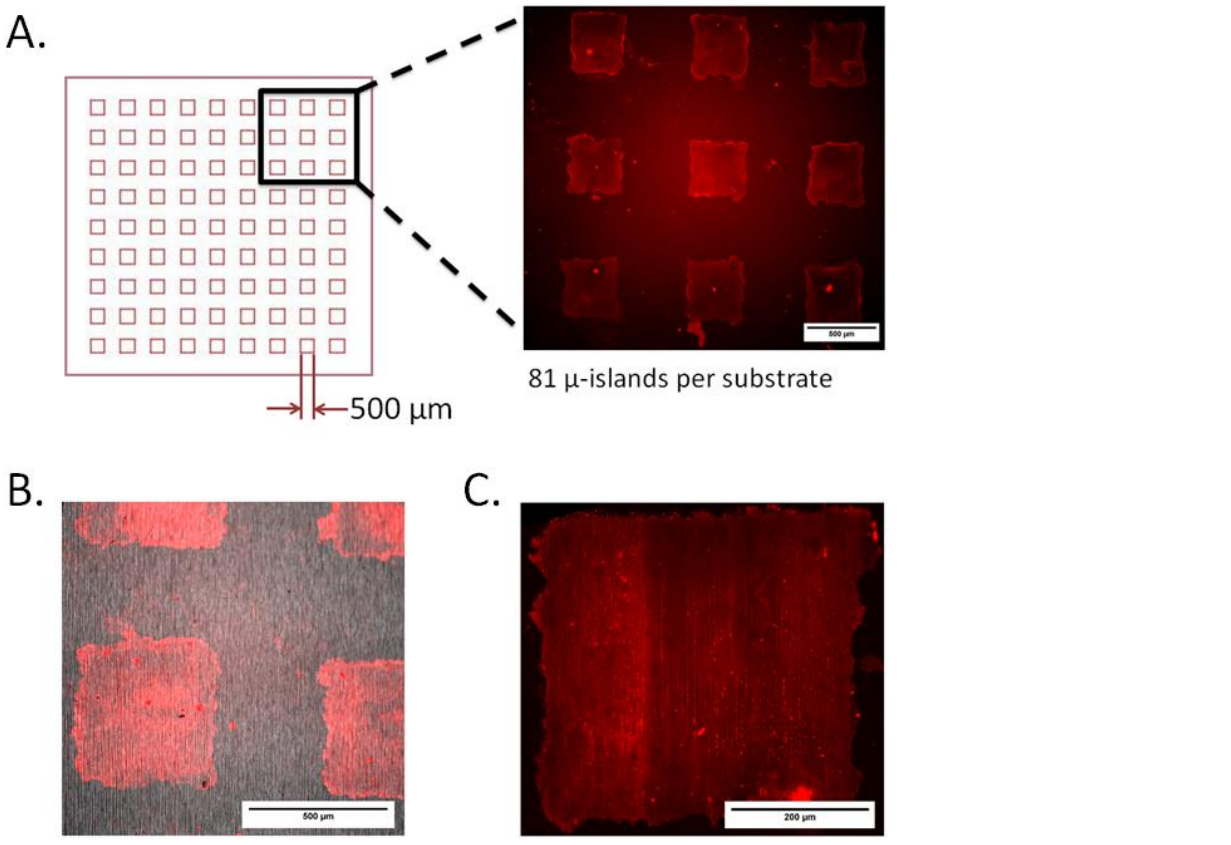

Figure 4.2 Characterization of organosilane approach with streptavidin-TRITC. A) Shadow mask was designed with 81 islands with features of 500 µm x 500 µm with a 500 µm gap in between islands. Streptavidin-TRITC was used as a model protein to show deterministic patterning on flat PDMS surfaces. B) Organosilane treatment was then applied to heterogeneous surfaces, anisotropic wrinkled substrate. Fluorescent image of square array overlaid on original brightfield image. Image was taken with a 4X

objective. C) Fluorescent image (taken with a 10X objective) of an individual island showed that wrinkled features were still preserved after protein coating.

4.2.3 Cell seeding and island independency

After the proof-of-concept on both homogeneous and heterogeneous surfaces, we plated stem cell-derived cardiomyocytes (stem cell line: hES2-7E) onto a PDMS substrate that had both flat and wrinkled surfaces. This PDMS substrate was designed to fit into a well of a 4 chamber slide (surface area of 1.7 mm^2 per well). Substrates were seeded at a density of $4.2x10^5$ cell/mL. The substrates prior to seeding were coated with Matrigel diluted at a 1:200 ratio. As seen in **Figure 4.3A**, the cardiomyocytes plated as islands and retained their square shape. To ensure that the anisotropic wrinkles did have an effect on cardiomyocytes and their contractility, we captured brightfield videos of the human embryonic stem cell-derived cardiomyocytes (hESC-CMs) contracting and measured the directionality of the vectors generated from the optical flow analysis as described in Chapter 2. In **Figure 4.3C**, the islands plated on the flat surface had a random orientation in the directionality of vectors, indicating no preference. However, the micro-islands formed on the wrinkled surfaces had a much stronger preference for the x-axis, which is parallel to the anisotropic wrinkles. To quantify this, we again used the orientation parameter X/Y ratio, which is the ratio between the sum of x-axis components' magnitudes and the sum of all y-axis components' magnitude. A ratio of 1 would indicate that the directionality of the contraction was random and had no preference. A ratio larger than1 would suggest the islands have a preference in contracting along the x-axis. Based on this, the islands cultured on the wrinkled surface (n = 6) had a larger X/Y ratio (1.36 $\pm$ 0.11) than the ratio (1.10 $\pm$ 0.16) of those cultured on the flat surfaces (n = 4), indicating a stronger preference to contract within the direction of the x-axis.

Another critical component of using the biomimetic substrates for high-throughput is that the formed islands of cardiomyocytes are truly independent samples. If the islands were independent from its neighbors, the contractile behaviors would be all different along with an asynchronous beating. As seen in **Figure 4.3B**, when we examined a video of 4 neighboring islands (taken with a 4X objective on the Olympus IX83 microscope), the PCA contractile plots indicated very distinct contractile patterns. For example, the island in the top left of the image beat at a frequency that is approximately 3-fold lower than that of the island in the top right. In addition, based on the amplitude of the contractile plots, the contractility of the top left island was over two-fold less than that of the island in the top right. These results preliminarily show that we can leverage an organosilane treatment and stencil lithography to selectively pattern cardiomyocytes and increase the number of independent samples within a single substrate.

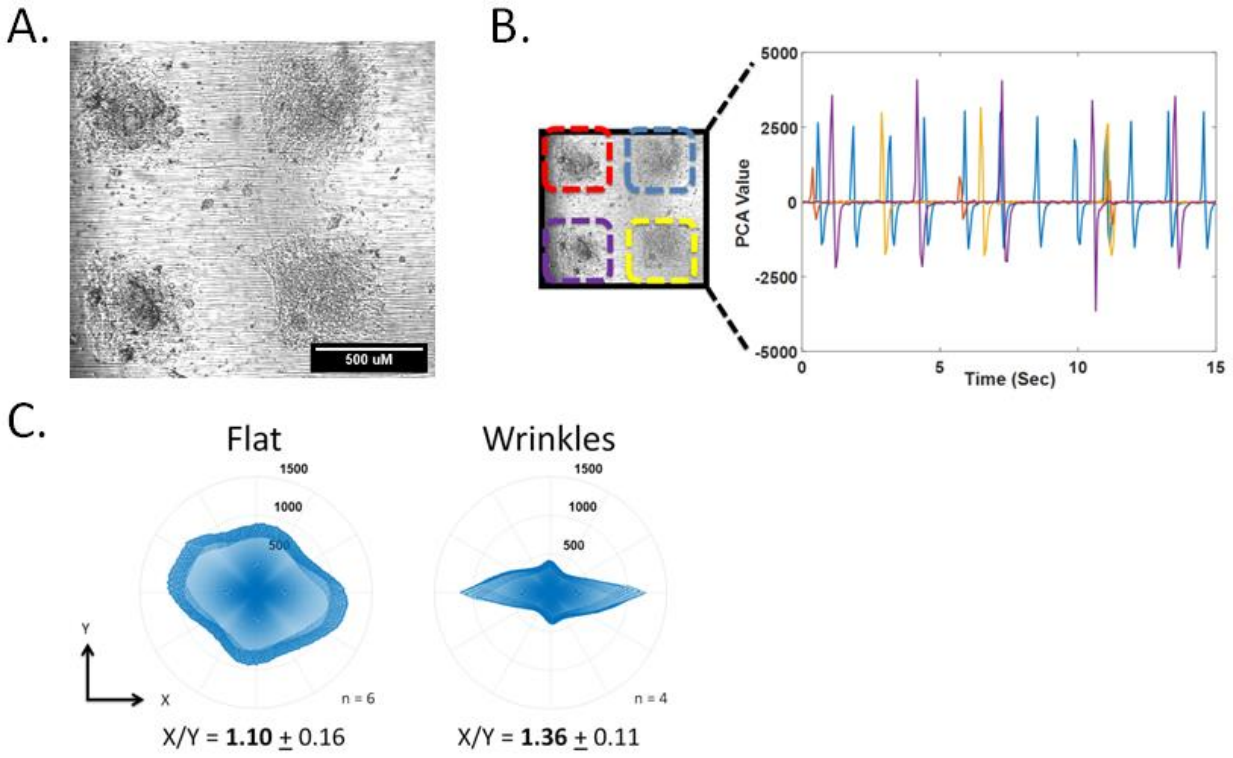

Figure 4.3 Evaluation of patterned islands' contractility. A) hESC-CMs were selectively patterned onto the anisotropic wrinkled PDMS substrate in a square array manner. B) PCA analysis indicated that each island has a unique contractile pattern that is independent of its neighbors. C) Islands of hESC-CMs

formed on the wrinkled substrates (n = 4) were compared to those formed on flat surfaces by examining the X/Y parameter. The X/Y parameter is the ratio between the sum of x-axis components' magnitude and the sum of all y-axis components' magnitude. A ratio of 1 would indicate that the directionality of the contraction was random and had no preference. A ratio larger than1 would suggest the islands have a preference in contracting along the x-axis.

4.3 Summary

In this chapter, we present a method to adapt the biomimetic wrinkled substrates for high-throughput use. The capability to do so is essential in the commercial viability of these substrates as various commercial platforms have already demonstrated their capacity for throughput. The goal of our method was to pattern multiple islands of cardiomyocytes onto a single wrinkled substrate. Instead of physically transferring the proteins onto the surface (e.g. microcontact printing), we used an approach that combines organosilane treatment and stencil lithography. This combined method provides the advantage of reproducibly patterning onto heterogeneous surfaces with relative uniform deposition. In addition, by using a laser cutter, shadow marks can be altered and fabricated in short periods of time. We demonstrated that hESC-CMs can be controllably seeded in a square array format with this approach. Each of the islands had independent contractile behavior and the ability of the anisotropic features to align cells was preserved as the hESC-CMs seeded on the wrinkled substrates had a preference to contract in the direction parallel to the features. Besides increasing the number of independent samples, videos of the contracting islands were taken at a lower magnification such that four islands appeared within one view. By doing so, throughput is increased by reducing the computational resources and time to analyze the contractility of each island of cardiomyocytes. While we showed that the biomimetic substrates can be feasibly adapted for high-through put use, the method still needs to be optimized and further characterized for commercial use. In particular, the optimal ratio of seeding density to the surface area of each island needs to be determined for consistent formation

of monolayers. A potential concern with having multiple islands of cardiomyocytes on a single substrate is paracrine signaling (e.g. release of growth factors) between the islands in response to exposure of a drug compound. Such an issue can be mitigated by measuring cardiomyocyte response in a timely manner. For example, functional measurements of cardiomyocyte response during the drug screens described in Chapter 5 Section 5 were captured in 5 minute intervals. Paracrine communication can be estimated to take place on a time scale of 10-30 minutes. If longitudinal studies are desired, the formation of factor gradients can be minimized by placing the islands in a microfluidic platform with designed flow. We have demonstrated that these islands can be patterned and then encased in a fluidic platform.[69] Finally, some other aspects of the organosilane and stencil lithography method that need to be explored include choice of protein for cell adhesion, substrate stiffness, and geometry of cardiomyocyte islands.

CHAPTER 5: Application of supervised machine learning

5.1 Introduction

Various screening platforms have emerged in recent years to address the need for more accurate and faster pre-clinical detection methods of drug-induced cardiotoxicity. A majority of these platforms have begun to utilize human pluripotent stem cell-derived cardiomyocytes (hPSC-CMs). Aside from the commonality of using hPSC-CMs, these screening platforms greatly vary in their setup. These systems can drastically differ in their methodology of quantifying changes in hPSC-CMs exposed to cardioactive compounds. Some systems examine the electrophysiological properties while others observe the calcium transients or directly measure the force being generated by hPSC-CMs.[16,30,46,70–74] The nature of this outputted data becomes high-dimensional especially when multiple experimental conditions are present or a multiplex system is used.[29,75] Traditional approaches of examining a few pre-determined parameters independently of one another may not adequately summarize and reflect cardioactive effects of a compound administered to hPSC-CMs. There is a possibility that the information that separates the behavior of normal hPSC-CMs from those exposed to the cardioactive compound is only present in disregarded parameters or a combinatorial form of examined parameters. Furthermore, as these platforms are designed for high-throughput screens, the analysis needs to be automated yet still provide comprehensive results.

Rather, holistic approaches must be developed to optimize the utility of datasets generated from screening platforms. Machine learning offers a possible solution as it can evaluate multiple parameters simultaneously without *a priori* knowledge; therefore, it can discover unexpected relationships to potentially yield better detection. In this chapter, we demonstrate the application of machine learning to the data generated from two platforms that

vary in their methodology of quantifying changes in hPSC-CMs. Collectively, we show that machine learning can determine whether a compound is cardioactive, predict the compound's mechanistic action based on a drug classification model, and provide drug response relationships between compounds. Such information would assist in streamlining the drug discovery pipeline, allowing for the rapid identification of select compounds for more in-depth follow up assays. In addition, this information coupled with knowledge of predicted class can guide scientists to efficiently and selectively screen for specific drug-to-drug interactions that prompt cardiotoxicity (e.g. disruption of Ca^{2+} handling when sofosbuvir and amiodarone are combined) instead of a brute force approach.[76] Finally, machine learning is able to provide all of this information in an automated manner, which would be ideal for any high-throughput system.

5.2 Binary SVM Background

Support vector machine (SVM) is a form of supervised machine learning that can be used for classification purposes. SVM classifies data points into two groups by creating a decision boundary that separates the groups. In the example of **Figure 5.1**, where the goal is to separate the red x's from the green circles, multiple lines can be drawn to complete this task. SVM is able to address this issue by choosing the line that maximizes the separation or margin between the two classes. This task is accomplished by finding the greatest distance between the nearest points in each class. These nearest points are referred to as the support vectors. The determination of the optimal separation line or hyperplane is solely dependent on the support vectors, a subset of all present data.[77,78]

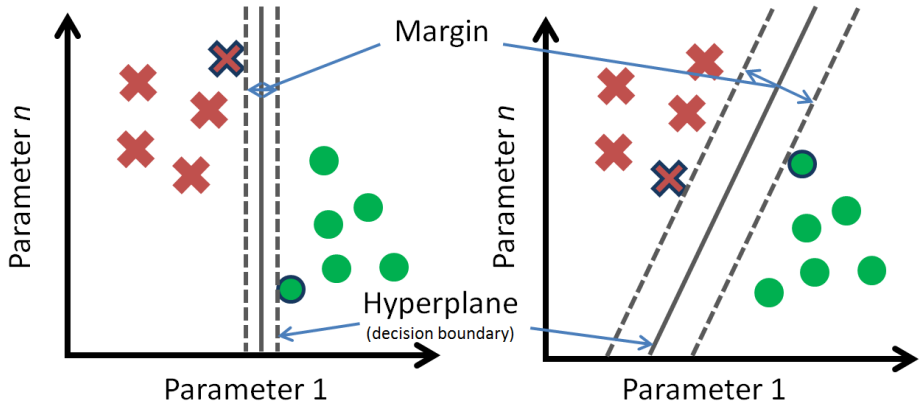

Figure 5.1 Classification with support vector machines. If the given task is to classify or separate the red X's from the green circles, this can be achieved with a line as seen in left panel. However, this line is one of multiple lines can be drawn. SVM determines the optimal by maximizing the margin between the support vectors. That line is referred to as the hyperplane or decision boundary. The support vectors represent the data points that are located on the margin. In the right panel, the line separating the two groups appears to achieve the largest margin possible, making it the hyperplane. If a new unknown data point were to be classified and was on the right of the hyperplane, it would be labeled a green circle (it would be labeled a red X if the point was to the left of the hyperplane).

In the example above, the classes could be separated with a linear hyperplane. However, this is not the circumstance with a lot of data, especially biological data. In **Figure 5.2**, it is apparent that a linear line cannot separate the green circles from the red x's. The optimal line of separation is rather a polynomial line. SVM or a linear separation line can still be implemented if the data was mapped from the input space into a vector space (possibly higher-dimensions) with a function φ. However if the vector space is high-dimensional, representing the transformed data can be computationally consuming. Thus, the kernel trick is utilized. Instead of mapping all the data points into the higher-dimensional vector space, a similarity measure is calculated in the higher-dimensional space. In SVM, this similarity measure is simply the dot product of the transformed vectors in the higher-dimensional space. In the example of two dimensional data ($x,z \in X$) and an existing mapping function to N-dimensional space

(φ: X → $\Re^N$), the inner product would be represented as $\langle\varphi(x), \varphi(z)\rangle$. There exists a kernel functions (K) such that $K(x,z) = \langle\varphi(x), \varphi(z)\rangle$. This kernel function is used in the calculation of the optimal hyperplane and allows for non-linear SVM classification.[79,80]

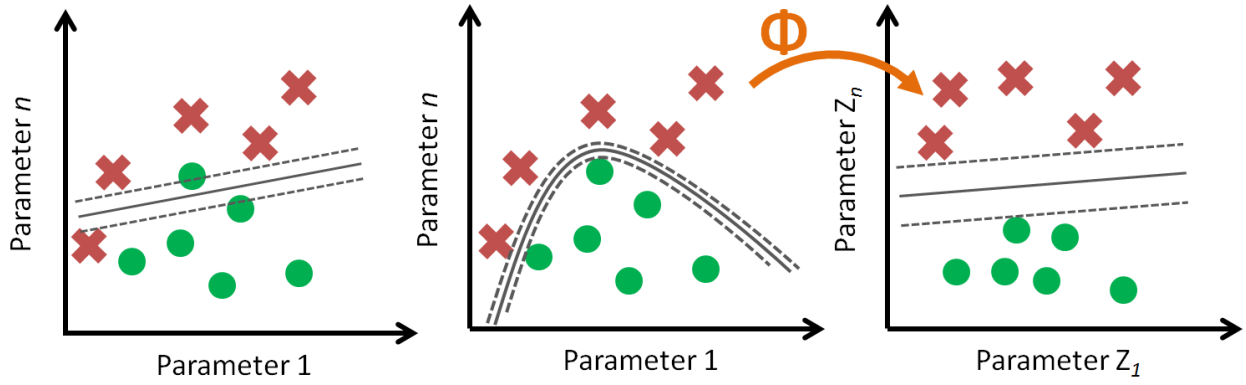

Figure 5.2 Non-linearly separable data and SVM. (Left panel) a linear separation cannot be used to separate the green circles from the red X's, a linear separation line cannot be used. (Middle panel) Instead separation of the two classes can be achieved if a polynomial line or non-linear function was used. (Right Panel) To be able to utilize SVM, the current input space can be transformed with a function φ into a new feature space in which linear separation is viable.

In scenarios where a hyperplane cannot be perfectly drawn while using either linear or non-linear SVM and data points are present within the margins, a soft margin method can be introduced with a non-negative slack variable (ξ) that represents the degree of misclassification. The algorithm will then penalize for the degree of non-zero ξ. In the search for an optimal hyperplane, it will result in a trade-off between a large margin and a small penalty error.[81]

5.3 Detection of drug-induced cardioactivity

5.3.1 Rationale and experimental design

Using binary SVM, we were able to create a singular quantitative index that described a compound's level of cardioactivity through the analysis of brightfield videos. To evaluate the efficacy of our method that pairs brightfield imaging and machine learning, we compared it to a more traditional fluorescent-based intracellular calcium assay. With human induced pluripotent

stem cell-derived cardiomyocytes (iPS-CMs), we screened three cardioactive compounds with distinct, dissimilar effects: E-4031 (hERG K^+ channel inhibitor), verapamil (L-type Ca^{2+} channel blocker), and blebbistatin (myosin-II inhibitor). The concentration range for each drug was selected based on the demonstrated window of cardioactive effects in previous studies.[17] To the best of our knowledge, we reported for the first time the integration of brightfield imaging with machine learning on iPS-CMs to detect drug induced cardioactive effects, and demonstrate superior performance to fluorescence-based methods.

5.3.2 Drug treatment and time-lapse imaging

To screen the three cardioactive compounds, iPS-CMs were seeded into 8-chamber Lab-Tek II chamber slides (Electron Microscopy Sciences) at a density of 150,000 cells/well. All cardiomyocytes were 40+ days post differentiation for the drug screens. Prior to expo- sure to drug compounds, three baseline measurements were made at time points 0, 30, and 60 minutes, which represented a baseline or healthy iPS-CM contractile behavior. Drugs were serially added to the wells, waiting 20 minutes after addition before taking measurement. RPMI/B-27 was used as placebo. At each time point, videos of contracting cardiomyocytes were acquired with an Olympus IX83 (Olympus) inverted scope equipped with an ORCA-R2 color charge-coupled (Hamamatsu) camera and MetaMorph software (Molecular Devices). To control for temperature and pH, an incubation system (model ZILCS) consisting of a stage top incubator, temperature controller, and gas flowmeter (Tokai Hit) was used with 5% CO2. Both fluorescent and brightfield acquisitions were taken for approximately 17.5 seconds at 15.6 fps at a resolution of 672 × 512 or at 8.6 fps at a resolution of 1392 × 1040 (subsequently downsized to a resolution of 672 × 512 via bilinear interpolation) and saved as a TIFF stack. To address variation among cell

populations within the same sample, stage locations were recorded prior to any acquisitions to ensure that the same cells among a sample were imaged.

5.3.3 Fluorescent-based intracellular calcium assay

For the fluorescence-based method, we utilized an iPS cell line transduced with a genetically encoded fluorescent calcium indicator, GCaMP6 (WTC11-AAV-CAG-GCaMP6; provided by Dr. Bruce Conklin of the Gladstone Institute of Cardiovascular Research). This method is similar to those found in industry for the high-throughput screening of drug-induced cardiotoxicity.[82–84] In order to quantify the calcium transients, a 240 by 240 pixels region of interest (ROI) was selected for each video taken with the fluorescent channel (**Figure 5.3C**). The average intensity value within the ROI for each frame was measured and imported into MATLAB (MathWorks). An automated code was written to identify the start and the peak of each contraction. However, the raw GCaMP6 signal acquired over time showed a rapid decay due to photobleaching (**Figure 5.3D**). The photobleaching artifact was eliminated by fitting an *n*-th (n = 2-10) order polynomial curve to the baseline of the signal, defined as the starting point of the calcium transient, and then normalizing the raw signal by the baseline value (**Figure 5.3E**). In addition, the starting points were normalized to zero using linear interpolation. From this data, we calculated the beating rate and the calcium transient duration 90% (CTD_{90}), defined as the duration of the fluorescent signal that was 90% below the peak amplitude of the transient (**Figure 5.3F**).

In addition to the rapid photobleaching over a single acquisition time frame, we noted that the GCaMP6 signal also experienced a smaller photobleaching effect over multiple acquisitions. This loss of signal intensity caused artificial decreases in CTD_{90}; this was corrected

by normalizing CTD_{90} with the amplitude of the calcium transient signal (**Figure 5.3G**). This corrected value is referred to as the Shape Ratio 90 (SR_{90}), and serves as one of the two parameters analyzed for the GCaMP6 method with the other parameter being beating frequency. This effect was independent of time between acquisitions. A compound was deemed to be cardioactive if any of the concentrations were different from the control with statistical significance in either of the two parameters. Statistical significance was measured with one-way repeated measure ANOVA. If a significant p-value (p-value < 0.05) was obtained from the repeated-measures ANOVA, we proceeded with Dunnett's test to determine which concentration differed from our baseline measurements. Differences with p-values less than 0.05 were considered statistically significant. All reported values in Section 5.3 are in the format of mean + S.E.M. All reported sample sizes (*n*) refer to independent wells of chamber slides (biological replicates).

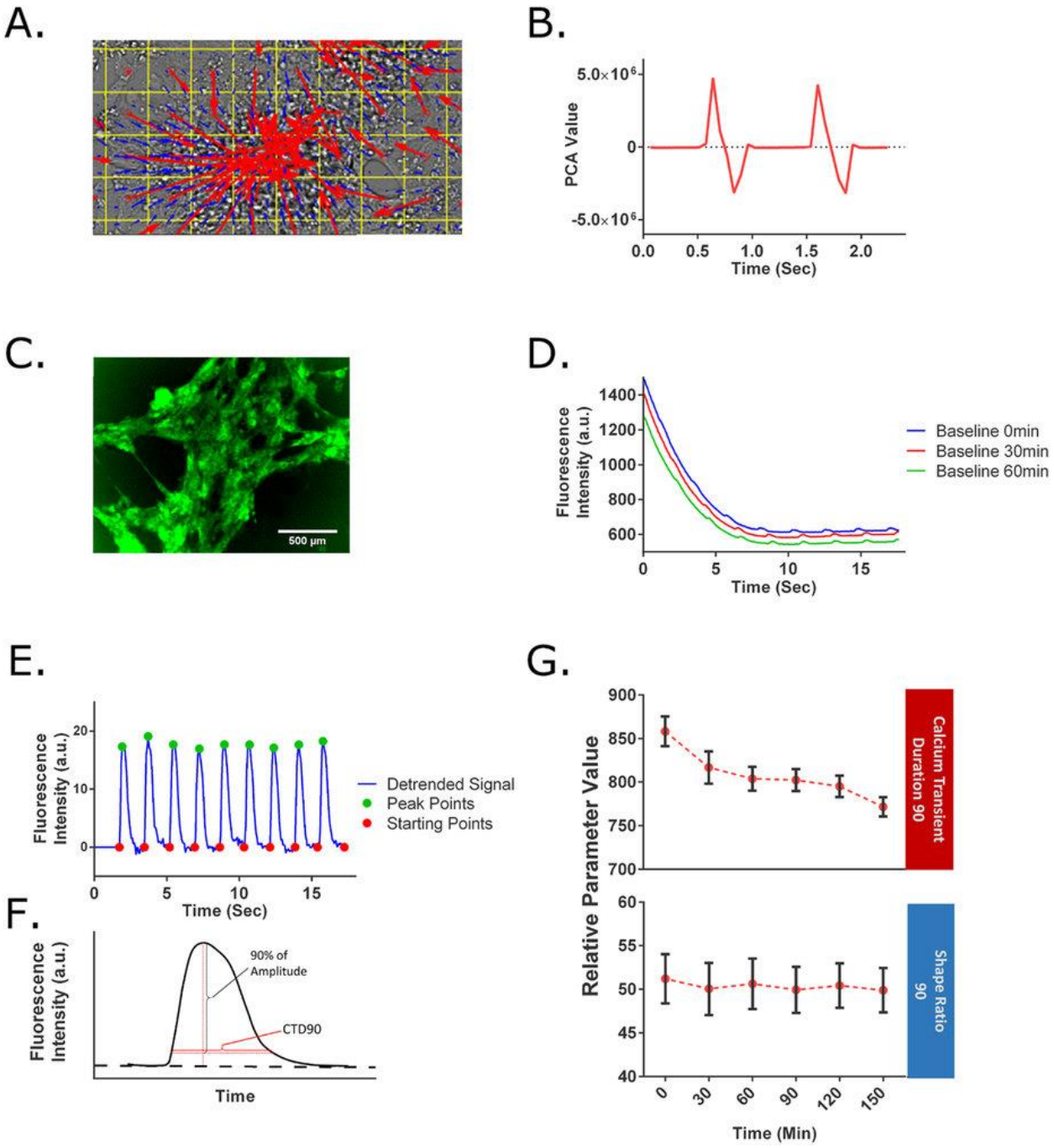

Figure 5.3 Data acquisition and analysis for GCaMP6 and brightfield signal. A) For the brightfield method, images were processed by an optical flow algorithm to generate vectors that represent the motion of the iPS-CMs. The blue vector arrows represented the average motion of 20 × 20 pixel regions, while the red vector arrows represented 50 × 50 pixel regions. The convergence of the vector arrows toward a center visually represented an iPS-CM cluster in the contraction phase. B) Based on the vectors, a contractile profile was derived from the 1st PCA of the norm of the x- and y-vectors. Positive PCA values indicate contraction phase, while negative values signify the relaxation phase. C) GFP signal produced by the contraction of cardiomyocytes derived from GCaMP6 iPS cells. D)

GCaMP6 signal recorded over time for 3 sequential acquisitions at baseline. The signals showed a rapid photobleaching effect within the first 5 seconds, but also showed a photobleaching effect between the different acquisitions. E) The starting points and peaks of the calcium transients were identified using the detrended GCaMP6 signal. F) A graphical explanation of CTD_{90}. The SR_{90} is defined as the ratio of CTD_{90} to the amplitude of a given calcium transient. G) A longitudinal experiment showed an artificial decrease in CTD_{90} due to photobleaching. This was corrected by normalizing by the amplitude in SR_{90}.

5.3.4 Quantification of brightfield imaging with binary SVM

In the brightfield analysis, optical flow, as described in Chapter 2 Section 2.3.1, was used to generate motion vectors representing iPS-CM contractions (**Figure 5.3A**). Using principal component analysis (PCA) as seen in Chapter 2 Section 2.4.4, we summarized these motion vectors into a contractile profile that contained distinct peaks that represent the contraction (positive PCA values) and relaxation (negative PCA values) phases (**Figure 5.3B**). A total of 12 parameters or attributes describing the contraction and relaxation phases of the contractile plots were derived as seen in **Table 1** and inputted for the machine learning.

Examined Parameters

1.	Contraction duration	7.	Time from max peak to baseline of contraction
2.	Relaxation duration	8.	Time from max peak to baseline of relaxation
3.	Contraction amplitude	9.	Area under the curve of contraction
4.	Relaxation amplitude	10.	Area under the curve of relaxation
5.	Time from baseline to max peak of contraction	11.	Frequency
6.	Time from baseline to max peak of relaxation	12.	Total duration

Table 1.1 Parameters derived from PCA contractile plots

For the machine learning algorithm, a machine is trained with data to create an optimal model with generalizability. SVM classifies the data points into two groups (e.g. normal and abnormal cardiomyocyte behavior) by creating a decision boundary that separates the two groups. The model is evaluated by classifying unseen or withheld data. This evaluation yields an accuracy value (SVM accuracy) that reflects the effectiveness of the model. The percentage accuracy represents the ability to identify an effect (e.g. 98% represents out of 100 samples, the machine can correctly classify 98 of the instances). In the absence of cardioactive compounds, we would expect the accuracy of the machine learning to be random and therefore generate a SVM accuracy of approximately 50%.

Each of the cardiomyocyte contractions was then regarded as an individual sample for the machine learning (ML) analysis. Support vector machine (SVM), a classifying ML algorithm, was implemented to discern between normal and abnormal cardiomyocyte contractile profiles. As most biological data do not have linear trends, a non-linear kernel, radial basis function, was chosen for SVM. The classification between the contractions of the baseline measurements and those of a given drug concentration was accomplished by randomly separating the data into a training set and a test set. The data in the test set was withheld from the training process and only used to evaluate the model. The two sets were formed by first randomly grouping one third of the wells and the corresponding contractions of that drug condition into the test set. To ensure that the test set has equal number of baseline and drug samples, the baseline measurements for one ninth of the wells were randomly allocated for the test set. The reason was that the number of baseline measurements for each well outnumbered each drug condition of that corresponding well three to one. The rest of the wells and respective contractions were used as the training set. Within the training set, a 5-fold cross validation was performed to optimize the parameters for

the generated SVM model. The optimized SVM model was then used to classify the test set. The SVM accuracy of the model was calculated by the ratio of correct classifications to the total classifications for the test set. To account for potential sampling bias, this process was performed 50 times and the reported SVM accuracy was the average of all the runs. With this process repeating numerous times and having random allocation each time for the test and training sets, the size of each respective set varied from run to run. For the baseline measurements, each well had approximately 9 contractions per video acquisition. With these numbers of contractions, the training set used for the SVM classifier had at least 200 samples.

5.3.5 Longitudinal and placebo studies

To ensure that the experimental setup (i.e. stage top incubator), time, and other external factors did not significantly impact the behavior of iPS-CMs, a longitudinal experiment was performed. iPS-CMs were recorded with both the GCaMP6 method and brightfield method for a total of 150 minutes at intervals of 30 minutes. In the analysis of the GCaMP6 signals, there were no changes in the beating rate and SR_{90}, indicating stability in the iPS-CM behavior during the length of the experiment. For the brightfield method, the SVM classification was performed by grouping the first three measurements (0, 30 and 60 minutes) as the baseline control in a similar fashion to the GCaMP6 analysis. The baseline control was then compared to the 90, 120 and 150 minute time points. Corresponding SVM accuracies of 48.64 ± 1.51, 48.22 ± 1.57, and 49.67 ± 1.41% were calculated (**Figure 5.4A**), which are consistent with no longitudinal effect.

The purpose of the placebo experiment was to evaluate the drug delivery process and serve as the vehicle controls. In each placebo condition, 10 μL of RPMI/B-27 media, the vehicle for drug treatment, was added to the iPS-CMs, for a total of four placebo deliveries. Analysis with the GCaMP6 method indicated no change in beating rate and SR_{90} values when compared

to the three baseline measurements taken prior to the placebo treatments. In the brightfield method, the SVM accuracies were 48.75 ± 1.01, 46.86 ± 1.19, 50.40 ± 0.98, and 55.67 ± 1.03% respectively for each of the placebo treatments (**Figure 5.4B**), again consistent with no effect. The data from both the longitudinal and placebo studies suggested only small and negligible, variations in iPS-CM behavior over time. Thus, the drug delivery process had no significant impact on the behavior of iPS-CMs.

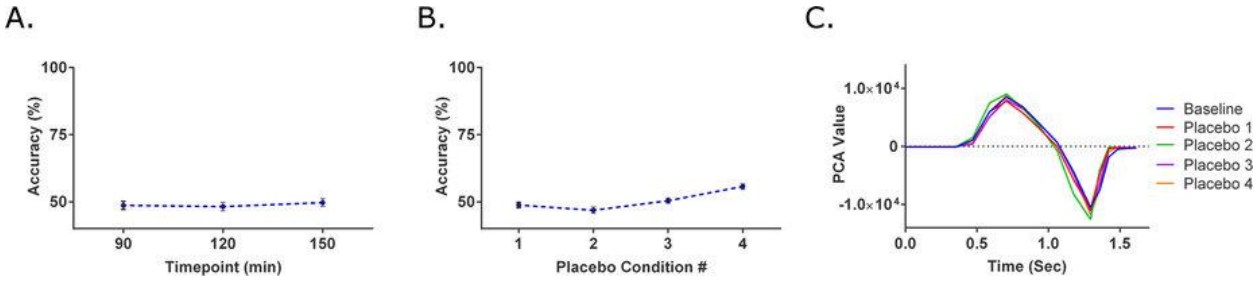

Figure 5.4 Analysis of control experiments: longitudinal and placebo experiment. A) In the longitudinal experiment, behavior of iPS-CMs was monitored for an extended period of 150 minutes at 30 minute intervals after baseline measurements. When the machine was tasked of classifying between the first and last half of the timepoints, the SVM accuracies were approximately 50% as expected ($n = 13$). B) To ensure the drug delivery process had no effects on iPS-CMs, at each placebo condition, 10 µL of media was added to the previous tested condition. The average SVM accuracy of all four placebo conditions was 50.42%, similar to that of the longitudinal experiments ($n = 18$). C) Representative traces of the contractile profile from the brightfield analysis show no differences among tested conditions.

5.3.6 Screen of cardioactive compounds

E-4031 is a known antiarrhythmic drug that blocks the human Ether-à-go-go-Related (hERG) K^+ channel and subsequently prolongs the QT interval.[85,86] The drug compound was administered to the iPS-CMs at an increasing concentration of 1, 3, 5, 10 and 30 nM. E-4031 induces QT prolongation, which was clearly seen in the contractile profiles generated from the brightfield images (**Figure 5.5A**). At the 10 nM condition, extension of the relaxation phase was seen, consistent with the inhibition of the hERG K^+ channel that contributes to the rapid

repolarization of the cardiomyocytes. The lengthening of the relaxation phase became more evident and dramatic at the next treatment level, 30 nM.

For the brightfield method, the SVM accuracies for concentration levels of 1 nM, 3 nM, and 5 nM (47.38 ± 0.64, 50.45 ± 1.05, and 49.19 ± 1.49%) were similar to the baseline SVM accuracies (48.84%) (**Figure 5.5B**). At the 10 nM concentration, the SVM was able to attain an accuracy of 79.82 ± 0.77%. The SVM accuracy continued to increase to 83.55 ± 1.08% at 30 nM concentration. At the higher concentrations (10 and 30 nM), noticeably higher SVM accuracy values were achieved, suggesting drug-induced effects. These observations were corroborated by the GCaMP6 data, which showed statistical significance among the parameters at 10 and 30 nM. With the GCaMP6 method, a change in beating rate was detected only at 30 nM with a 6.38% decrease (**Figure 5.5C**). The SR_{90} increased by 10.73% and 21.51% for 10 nM and 30 nM respectively (**Figure 5.5D**), which were statistically different from baseline. This separation in accuracy values highlights the utility and applicability of machine learning for drug screening purposes.

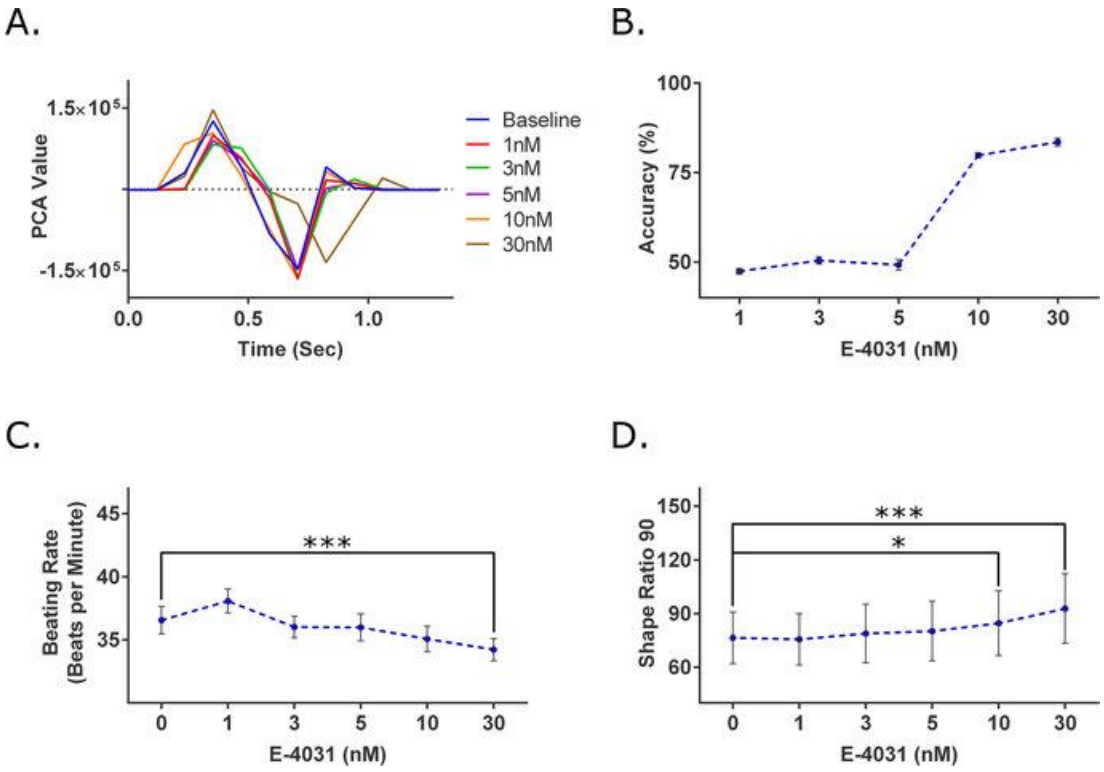

Figure 5.5 Analysis of E-4031, a hERG K^+ channel blocker. A) Representative traces of the contractile profile from the brightfield analysis show a pronounced contraction elongation at the highest tested concentration (30 nM). B) At the concentrations of 1, 3, and 5 nM, the SVM accuracies were approximately 50%, similar to those of the control experiments. For the 10 and 30 nM concentrations, the SVM accuracies increased to 79.82 ± 0.77% and 83.55 ± 1.08% respectively. This increase among accuracies suggest the compound had a cardio-modulating effect on the cells at those given concentrations ($n = 15$). C) Using the GCaMP6 method, significant changes in the beating rate were seen at the 30 nM concentration ($p = 0.0175$). D) For the SR_{90} parameter, significant differences were detected at the 10 and 30 nM concentration ($p = 0.0355$ and $p \leq 10^{-4}$ respectively) ($n = 15$). *$p < 0.05$, ***$p < 0.001$.

Verapamil was the second cardioactive compound to be screened. It is an L-type Ca^{2+} channel blocker that is used therapeutically to treat cardiac arrhythmia.[86,87] The drug compound was administered at increasing concentrations of 1, 10, 50, and 100 nM. Verapamil causes QT shortening[88], which was consistent with the observed decrease in the duration of the contractile profile, first seen at 10 nM (**Figure 5.6A**). At 50 and 100 nM, the shortening effect became more pronounced. In addition, the amplitude of the contractile profiles significantly

decreased, indicating a negative inotropic effect due to decreased levels of intracellular calcium. In the brightfield method, the 1 nM concentration level had a SVM accuracy value of 64.52 ± 1.78% (**Figure 5.6B**). At the 10 nM level, the generated SVM models generated were able to achieve a SVM accuracy value that exceeded 90% (90.64 ± 1.49%). The SVM accuracy values continued to increase for the 50 nM and 100 nM concentration levels (94.32 ± 1.47 and 96.39 ± 1.16% respectively). With the GCaMP6 method, the beating rate decreased by 32.93% and 56.39% for 50 and 100 nM, respectively (**Figure 5.6C**), which were statistically significant. A change in the SR_{90} value, a 45.42% increase, was statistically significant only at the highest concentration of 100 nM, (**Figure 5.6D**).

Interestingly, at 10 nM of verapamil, a SVM accuracy of 90.64% was reported, indicating a change in cardiomyocyte behavior, while the lowest concentration level that had a significant change in the GCaMP6 data was at 50 nM. As verapamil inhibits the L-type Ca^{2+} channel, both the amplitude and duration of the calcium transient would be reduced. Thus, when normalizing by the amplitude to calculate SR_{90}, the decrease in CTD_{90} could be masked by the decrease in amplitude. The shortened contractile profile and decrease in CTD_{90}, may suggest that the effects of verapamil were masked at lower concentrations. If this is the case, the increases in SR_{90} values at higher concentrations indicate that the relative decrease in the amplitude is greater than the decrease in the duration of the calcium transient.

The SR_{90} parameter is prone to inaccuracies in drug compounds that elicit similar and simultaneous changes in the amplitude and duration of calcium transients. However it is necessary as a means of normalization to counteract the photobleaching effect seen in the GCaMP6 method. Attempts to normalize the decay to the control experiments were not possible as the decay pattern among each sample of the longitudinal experiments greatly differed. Due to

unpredictability of the this decay, modeling the decreasing trend as linear or exponential functions dependent on the acquisition number was unsuccessful as well. This photobleaching effect is not unique to the GCaMP6 method, but rather present in most fluorescence-based techniques. Although there are ways to minimize photobleaching effects, there are considerable trade-offs. One method of adjustment is reducing the laser intensity; however, this reduces signal-to-noise ratio and does not remove the photobleaching effects altogether. A line-scan mode of acquisition can significantly reduce photobleaching, but this method eliminates wide field-of-view image acquisition, making it less suitable for high-throughput screening. These degradation in signals further highlight the advantage of using a brightfield method at it is not subject to this photobleaching effect and can be adapted for high–throughput, longitudinal studies on the same set of the iPS-CMs.

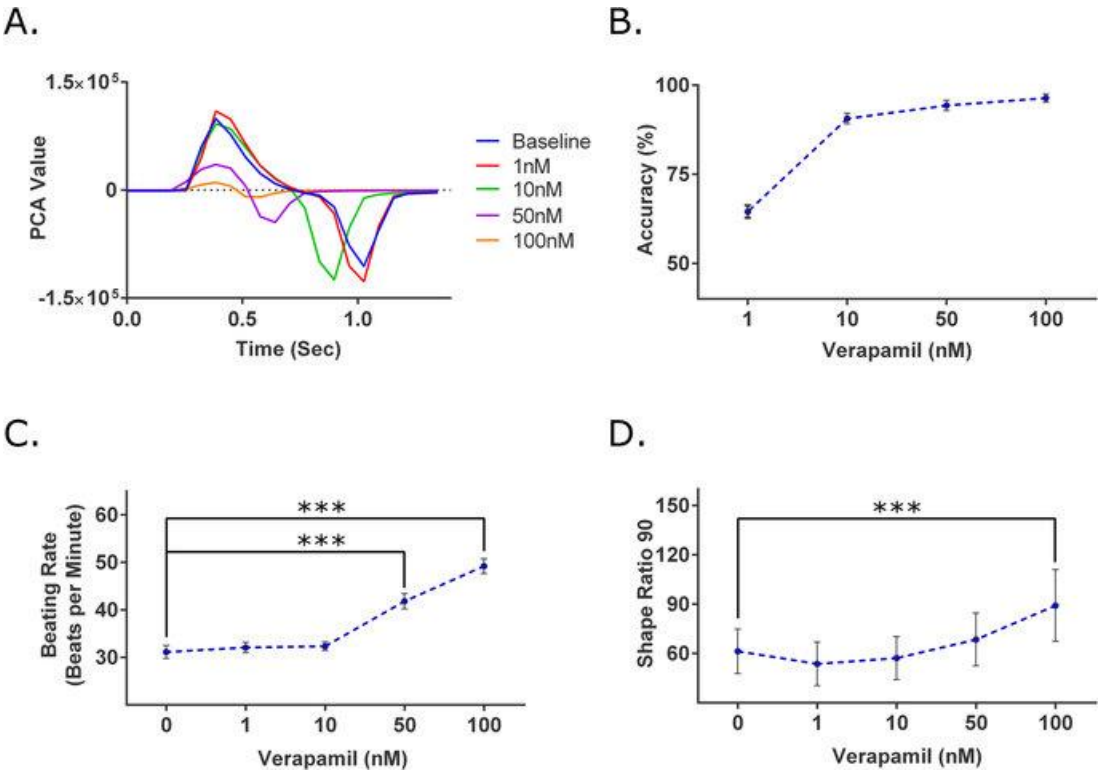

Figure 5.6 Analysis of verapamil, L-type Ca^{2+} channel blocker. A) Representative traces of the contractile profile from the brightfield analysis show the QT shortening effect begin at 10 nM and the negative inotropic effect at 50 nM. B) At 1 nM, the SVM accuracy was 64.52 ± 1.78%. At the 10, 50, and

100 nM concentrations, the SVM accuracies were all above 90%, strongly indicating verapamil's cardio-modulating effect. ($n = 14$). C) In the GCaMP6 method, significant changes were detected at the 50 and 100 nM concentrations ($p \leq 10^{-4}$ and $p \leq 10^{-4}$). D) Looking at SR_{90}, significant differences were only detected at the 100 nM ($p = 8.78 \times 10^{-4}$) ($n = 14$). ***$p \leq 0.001$.

Blebbistatin, a myosin-II inhibitor and a known excitation-contraction decoupler, was the final compound to be screened and was expected to have no changes in the GCaMP6 signal as the inhibition occurs downstream in the proteins that generate the force of contraction, and not intracellular calcium.[89] The drug compound was administered at an increasing concentration of 1, 10, 100, 500, and 1000 nM. The SVM accuracy values for the 1 nM and 10 nM concentration levels were near 50% (44.02 ± 1.45 and 47.38 ± 1.44% respectively) (**Figure 5.7B**). However, at 100 nM, the SVM accuracy increased to 85.08 ± 1.49%. For both 500 and 1000 nM, SVM accuracy values increased to nearly 100% (99.67 ± 0.26 and 99.03 ± 0.57% respectively). Conversely, in the GCaMP6 method, there were no changes for any of the given concentrations (**Figure 5.7C & D**).

As an excitation-contraction decoupler, blebbistatin induces a negative inotropic effect on the iPS-CMs. The expected negative inotropic effects were seen starting at 100 nM (**Figure 5.7A**). At the highest concentration of 1000 nM, contraction and relaxation phases were still distinctly seen. However, the max amplitude of the contraction peak for the 1000 nM concentration was approximately 33-fold smaller than that of the baseline measurement (121.00 PCA value compared 3976.42 PCA value).

As seen above, the predictions of blebbistatin as a false negative in the GCaMP6 method were confirmed as the analysis showed there were no differences in any of the tested concentrations. However, in the brighfield method, a decrease in the amplitude of the contractile profile was seen starting at 100 nM. This experiment clearly demonstrates that methods based on

the electrophysiological profiles, such as patch clamping, fluorescence-based optics, and MEA, are prone to type II errors with drugs such as blebbistatin that decouple excitation and contraction of iPS-CM. Thus, it is crucial in future cardiotoxicity drug screening assays to have a component that monitors contraction and relaxation of the iPS-CMs.

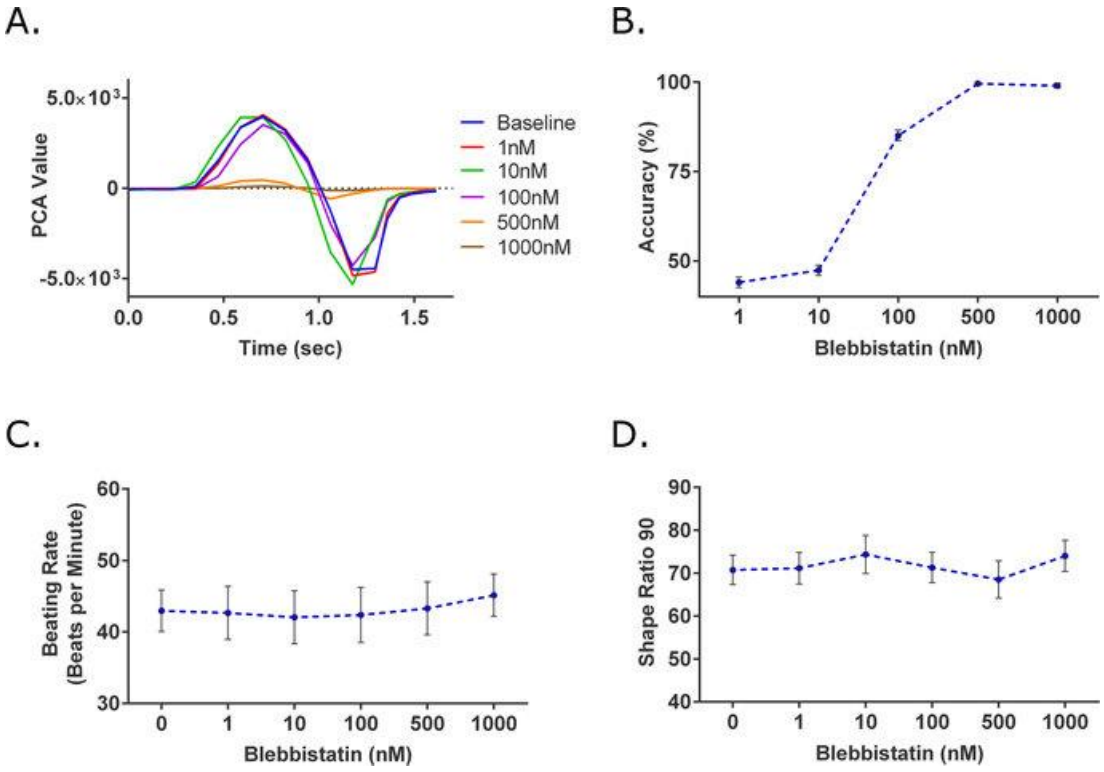

Figure 5.7 Analysis of blebbistatin, a myosin-II inhibitor. A) Representative traces of the contractile profile from the brightfield method showed significant loss of contractility at higher concentrations. B) At 1 and 10 nM the SVM accuracies were near 50%, suggesting minor to no changes in iPS-CMs. At 100 nM, the accuracy increased to 85.08 ± 1.49%. For 500 and 1000 nM, the respective SVM accuracies further increased and were both near 100% ($n = 11$). As expected with the GCaMP6 method, blebbistatin resulted in a false negative with no changes in C) beating rate or D) SR_{90} at any of the tested concentrations ($n = 11$).

In summary, through the monitoring of IPS-CMs exposed to three compounds with distinct cardioactive effects, we presented a screening method that combines brightfield microscopy and machine learning to enable the sensitive detection of changes in the contraction of human iPS-derived cardiomyocytes. This combined method was comparable to – and even superior to – fluorescence readouts. With binary SVM, a singular quantitative index was created.

This index or metric not only summarized the impact of 12 parameters of interest, but also examined any underlying relations or interactions among parameters. This index becomes valuable for high-throughput screening of drug-induced cardiotoxicity by highlighting compounds that have any cardioactive effect on the contractile behavior of cardiomyocytes.

5.4 Multi-class SVM background

Pertaining to multi-class SVM, there are generally two approaches: 1) consider all the data in a singular optimization problem and 2) decompose the task into a set of binary classifications. The former approach will be avoided as it will most likely be inefficient as in most cases no single mathematical function exists to separate all classes of real data sets.[90] With the latter approach, two popular methods (one-against-all and one-against-one) exist. The one-against-all method has a binary classification for each class against all the other classes combined, as seen in **Figure 5.8 (Left Panel)**. A data point would only be classified as a certain class if and only if that class SVM's accepted it while all the SVMs of other classes rejected it. As a result of this method, there exists regions in the feature space where a class cannot be defined. With the one-against-one approach, a binary classification is performed for each pair of classes as seen in **Figure 5.8 (Right Panel)**. The simplest way to then perform a multi-class classification is to select the class that was chosen by the highest number of pair-wise SVMs. In summary, SVM is a powerful classification tool that is effective in high dimensional spaces, not bound to local minimums, and

memory efficient with selected use of training points (support vectors).[91]

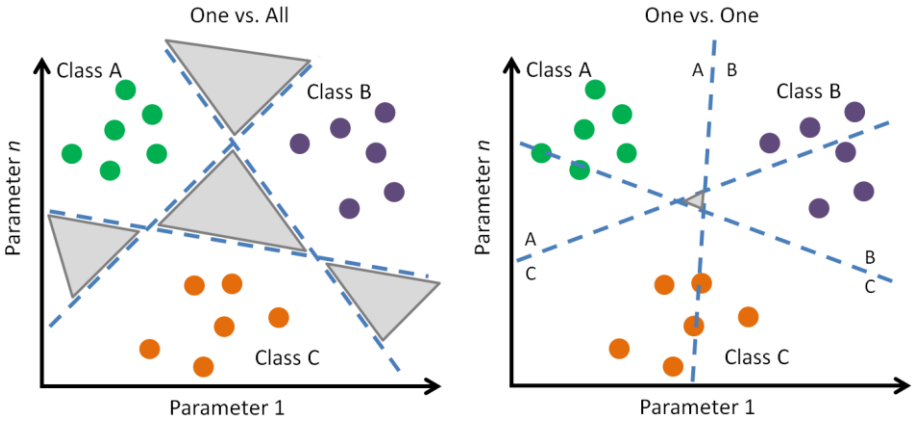

Figure 5.8 Multi-class classification approaches. Multi-class classification can be broken down into a set of binary classifications. (Left panel) In the one-against-all approach, each class is classified against the rest of the classes combined. Upon this, a data point is only classified if one class accepts it and the others reject it. This methodology would yield feature spaces that are not accounted for. (Right panel) In the one-against-one approach, each class is classified with every other class in a pair-wise manner. While this method typically reduces the number of feature spaces that are not accounted for, it may be more resource intensive.

5.5 Prediction of cardioactive compounds' mechanistic actions

5.5.1 Rationale and experimental design

While capable of analyzing vectors generated from optical flow, binary SVM and other machine learning techniques can be readily applied to data of various screening methodologies. This flexibility was demonstrated by applying machine learning to the force measurements of human ventricular cardiac tissue strips (hvCTS) exposed to cardioactive compounds. hvCTSs are 9 mm tissues that model cardiac muscle fiber. These measurements of hvCTS belonged to a database generated by Dr. Ron A. Li's research group of Hong Kong University in conjunction with Novoheart. A unique aspect of these drug screens was that the hvCTSs were paced at four different frequencies. These measurements allowed a perspective on whether cardioactive compounds can influence force-frequency relationships and further highlighted machine learning's ability to analyze a high dimensional datasets. Aside from determining if a compound

is cardioactive, we leveraged the machine learning to create drug classification model that can predict an unknown compound's mechanistic action. In addition, the binary SVM approach was repurposed to explore drug response relationships between compounds. To accomplish these new applications of machine learning, we selected a total of eleven compounds that represented five drug classes (1. Ca^{2+} channel blockers, 2. adrenergic agonists, 3. cardiac glycosides, 4. human Ether-à-go-go-Related Gene (hERG) K^+ channel blockers, and 5. angiotensin converting enzyme (ACE) inhibitors) along with one negative control compound from the database (**Table 5.1**). To the best of our knowledge, we reported for the first time the use of machine learning to establish a drug classification model based on hPSC-CM contractile behavior (half of the selected compounds) and subsequently demonstrated predictive capabilities by having the model classify unknown compounds (which was completely withheld from machine during any training).

Compound Name	MechanisticAction	Tested Range (M)
1) Nifedipine	A L-type Ca^{2+} channel blocker known to shorten action potential duration.[92]	10^{-8} to $3.0x10^{-5}$
2) Mibefradil	A tetralol derivative that blocks both L- and T-type Ca^{2+} channels. Shown to have higher affinity for T-type than L-type channels.[93]	10^{-9} to $3.0x10^{-6}$
3) Isoproterenol	A mixed beta-adrenergic agonists. Compound is nonselective in terms of beta receptors.[94]	10^{-8} to 10^{-4}
4) Norepinephrine	Mixed adrenergic agonist that stimulates both alpha- and beta-receptors.[41]	10^{-9} to 10^{-5}
5) Digoxin	A cardiac glycoside that inhibits that Na^+/K^+-ATPase, resulting in higher intracellular Na^+. Higher Na^+ concentration suppresses the Na^+/Ca^{2+} exchanger and causing the accumulation of intracellular Ca^{2+}.[95]	10^{-8} to 10^{-4}
6) Ouabain	A cardiac glycoside that affects Na^+/K^+-ATPase, which consists of both alpha and beta-subunits. Has a lower affinity for alpha subunits than digoxin and other digitalis glycoside.[95,96]	10^{-8} to 10^{-4}
7) Flecainide	A mixed hERG K^+ blocker that also inhibits Na^+ channels, causing effects on action potential's repolarization and conduction.[92]	10^{-8} to 10^{-4}

8) E-4031	A pure hERG K^+ channel blocker known for pro-arrhythmic potential.[97]	10^{-8} to 10^{-4}
9) Cisapride	A serotonin (5-HT_4) receptor agonists that also inhibits the hERG K^+ channel.[98]	10^{-8} to 10^{-4}
10) Lisinopril	An angiotensin converting enzyme (ACE) inhibitor , which reduces vasoconstriction and lowers blood pressure in patients.[99]	10^{-8} to 10^{-4}
11) Ramipril	An angiotensin converting enzyme (ACE) inhibitor. Unlike lisinopril, ramipril does not block ACE until it is converted by liver.[100]	10^{-9} to 10^{-5}
12) Aspirin	Common nonsteroidal ant-inflammatory drug that has been shown to have no cardioactive effects in screening platforms.[30]	10^{-8} to 10^{-4}

Table 5.1 Compound used in multi-class drug model

5.5.2 Formation of hvCTS and drug treatment

Cardiomyocytes used for the hvCTSs were differentiated from a human embryonic stem cell line (hES2) with a protocol involving the sequential addition of BMP4, Rho kinase inhibitor, activing-A, and IWR-1, a Wnt inhibitor.[101] To form hvCTS, cardiomyocytes at 14-16 post-differentiation were dissociated and allowed to recover for 2 days. Afterwards, the cells at a density of 1 million cells per strip were combined with an extracellular matrix solution of bovine collagen I (2 mg/mL) and Matrigel (0.9 mg/mL) and human foreskin fibroblasts (10^5 cells per strip). The cell-matrix solution (100 uL per tissue strip) was injected into a PDMS device and placed in an incubator (37 °C and 5% CO_2). Formed tissue strips were fed with DMEM supplemented with 10% calf serum, 1% penicillin-streptomycin and 0.1% amphotericin B. The PDMS device contained flexible vertical posts of which the tissue anchors to and therefore shifts in position as the tissue beats. Contractile force measurements were captured with a high speed (100 fps) CCD camera while custom LabVIEW software tracked the centroid movement of the flexible pole tips. Force was derived from the deflection of the PDMS poles by the elastic beam

bending equation. This results in $F = \frac{3\pi E R^4}{2a^2(3L-a)}\delta$, where F, E, R, L, a and δ represent force of tissue contraction, Young's modulus of PDMS, radius of posts, length of posts, height of the tissue on the post and measured tip deflection respectively.[102] A custom MATLAB script was used to calculate 17 parameters that described the overall shape of the force traces for each contractile event (e.g. amplitude of curve) as seen in **Table 5.2** and **Figure 5.7**. As some of the parameters are frequency-related (e.g. captured frequency), the calculated parameters for the last contractile event of each data acquisition was removed from the analysis.

Examined Parameters

1.	Desired pacing frequency	7.	Area under the curve of decline from max force to 95% cutoff	13.	Area under the curve of decline from max force to 50% cutoff
2.	Captured pacing frequency	8.	Max change of force over time (ΔF/ΔT) of contraction phase	14.	Duration of rise from 25% cutoff to max force
3.	Max force generated (Amplitude)	9.	Max change of force over time (ΔF/ΔT) of relaxation phase	15.	Duration of decline from max force to 25% cutoff
4.	Duration of rise from 95% cutoff to max force (contraction phase)	10.	Duration of rise from 50% cutoff to max force	16.	Area under the curve of rise from 25% cutoff to max force
5.	Duration of rise from max force to 95% cutoff (relaxation phase)	11.	Duration of decline from max force to 50% cutoff	17.	Area under the curve of decline from max force to 25% cutoff
6.	Area under the curve of rise from 95% cutoff to max force	12.	Area under the curve of rise from 50% cutoff to max force		

Table 5.2 Parameters derived from force traces of hvCTS

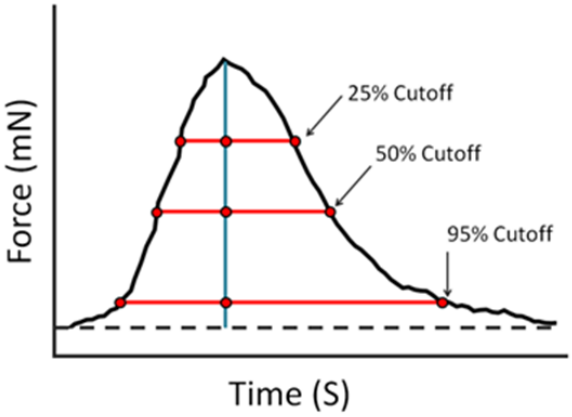

Figure 5.9 Cutoffs in force traces of hvCTS. Green line represents the amplitude. The left of the amplitude line is the contraction phase. The right of the line is the relaxation phase.

After 7-8 days post tissue formation, hvCTS were exposed to drugs for pharmacodynamic analysis. The test compounds of cisapride, digoxin, E-4031, isoproterenol, mibefradil and ouabain were purchased from Sigma-Aldrich, while flecainide, lisinopril, norepinephrine and ramipril were provided by Pfizer. Compounds were initially re-suspended in DMSO and subsequently diluted in water for final concentrations composed of less than 0.1% (vol/vol) DMSO. All tested concentrations are reported in **Table 5.1**. The PDMS device containing the hvCTS was placed onto a heated stage (37° C) under a dissecting microscope. Before either vehicle or drug addition, the media was replaced with DMEM containing high glucose (4.5 g/L) and HEPES without phenol red. Drug doses were added to a tissue in consecutively increasing manner up to 10 concentrations with 3 minutes in between measurements. Vehicle doses containing only water were applied similarly. A pulse stimulator (AMPI Master-9) connected to platinum wires electrically paced the hvCTS with a monophasic electric field of 5 V/cm with a 10 ms duration. Force-frequency response was probed at each concentration for the range of unstimulated, 0.5, 1, 1.5 and 2 Hz.

5.5.3 Multi-class classification

To establish the drug classification model, we first determined which concentration of a chosen compound to add to the library. We gauged each compound's level of cardioactivity by utilizing binary SVM as we did in Chapter 5 Section 4.[103] To normalize for the increasing variation seen in hvCTS contractile behavior during the later serial additions of the vehicle studies, the SVM was performed between each concentration of a compound and the vehicle data from the corresponding serial addition number in which the concentration was achieved. For example, if a hvCTS was exposed to a cumulative 10 nM of compound on the 5^{th} serial addition, the collected data would be compared to the vehicle data recorded at the 5^{th} serial addition. Similar to our previous study, a non-linear kernel, radial basis function, was selected for the binary SVM. The hvCTS data was allocated with one third representing the test set and the remainder serving as the training set. We maintained a balanced number between the vehicle-treated strips and those exposed to a cardioactive compound of the library (n = 6, 7, 8, 9, or 10). Since the number of vehicle strips (n = 28) always outweighed those treated with drugs, we randomly selected a subset of the vehicle-treated tissue strips that equaled in number for each SVM run. Again, we tuned both the box constraint and sigma parameter of each run with a geometric progression approach. To prevent overfitting, we performed a 5-fold cross validation. A total of 50 SVM runs were performed for each concentration to account for the variation and random selection of data sets. It should be noted that if more than half of the tissue strips become unresponsive to the electrical stimulation at a given concentration, the SVM accuracy for that condition was automatically designated as 100% and binary SVM was not performed.

In order to determine whether a concentration of a compound was inducing cardioactivity in the hvCTS, a non-cardioactive benchmark was first established by having a subset of vehicle-

treated hvCTSs act as strips exposed to a non-cardioactive compound and subsequently comparing it to another set of vehicle-treated hvCTSs that served as a control. Thus, SVM accuracies for each serial addition of the vehicle study were generated 50 times for this benchmark. Then SVM accuracies of strips exposed to a drug condition were compared to those of the non-cardioactive benchmark by using a student T-test (a desired α value of 0.05) with a Bonferroni correction (*m*, the number of tests or hypotheses, was dependent on the number of drug additions in a screen). If the adjusted p-value was statistically significant, the drug condition was considered to have incited irregular behavior in hvCTSs and was labeled as cardioactive. The Bonferroni correction was also applied when examining changes in specific parameters.

For the multi-class classification, we then selected the compound concentration that met two criteria: 1) a binary SVM accuracy closest to 85% and 2) at least 6 of all screened tissue strips were still responsive to electrical stimulation. The criterion of 85% served as a reference point where the cardioactive effects of a compound would be prominent, but can still define a generalizable space and boundaries from those of other compounds. The value of 85% was specifically chosen as it was approximately the midpoint between the maximum achievable separation (100%) and a minimum bound that would ensure cardioactivity. We defined the minimum bound as the largest sum of mean SVM accuracy and one standard deviation across all vehicle studies, resulting in a bound of 69.34% (mean SVM accuracy of 53.45% and standard deviation of 15.89%). The criterion of at least 6 responsive tissue strips was to ensure that within the test sets there were data from at least two strips for all runs. As seen in Figure 1B, we then divided the compounds into two groups, one used to train the multi-class model and one representing ‘unknown’ compounds to be predicted. During this separation it was ensured that each class was at least represented by one compound within the two groups. For the training of

the model, we used an error-correcting output codes (ECOC) approach with the binary learners being SVM. The binary learners were again tuned in regards to the box constraint and sigma parameter. A 10-fold cross validation was performed on the entire model. To confirm the generalizability of the generated models, we randomly pre-allocated a third of the data as a test set prior to the training. Finally, we evaluated the multi-class model with this test set and then asked the machine to predict the classes of the contractile beats derived from the 'unknown' compounds group. Similarly, this multi-class classification and prediction process was repeated for a total of 50 times.

To analyze the performance of the multi-class models, confusion matrices were generated for each of the 50 runs. In a confusion matrix, M, the precision and recall rate for each classifier were defined as the following: $Precision_i = \frac{M_{ii}}{\sum_{j=1}^{n} M_{ij}}$; $Recall_j = \frac{M_{ii}}{\sum_{i=1}^{n} M_{ij}}$. Within each matrix, the precision and recall rate were calculated for each of the classifiers. With these two metrics, the F_1score, the harmonic mean of precision and recall, was calculated to summarize the performance of each classifier. The F_1score is defined as the following: $F_1Score_i = \frac{2 \times Precision_i \times Recall_i}{Precision_i + Recall_i}$. A model that is perfect would achieve a F_1 score of 1. If a model were composed of *s*-number of classes and had random classifiers, the expected F_1 score would be $\frac{1}{s}$. To assess the model as a whole, accuracy, defined as $Accuracy_{model} = \frac{\sum_{i=1}^{n} M_{ii}}{\sum_{i=1}^{n}\sum_{j=1}^{n} M_{ij}}$, was calculated. In summarizing the 50 runs of each model, all the calculated metrics were averaged and a confusion matrix containing the average number of contractile events over all runs was provided. All reported values in Chapter 5 Section 5.5 are in the format of mean + standard deviation. All reported sample sizes (n) refer to independent tissue strips (biological replicates).

5.5.4 Control studies

Although the hvCTSs were examined under temperature-controlled conditions, there was an observable change in contractile behavior of the vehicle-treated hvCTSs upon each serial addition. For example, the relative measured max force (amplitude) increased for all four pacing frequencies by an average of 16.96 $\pm$ 0.83% upon the ninth serial addition (**Figure 5.10B**). To account and normalize for baseline drift, each drug condition was compared to its respective vehicle condition via binary SVM (e.g. measurements of the 7th serial drug addition was compared to those of vehicle-treated hvCTSs at the 7th serial addition). To establish that this methodology would create a benchmark of non-cardioactivity, a subset of the vehicle-treated hvCTSs were randomly selected to model a non-cardioactive compound. Binary SVM was then performed between the subset and a corresponding control group of equal size (*n*). To ensure that the number of hvCTSs in the subset had no effect, the calculations were done with *n* equal to 6, 8, 9, and 10, which matched the range of numbers of striped used in each drug study of the 12 tested compounds. As expected, the SVM accuracy, regardless of the size of *n*, was approximately 50% for all serial additions (**Figure 5.10C**). These results indicated that there were no consistent and distinguishable trends within each serial addition and thus, a reference of non-cardioactivity was created.

To validate this reference of non-cardioactivity, drug screens of aspirin from the database were used as negative controls. Aspirin is known to have no cardioactive effects on hPSC-CMs as this has been demonstrated in various platforms.[30,71,104–106] As shown in **Figure 5.10D**, the SVM accuracies of the aspirin drug screens (n = 6) had an average of 52.85 $\pm$ 1.77% among the 9 serial additions (10 nM to 100 μM). None of the nine conditions were statistically different

from their vehicle counterparts, indicating that the binary SVM detected no drug-induced cardioactivity by aspirin.

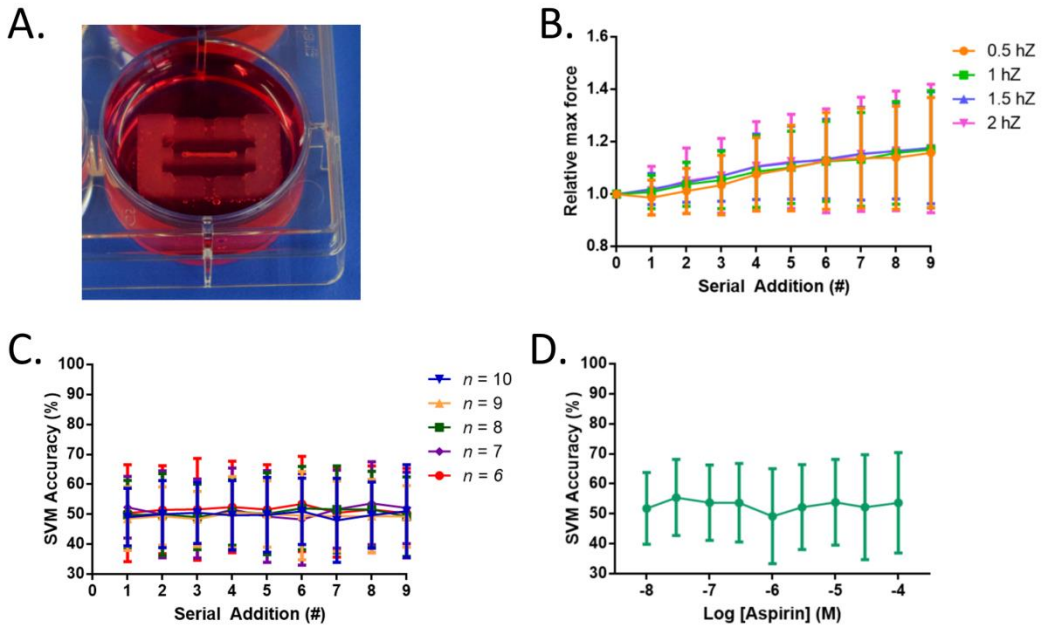

Figure 5.10 Control experiments with hvCTS. A) hvCTSs were formed by the compaction of hPSC-CMS, fibroblasts, and extracellular matrix solution around two PDMS poles. Force was derived from the deflection of the PDMS poles. B) The hvCTSs of the vehicle study exhibited a drift in contractile behavior after multiple serial additions of water. By the 9th serial addition, the max force generated increased by 16.96 + 0.83% for all four pacing frequencies (n = 28). C) To normalize for baseline shifts in the vehicle, data from each drug conditions was compared to its respective vehicle condition (matching serial addition numbers). With this, a benchmark of non-cardioactivity was created with subsets of the vehicle-treated strips being modeled as strips exposed to non-cardioactive compounds. This subset was then compared to other groups of vehicle-treated strips with binary SVM. After 50 runs, the corresponding SVM accuracies served as the benchmark. The study showed that the number of tissue strips in the subset (n = 6, 8, 9, or 10) had no effect as the SVM accuracies for all conditions were approximately 50% for all serial additions. D) To assess non-cardioactivity benchmark, the data of aspirin-treated hvCTSs indicated no statistical difference from the vehicle study with an average 52.85 $\pm$ 1.77% among the tested range (n = 6).

5.5.5 Drug classification model

In setting up the drug classification model, the eleven compounds were compared to vehicle-treated tissue strips with the aforementioned binary SVM approach. At one or more of the tested concentrations, all but two compounds, lisinopril and ramipril, had SVM accuracies that were greater than those of the respective vehicle studies with statistical significance (**Figure 5.11J & K**). The ACE inhibitors, lisinopril and ramipril, did not have detectable cardioactive effects on hvCTS contractility, consistent with the results of other platforms.[105,107] These non-cardioactive results may have been anticipated as ACE inhibitors are primarily known to effect cardiovascular function through the relaxation of vascular smooth muscle and subsequent regulation of blood pressure, which is not present in the studied tissue model.[99] Therefore, the ACE inhibitor class was therefore removed from the model resulting in a four class system. Overall, hvCTSs paired with the binary SVM approach demonstrated the capability in determining if a compound was cardioactive with great accuracy.

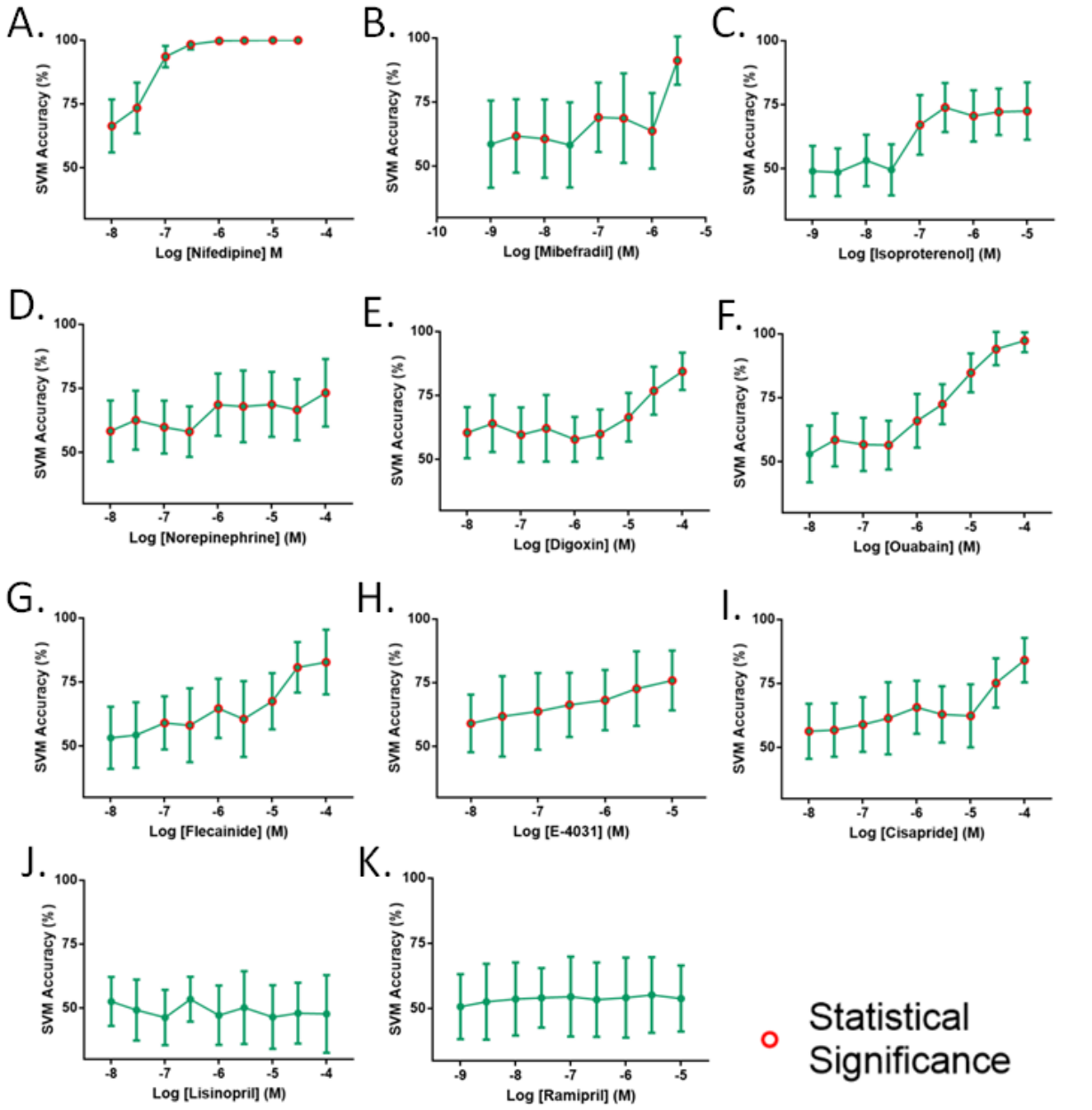

Figure 5.11 Level of cardioactivity with screened compounds. Binary SVM was performed on the 11 compounds including: A) nifedipine ($p \leq 0.0063$; $n = 10$) , B) mibefradil ($p \leq 0.0063$; $n = 6$), C) isoproterenol ($p \leq 0.0055$; $n = 10$), D) norepinephrine ($p \leq 0.0055$; $n = 8$), E) digoxin ($p \leq 0.0055$; $n = 9$), F) oubain ($p \leq 0.0055$; $n = 10$), G) flecainide ($p \leq 0.0055$; $n = 8$), H) E-4031 ($p \leq 0.0071$; $n = 8$), I) cisapride ($p \leq 0.0055$; $n = 9$), J) lisinopril ($p \leq 0.0055$; $n = 8$), and K) ramipril ($p \leq 0.0055$; $n = 7$). Red circles indicate statistical significance in comparison to vehicle-treated hvCTSs. All listed p-values are already adjusted with a Bonferroni correction.

Mibefradil, norepinephrine, ouabain, and cisapride were chosen to represent the 'unknown' compound group that the model would predict on. Mibefradil and cisapride were selected in particular as both compounds received market approval and were subsequently withdrawn.[62] Thus, nifedipine, isoproterenol, and digoxin were chosen to represent the Ca^{+2} channel blocker, adrenergic agonist, and cardiac glycoside classes respectively. As both flecainide and E-4031 exhibit hERG K^+ blocking capabilities, the impact of having either compound represent the hERG K^+ blocker family was evaluated by generating the multi-class model under three different conditions: 1) flecainide as only representative, 2) E-4031 as only representative, and 3) both flecanide and E-4031 as representatives.

As previously mentioned, a subset of the data was always withheld from the machine prior to training in each of the runs. This withheld set quantified the generalizability in the models and ensured that overfitting had not occurred. Upon asking the machine to classify these test sets, the multi-class models demonstrated good generalizability by being able to correctly classify itself at an average accuracy rate of 76.09 $\pm$ 6.43, 78.29 $\pm$ 5.34, and 73.61 $\pm$ 5.19% for the flecainide only, E-4031 only, and flecainide & E-4031 conditions respectively (**Figure 5.12**).

In all three conditions, the multi-class models behaved similarly in that both the nifedipine and isoproterenol classifiers performed the best by always achieving the highest F_1score values. This performance indicates that the data points of the nifedipine and isoproterenol compound occupied very distinct dimensional spaces, allowing for the binary learners to more accurately separate these compounds from others. At the same time, digoxin and the compounds representing the hERG K^+ blocker had the lowest F_1score values in all three conditions. These values would indicate that the data points of these compounds may occupy spaces that are near one another and possibly overlapping, making it more difficult for the

learners to separate between them. As a perspective of the quality of model performance, if there were absolutely no discernable differences among the four compounds for the machine to use, the expected values for precision, recall, and accuracy would be a rate of 25% (F_1score would be 0.25). Thus, the multi-class models created in all three conditions demonstrated good generalizability. In addition, as all three models behaved similarly, this would suggest that the choice of compound representing the hERG K^+ blocker family had minimal effect on setting up the drug classification model.

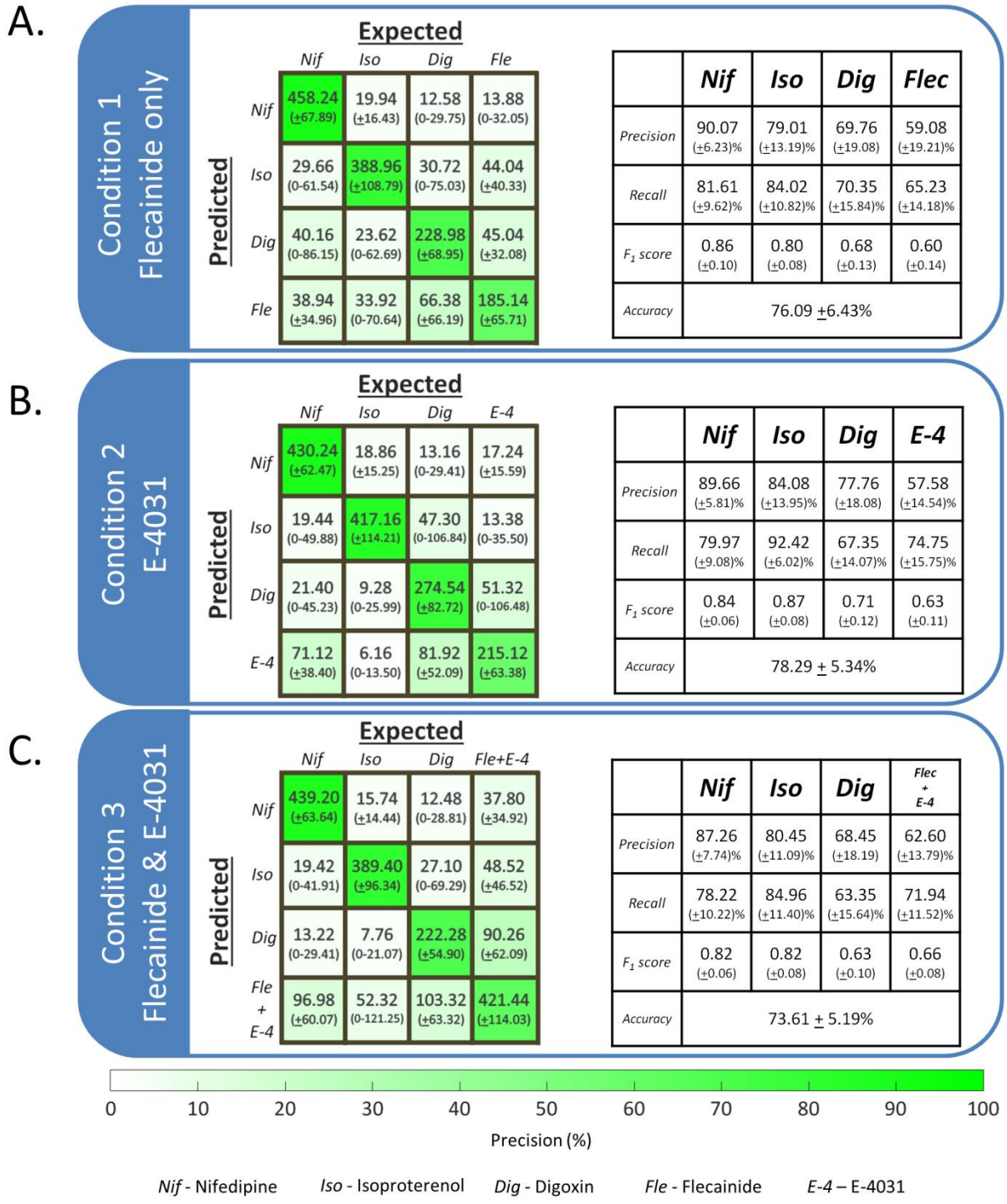

Figure 5.12 Generalizability of drug classification models. A) Condition 1: Flecainide was the representative compounds of the hERG K^+ blocker family. Once the model was generated, its generalizability was evaluated by having it classify a withheld test set composed of compounds used to define the model. (Left panel) The confusion matrix displays the average number of classified contractile events over 50 runs and is imposed with a color scale that indicates precision rate. (Right panel) Metrics evaluating the performance are summarized in table. Metrics indicated good predictability as F_1 scores

were above 0.6 for all classifiers. B) Condition 2: E-4031 was the representative of the hERG K^+ blocker family. (Left panel) Confusion matrix indicated that all compounds were being correctly classified to themselves as the diagonal of the matrix had the highest precision rate. (Right panel) Metrics indicated similar performance between condition 1 and 2. C) Condition 3: Flecainide and E-4031 were the representatives of the hERG K^+ blocker family. (Left panel) Confusion matrix indicated no major effect on generalizability by having two compounds define a class. Precision rate was highest among the diagonal of the matrix. (Right Panel) Similar to condition 1 and 2, F_1 scores were all above 0.6 indicating good generalizability of model.

5.5.6 Prediction on unknown compounds

With each condition's drug classification model evaluated for generalizability, the machine was then asked to use each of these models to predict the data from the 'unknown' compounds group. In the first scenario with flecainide as the only hERG K^+ blocker representative, the multi-class model was able to correctly label the four 'unknown' compounds to their corresponding counterparts with an average accuracy of 71.69 $\pm$ 1.96% (**Figure 5.13A**). The four binary classifiers of this model demonstrated overall predictability by all having an average F_1score above 0.6. The cardiac glycoside classifier (trained with digoxin data) had the highest score of 0.78 $\pm$ 0.02 and the Ca^{2+} channel blocker classifier (trained with nifedipine data) had the lowest at a value of 0.63 $\pm$ 0.05, mainly attributed to a recall rate of 54.97 $\pm$ 4.50%.

When the second drug class model (only E-4031 defining hERG K^+ blocker space) was used to predict the 'unknown' compounds, the average accuracy diminished to 65.37 $\pm$ 2.33% (**Figure 5.13B**). This decrease was mainly the result of the contractile events from strips exposed to cisapride being miscategorized. Of the 779 contractile events of from hvCTSs exposed to cisapride, on average, 46.76 $\pm$ 7.00% of the events were incorrectly labeled as hvCTSs affected by a cardiac glycoside. These misclassifications yielded a poor precision rate, 20.51 $\pm$ 11.20%, and subsequently, a low F_1 score, 0.27 $\pm$ 0.11, for the hERG K^+ blocker classifier. As for the classifiers of the other three families, they performed comparably to those of the first condition and all had an average F_1score over 0.6. These results indicate that using only data of hvCTSs

exposed to E-4031 is not sufficient in defining the hERG K^+ blocker family within a multi-class model and enabling that model to correctly predict cisapride's mechanistic action.

In the last condition where the machine was trained with both flecainide and E-4031 representing the hERG K^+ blocker family, the average accuracy was 71.43 $\pm$ 2.09%. All four classifiers had an average F_1score higher than 0.6 (**Figure 5.13C**). Unlike the second condition, the hERG blocker classifier had a precision rate higher than 25% at 66.87 $\pm$ 8.05%. The performance of this multi-class model was very similar to that of the first condition. In both scenarios, the macro-average of the F_1scores was 0.71, demonstrating good predictability. These results suggest that the data points from the hvCTSs exposed to flecainide designated a dimensional space within the model that was similar to those of hvCTSs exposed to cisapride. Finally, the inclusion of E-4031 data with the flecainide data did not negatively impact the multi-class model's ability to correctly predict cisapride's mechanistic action as neither the precision and recall rate fell below 41% as they did in second condition.

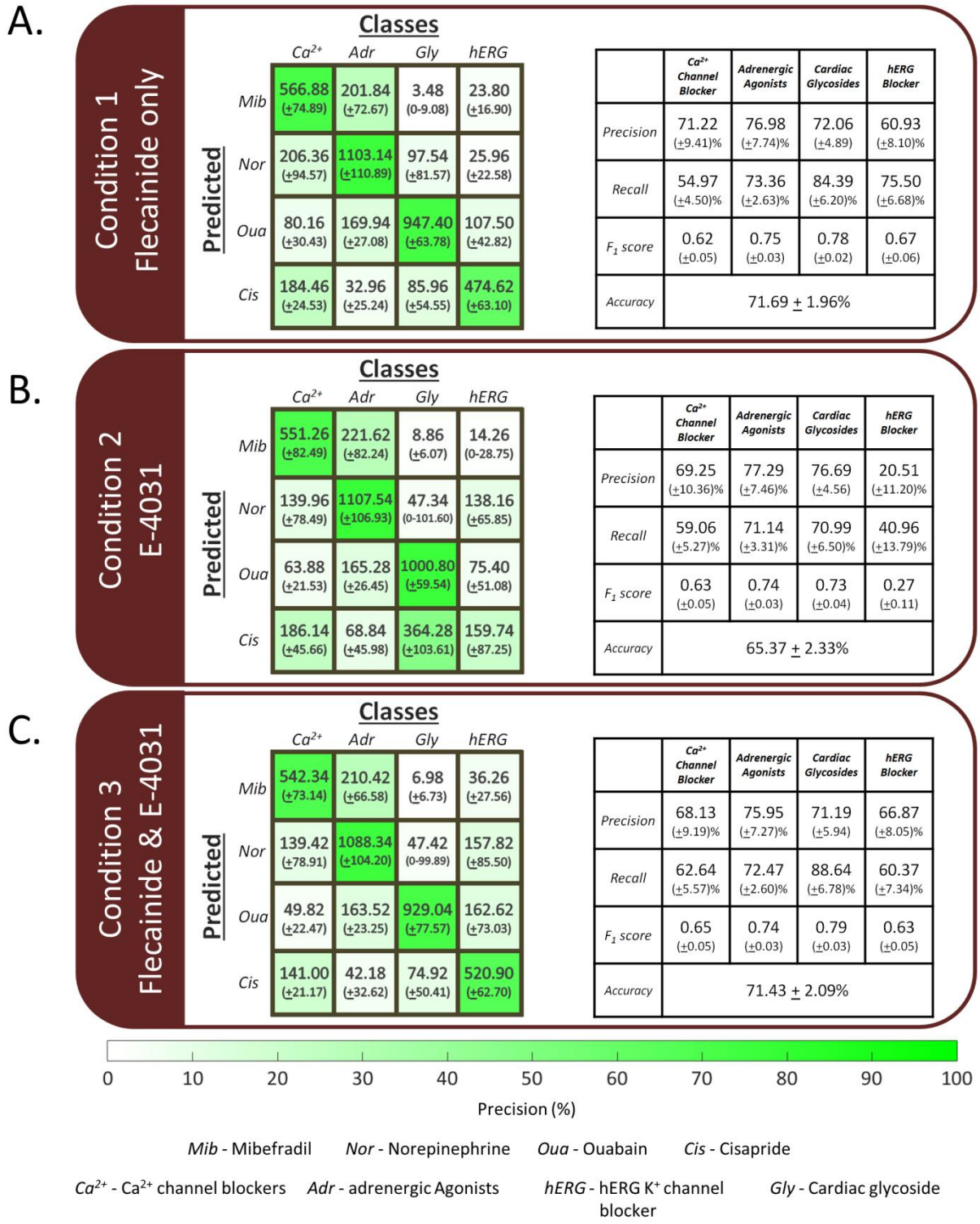

Figure 5.13 Predictability of drug classification models. (A) Condition 1: Flecainide was the representative compounds of the hERG K^+ blocker family. Models of all three conditions were evaluated for capabilities to predict drug families of compounds unseen by the machine. (Left panel) The confusion matrix displays the average number of predicted contractile events from the 'unknown' group over 50 runs. Matrix shows that the 'unknown' compounds were classified to the correct drug family as the

precision rate was highest among diagonal of matrix. (Right panel) Model demonstrated good predictability as the macro-average of F_1 score was 0.71. (B) Condition 2: E-4031 was the representative of the hERG K^+ blocker family. (Left panel) Confusion matrix indicates that cisapride was predominantly being mislabeled as a member of cardiac glycoside family, represented by digoxin. Other three compounds were classified correctly to their respective drug families. (Right panel) The classifier of hERG K^+ blocker class had a F_1 score of 0.27, which is slightly better than a random classifier in a 4 class system (expected F_1 score of 0.25). As the other three classifiers maintained a F_1 score above 0.6, E-4031 did not define a space that is shared with that of cisapride. (C) Condition 3: Flecainide and E-4031 were the representatives of the hERG K^+ blocker family (Left panel) Confusion matrix indicates the model had good predicatability once flecainide was included again. Precision rates are highest among the diagonal of the matrix. (Right panel). The combination of having two compounds define a class did not affect the predictability of model. Condition 3's model performed similar to condition 1 as it had a macro-average of 0.71, as well.

5.5.7 Class relationship metrics

Aside from determining drug class, the concentration of a library compound that induced the most similar cardioactive effects as the compound of interest was determined. This metric was computed by first selecting the compound of interest at a desired concentration and performing a series of binary SVM among the tested range of a library compound. For each concentration of the library compound, the closer the SVM accuracy was to 50%, the more defined spaces of the compounds overlapped and the more similar the cardioactive effects were. This relationship between SVM accuracy and tested concentration range was presumed to behave in a Gaussian manner with the centroid representing the concentration that would elicit the most similar effects. The Gaussian fit was set with 50% as the lower limit and the highest achieved SVM accuracy as the upper limit. If the original SVM accuracies reached the 50% mark and remained around this value for subsequent concentrations, only the first concentration to reach the 50% was included in the fit to accurately model one side of the Gaussian curve.

These relationship metrics are summarized in **Table 5.3**. For example, an estimated 5.35×10^{-5} M of digoxin would be needed to evoke a level of cardioactivity that matches ouabain tested at 1.0×10^{-5} M. Such relationships could be of use as they provide insights on the potency of drugs. In the aforementioned example, ouabain would be considered to be the more potent

compound for that level of cardioactivity as it requires approximately 5-fold lower concentration. Such observation of ouabain's higher potency is corroborated by the results seen in other *in vitro* data.[96,108] The SVM accuracies and Gaussian fits related to these estimations are reported in **Figure 5.14**.

Compound (M)	Predicted Class	Estimated Similar Concentration (M)
Mibefradil ($3.0x10^{-6}$)	Ca^{2+} channel blocker	Nifedipine ($1.28x10^{-7}$)
Norephinephrine ($1.0x10^{-5}$)	Adrenergic agonist	Isoproterenol ($1.44x10^{-6}$)
Ouabain ($1.0x10^{-5}$)	Cardiac glycoside	Digoxin ($5.35x10^{-5}$)
Cisapride ($1.0x10^{-4}$)	hERG K^{+} channel blocker	Flecainide ($1.03x10^{-5}$)

Table 5.3 Summary of estimated drug response relationships of all four classes.

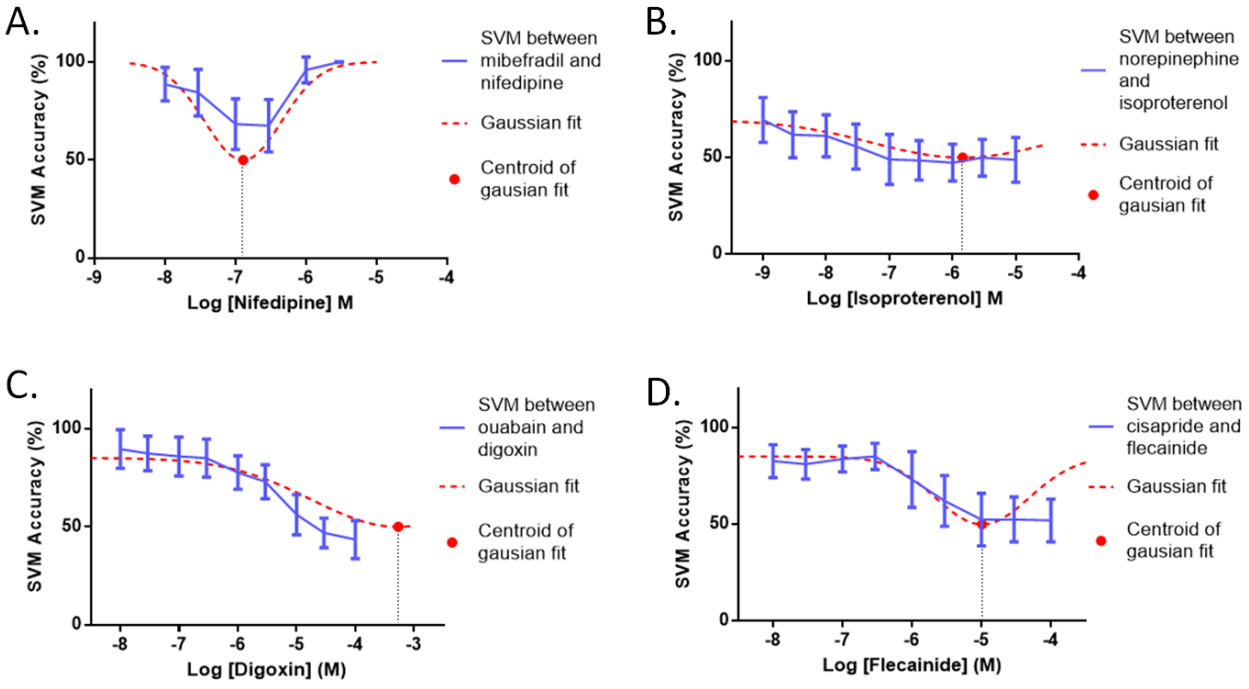

Figure 5.14 Drug response relationships of 'unknown' compounds to compounds representing predicted classes using a binary SVM approach. Solid blue line indicates the binary SVM accuracy between a

concentration of the 'unknown' compound and each tested concentration of the representative compound. Dotted red line indicates a fitted Gaussian curve where the centroid represents the concentration at which the representative compound elicits the most similar response in the hPSC-CMs as the condition of the 'unknown' compound. A) mibefradil and nifedipine (Ca^{2+} blockers), B) norepinephrine and isoproterenol (adrenergic agonist), C) oubain and digoxin (cardiac glycoside), and D) cisapride and flecainide (hERG K^+ channel blocker).

5.5.8 Improvements to predictability of drug model

While the F_1 scores of the established models already signified good predictability, there are still opportunities to further improve model performance and obtain F_1 scores closer to 1, indicating better precision and recall rates with reduction in errors. The data in this study already suggests ways to do so. One method is to define each drug family with multiple compounds. By having only one compound define a class, there is a risk of only defining a partial space that the drug class entails. The data of E-4031 exemplified this when it was tasked of defining the hERG K^+ blocker family. E-4031's defined space did not match that of cisapride's, another hERG K^+ blocker, causing classification of cisapride to be closer to that of the cardiac glycoside family. The inclusion of flecainide, a mixed hERG blocker, with the E-4031 in the definition of the class allowed for the correct prediction of cisapride without adversely affecting the predictive capability of the remaining classes. Although the addition of E-4031 to the hERG blocker definition does not necessarily improve the predictive capability with respect to cisapride classification, establishing a more expansive dimensional space to define the hERG class may improve prediction of other unknown hERG blockers that have effects more similar to E-4031 than flecainide. These results also suggest the potential of having subgroups within classes of the model, which can be achieved through a series of multi-class classifications. For instance, a compound can be predicted as Ca^{2+} channel blocker in the first classification. Within this family,

the compound can be subsequently categorized into a subgroup defined by frequency-dependent cardioactivity.

In **Figure 5.15A**, a benchmark of non-cardioactivity was established by having a subset of the vehicle-treated strips represent a non-cardioactive compound and then asking the machine to separate this group from other vehicle-treated strips. The number of vehicle-treated strips was altered to see if this would affect the separation. There appeared to be no difference as all conditions had an average SVM accuracy of approximately 50%. However, as the number of tissue strips in each data set increased from 6 to 10, the standard deviation of the results decreased. Such results are comprehensible in that if a machine is provide more data, it would be able to create a more generalizable model and one that is less likely to overfit. Therefore, to further advance the predictability of the model, a larger number of hvCTSs per drug screen should be used for future models.

Improvements of the multi-class drug models can also be achieved from enhancements of the hvCTSs and the acquisition system. In particular, the sensitivity of this system to positive inotropic compounds can be increased by addressing two issues, the maturity of stem-cell derived cardiomyocytes and the shifting baseline of vehicle-treated strips. Studies have shown that hPSC-CMs elicit a minimal to non-existent response to certain positive inotropic compounds, such as beta-adrenergic agonists, because of immature phenotypes.[39,43,44] When these diminished responses are paired with a baseline that has increasing contractility over time, positive inotropic effects of a compound can get masked and harder to detect. This impediment is apparent in the isoproterenol drug screen. In **Figure 5.15B**, hvCTSs exposed to 10 μM of isoproterenol and paced at 0.5 Hz had a similar increase in max force to that of respective vehicle-treated strips (10.42 $\pm$ 16.23% and 15.76 $\pm$ 21.05% respectively), suggesting the

compound had no inotropic effects. However, isoproterenol's cardioactive effects manifested in other parameters. For example, the duration of the relaxation phase or time from max force to 95% cutoff decreased by 22.19 $\pm$ 19.35% for the strips exposed to 10 µM isoproterenol, while those of the vehicle-treated strips experienced essentially no change. Even though machine learning was able to leverage these positive lusitropic effects in both binary and multi-class SVM, increasing the sensitivity of the system to positive inotropic effects would yield an even more distinct space for such compounds and subsequently better predictability in the drug classification models. While hvCTSs were already arranged in an anisotropic manner and co-cultured with fibroblasts, they can be further matured through additional techniques: electrical stimulation prior to screens, a tri-culture including endothelial cells, or forced expression of selective proteins.[45–48] As for the stabilization of the baseline, different components of the setup, ranging from pH to CO_2 levels in ambient environment, should be re-evaluated to minimize overall drift within the serial additions.

Interestingly, the hvCTSs treated with cardiac glycosides (digoxin and ouabain) also demonstrated the system's sensitivity to positive inotropes. Typically these compounds induce an increase in amplitude in waveform (Ca^{2+} transients or MEA); however, in this dataset, the strips treated with cardiac glycosides decreased in max force generated (amplitude) as the concentrations increased (**Figure 5.15C**).[47,75,109] Such results could be attributed to cardiac glycoside toxicity or immature phenotype. Studies have shown that above 3 µM of digoxin or ouabain hPSC-CMs in monolayers stopped beating altogether.[70,75,110] In this dataset, the highest concentration applied for both cardiac glycosides was 100 µM. At 100 µM of ouabain, 4 of the 10 treated strips stopped beating at all pacing frequencies.

Similar to isoproterenol, a lack of increase in max force persisted in the strips exposed to lower concentrations of the cardiac glycosides; however, the cardioactive effects of these compounds appeared in the changes of other parameters. Such changes further highlight the need to look at multiple parameters. When the concentration of digoxin increased, the max force decreased while the duration of the relaxation phase increased. If limited to the observation of only these two parameters, one may believe that cisapride and digoxin are related in their cardioactive effects as cisapride-treated hvCTSs experienced similar trends in the two parameters (**Figure 5.15D**). But upon visual inspection of the force traces, it is evident that the compounds have distinct effects on hvCTSs caused by different mechanistic action (**Figure 5.15E & F**). The use of other parameters, such as the area under the curve of the relaxation phase, can easily summarize such differences. Changes in these parameters were clearly unique to the cardiac glycoside family as the ouabain-treated strips were correctly predicted from the other three classes. As seen in this study, machine learning is capable of analyzing all parameters and using those most critical in distinguishing a compound in a truly automated fashion. Because machine learning does not define drug classes with *a priori* knowledge (e.g. guidelines on how parameters are expected to change), the number of drug families and subclasses that can be defined within a model are not limited. This automation is also advantageous when a new drug family needs to be added into the library as no rubric needs to be manually amended and re-evaluated.

While the concept of examining multiple parameters from waveforms has been pursued lately, some studies have suggested that only a few parameters (e.g. peak count) are necessary in assessing a compound's cardioactivity as other parameters are derivatives of the select few and provide no further mechanistic insight.[70,71,111–114] This is primarily true when the hPSC-CMs are spontaneously beating, meaning the force generated is linked to beating frequency. This study's

dataset affirmed the importance of decoupling this force-frequency relationship through the pacing of the tissues. By setting a fixed pacing frequency, any changes to the force waveform can be truly accredited to a compound's inotropic and lusitropic effects. For example, if the nifedpine-treated strips were allowed to spontaneously beat, a positive chronotropic effect would have most likely been observed.[17,43,92,108] Because the hvCTSs displayed a negative force-frequency relationship, a decrease in max force could not be directly linked to chronotropic or inotropic effects or a combination of both. When 0.3 μM nifedipine-treated hvCTSs were paced at 1 Hz, the captured frequency of the tissue was 0.99 $\pm$ 0.01 Hz and the max force decreased by 45.69 $\pm$ 10.42% (**Figure 5.15G**). This paced data confidently confirmed nifedipine had a negative inotropic effect on the tissues. However, a limitation of this study's drug models is the absence of spontaneously beating hvCTSs' responses to cardioactive compounds. This data would provide understanding of a compound's chronotropic effects. Even though the model has already demonstrated good predictability on inotropic- and lusitropic-related data alone, the model would benefit from chronotropic-related data as it would provide more dimensions in which the compounds can further distinguish themselves and yield better predictability.

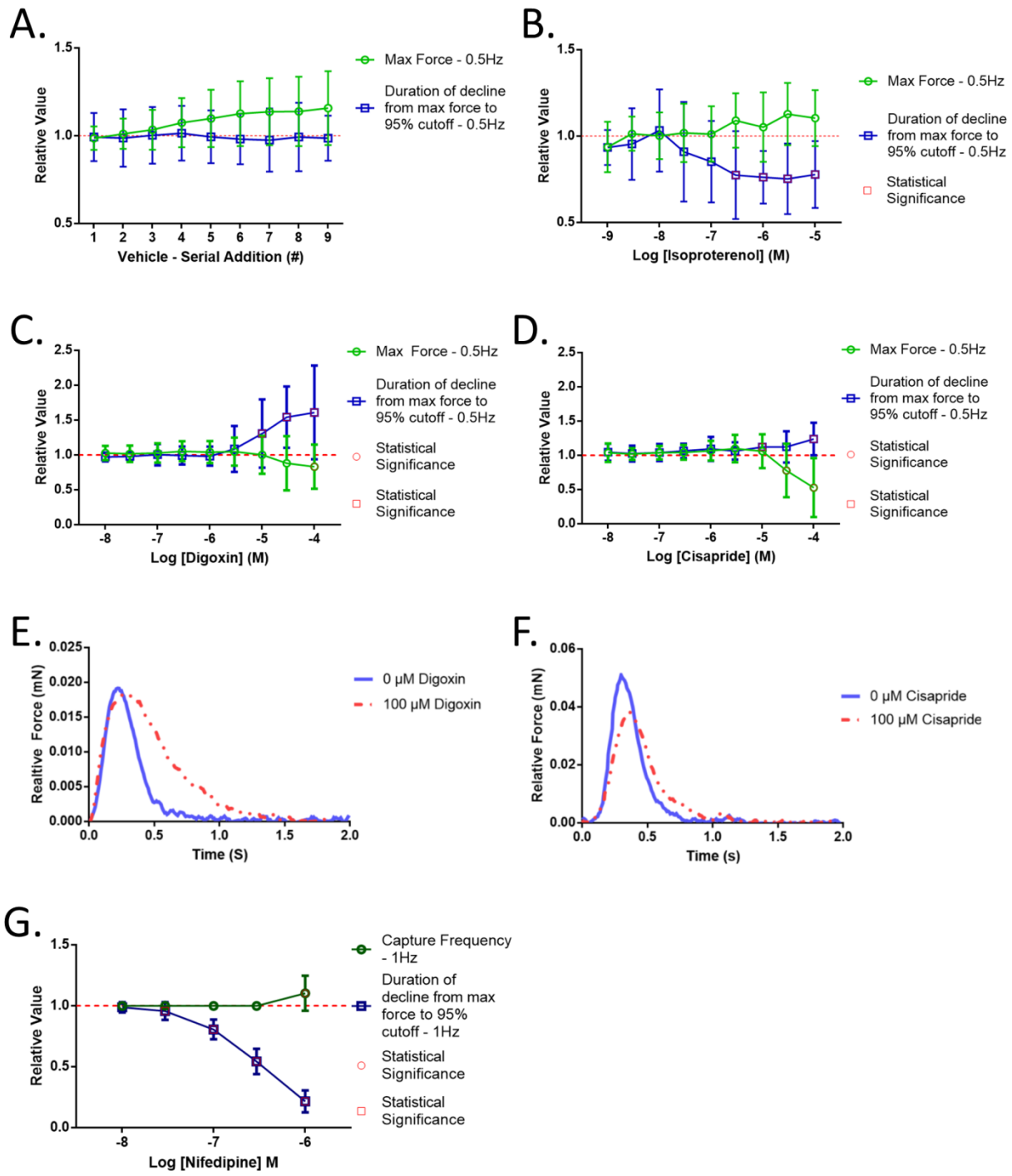

Figure 5.15 Examination of various compounds' cardioactive effects. A) In the vehicle study, hvCTSs paced at 0.5 hZ continually increased in max force generated through subsequent serial additions. The duration of decline from max force to 95% cutoff, relaxation phase, was unaffected by the number of serial additions. (n = 28). B) Isoproterenol-treated hvCTSs experienced an increase in max force similar to the vehicle-treated strips, suggesting no inotropic effects. Isoproterenol's lusitropic effects were apparent as duration of the relaxation phrase decreased with significant differences respective to the vehicle study at concentration range of 3.0×10^{-7} to 10^{-5} M ($p \leq 0.0055$; n = 10). C) Digoxin-treated

hvCTSs (paced at 0.5 Hz) experienced a decrease in max force and an increase in duration of relaxation phase by the highest concentration, 10^{-4} M ($p \leq 0.0055$; $n = 9$). D) Cisapride-treated hvCTSs (paced at 0.5 Hz) experienced similar trends in max force and duration of relaxation phase by the highest concentration, 100 µM ($p < 0.0055$; $n = 9$). E) Representative force tracing of a contractile event from a digoxin-treated hvCTSs (paced at 0.5 Hz) show the distinct cardioactive effects prolonging the duration while increasing the area under the curve of the relaxation phase. F) Representative force tracing of a contractile event from a 100 µM cisapride-treated hvCTSs (paced at 0.5 Hz) show that while cisapride and digoxin have similar trends in certain parameters, the cardioactive effects of the two are visibly distinguishable. G) Nifedipine-treated hvCTSs had capturing frequencies that matched the pacing frequency of 1 Hz from 10-8 to 3.0x10-7 M. During this concentration range, the max force generated decreased by 45.69 + 10.42%. Since the force-frequency relationship was decoupled by pacing the strips, it can be concluded that the decrease in force is attributed to the compound's negative inotropic effects ($p < 0.0063$; $n = 10$). All listed p-values are adjusted with a Bonferroni correction.

5.6 Summary

In this chapter, the utility and flexibility of machine learning was shown through the analyses of data from two different screening platforms, vectors outputted from optical flow of brightfield videos and force traces of hvCTSs. Machine learning applications to cardiotoxicity screening has been primarily *in silico* rather than the assessment of cardiomyocyte functionality to compounds.[115,116] Machine learning techniques offer the advantage of simultaneously evaluating multiple parameters and any underlying relationships, which may lead to better detection of cardioactivity. Without the need for guidelines and rubrics, machine learning can provide information in an automated manner that would facilitate in the streamlining of the drug discovery pipeline. Notably, we have shown that binary SVM can generate a quantitative singular index that describes a compound's level of cardioactivity and provide drug response relationships between compounds. Using multi-class classification, models of drug families were established and used to predict the mechanistic action of unknown cardioactive compounds (which were completely withheld from the machine). While functional, the analyses of both platforms were meant to exhibit the potential of machine learning in providing further insights in the detection of cardioactivity using hPSC-CMs. The basis of the models was an ECOC

approach with the binary learners being SVM. Different binary learners, such as decision trees, should be explored alongside completely different approaches (e.g. neural networks). Other machine learning approaches and techniques may provide additional information relevant to evidence based decision-making for drug development. Importantly, an ideal machine learning technique will need to balance predictive capabilities and use of computational resources.

CHAPTER 6: Analysis of 3D cardiac organoid chambers

6.1 Introduction

Along with platforms differing in their methodology of monitoring hPSC-CM behavior, the tissue geometry in these systems also greatly contrasts. Certain platforms employ hPSC-CMs in a two dimensional manner (e.g. monolayer), while others choose to recapitulate aspects of the three dimensional environment of native myocardium by modeling the cells as cardiac muscle fibers or fascicles.[27,35,46,74] Regardless of geometry, the majority of these platforms have presented adequate capabilities of capturing the effects of chronotropic and inotropic agents within hPSC-CMs. However, there exist compounds where the cardioactive effects become most apparent when observing the heart's ability to pump in a stable and rhythmic manner. Each heart beat is comprised of electrical stimulation of the four heart chambers in a sequential manner. Any disturbances to the electrical propagation can alter pumping functions and more importantly, the amount of oxygenated blood delivered to the body. Compounds, such as dromotropic agents, can perturb the conduction velocity at the atrioventricular (AV) node, leading to arrhythmic events and sudden cardiac deaths.[117,118] Tissues with 2D geometry (e.g. monolayer) or those that model cardiac muscle fibers (e.g. hvCTS in Chapter 5) cannot observe such compounds' effects on pumping mechanism. Thus, there is still a need to create systems that can recapitulate the three-dimensionality of the heart on the level of organs.

Dr. Kevin Costa's research group has shown a way to create bioartificial pumps, referred to as cardiac organoid chambers (COC). These COCs exhibits pumping functions and a geometric shape similar to a chamber of the human heart, which is currently not present in most 3D cardiac organoids. Traditionally to quantify the COC, pressure readouts from a transducer is required. As the readouts are one dimensional, they do not necessarily capture the spatial

changes of the organoid as the electrical propagation occurs. While optical mapping techniques can be performed, the dyes, as mentioned in Chapter 1, can be cytotoxic and prevents longitudinal studies. In this chapter, we show that the brightfield techniques described in Chapter 2 can be readily applied to videos of COCs exposed to a cardioactive compound and provide key spatial information not present in pressure readouts.

6.2 Cardiac organoid chambers

The COC is prepared by casting a gel mixture of collagen, basement membrane matrix, and cells into a cup-shaped mold. Both neonatal rat cardiomyocytes and hPSC-CMs along with respective fibroblasts have been demonstrated with the COC. Prior to the gel polymerization, a silicone balloon catheter with the tip cut off is placed concentrically in the mold and inflated to the desired size. After 24 hours of incubation, the gel and catheter are then placed in medium. Within 7 to 10 days, the gel will have compacted into a network of cardiac tissue around the catheter.[119]

The COCs spontaneously beat and generated cyclic changes in chamber pressure. Via measurements with electrodes, voltage signals with distinct spikes and subsequent slow repolarizations were present. As seen in Figure **6.1A**, a pressure-area loop was formed with a counter-clockwise direction, indicating positive stroke work. To demonstrate the Frank-Starling mechanism, the mean chamber pressure was increased and as a result, the developed pressured from the spontaneous beating increased in a near linear relationship.[119]

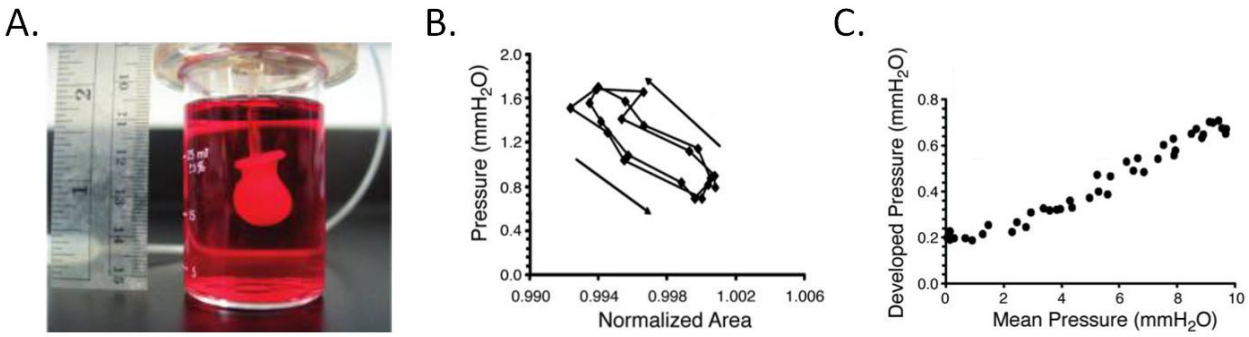

Figure 6.1 Cardiac organoid chamber A) COC after 7 days of incubation. B) Pressure-area curves derived from measurements of the COC. The counter clockwise motion indicates positive stroke work, a pumping characteristic of the human heart. C) As mean chamber pressure increased, the developed pressure within the COC increased. This positive trend indicates a functional Frank-Starling mechanism. Adapted from Lee, E. J., Kim, D. E., Azeloglu, E. U. & Costa, K. D. Engineered cardiac organoid chambers: toward a functional biological model ventricle. *Tissue Eng. Part A* **14**, 215–25 (2008) with permission from Mary Ann Liebert Inc.
.

6.3 Drug responses with COC's

A set of videos capturing the effect of isoproterenol on a spontaneously beating COC were provided for analysis. The COC was formed with 10 million cells and had a diameter on the centimeter scale. The videos were captured at 100 frames per second with a resolution of 1024 x 1024 pixels for a total of 30 seconds. Furthermore, the COC was illuminated by a single light source with a dark background. Isoproterenol was administered to the COCs at an increasing concentration of 10, 100, 1000 and 10^4 nM. Prior to analysis, the COC in each frame was segmented from the dark background (image was thresholded into a black and white image) and superimposed onto a white background with grids. This pre-processing step improved the signal to noise ratio. Afterwards, the videos were processed with the optical flow technique described in Chapter 2 Section 2.3.1. A contractile plot was then derived by performing PCA on the corresponding vectors.

The obtained signals for all tested concentrations are shown in **Figure 6.2**. As expected the beating frequency of the control measurement (approximately 0.6 Hz) increased with the

administered concentration of isoproterenol. At the highest concentration of 10 µM, the beating frequency (0.93 hZ) increased by 1.55 fold, demonstrating the compound's chronotropic effects. In addition, the amplitude of the contraction phase by 10 µM increased by 61.44% relative to the baseline, suggesting greater contractility. These results are consistent with the known cardioactive effects of isoproterenol and were confirmed with the pressure data captured (increase in both frequency and max pressure developed).

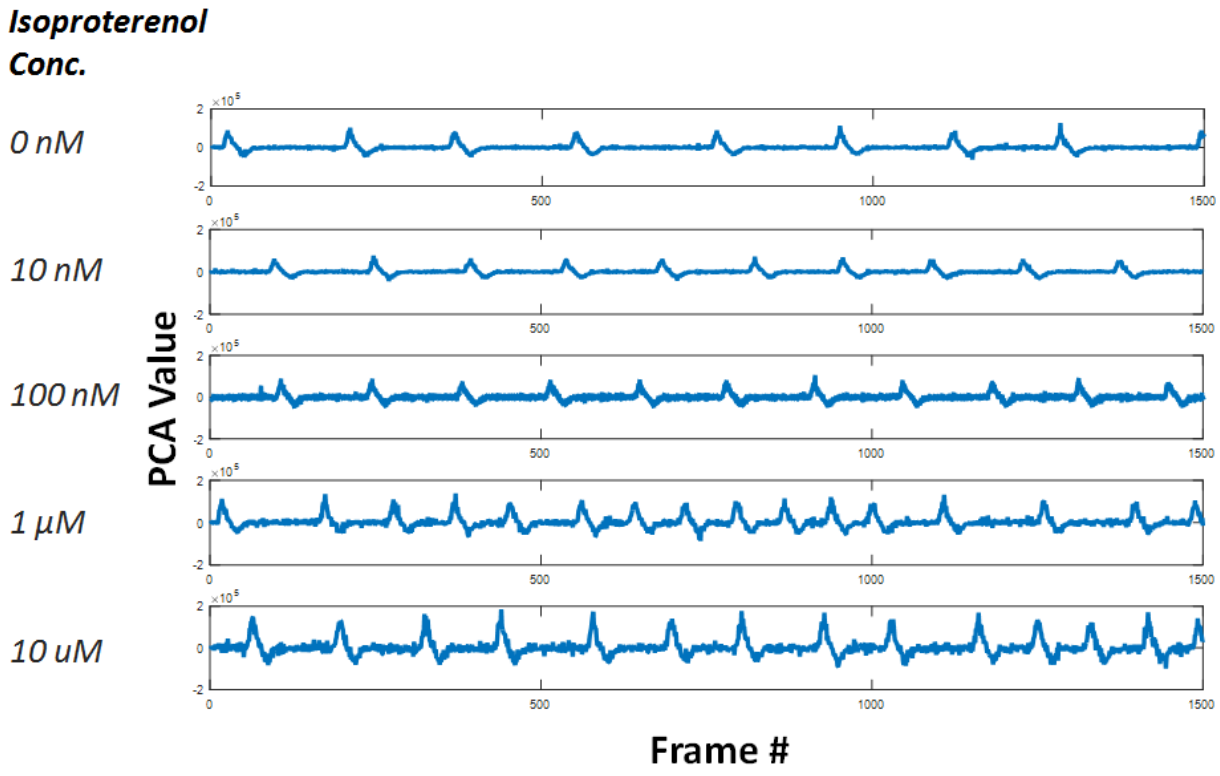

Figure 6.2 PCA analysis of COC exposed to isoproterenol. As the concentration of isoproterenol increases, the beating frequency and amplitude of the contraction phase of the COC increase. Such changes are consistent with isoproterenol's cardioactive effects.

While the PCA analysis of the optical flow vectors complemented the pressure data, it did not provide the spatial information that is missing from the pressure readouts. As a result, we investigated the vectors themselves as they are composed of magnitudes and directionality. To

determine a reference point for analysis, we used the contractile plots and selected the peak of the contraction phase for each contractile event (**Figure 6.3A**). We then aggregated all the vectors of each peak and binned them by their directionality (to the nearest whole degree). In each bin, the magnitudes of the vectors were summed and displayed in a polar coordinate plane as seen in **Figure 6.3B & C**. At the baseline measurement, the COC appeared to prefer two directions (upwards and to the right) at this reference point of contraction. However, at the point, the COC when exposed to 10 μM had a preference for only the upwards direction, indicating that besides beating faster and stronger, the pumping mechanism of the COC was spatially altered.

In order to confirm this, the vectors generated from optical flow were plotted over the images of the COC. In **Figure 6.3D & E**, the frame at which the peak occurred for a contractile event is shown. In this image, it is observed that the bottom of the COC was contracting upward and the right wall of the organoid was distending outward. In the corresponding image that represents the COC exposed to 10 μM of isoproterenol, only the bottom of the organoid was contracting upward with the right wall showing reduced motion. As these images agree with the polar plot, it is evident that the brightfield technique can be applied to the monitoring of COCs and track changes to the organoid's pumping from a spatial perspective. This information can be critical in screening for compounds that disrupt electrical propagation across the cardiac surface (e.g. reentrant arrhythmia) and have its cardioactive effects primarily manifest in the perturbation of the heart's pumping capabilities.

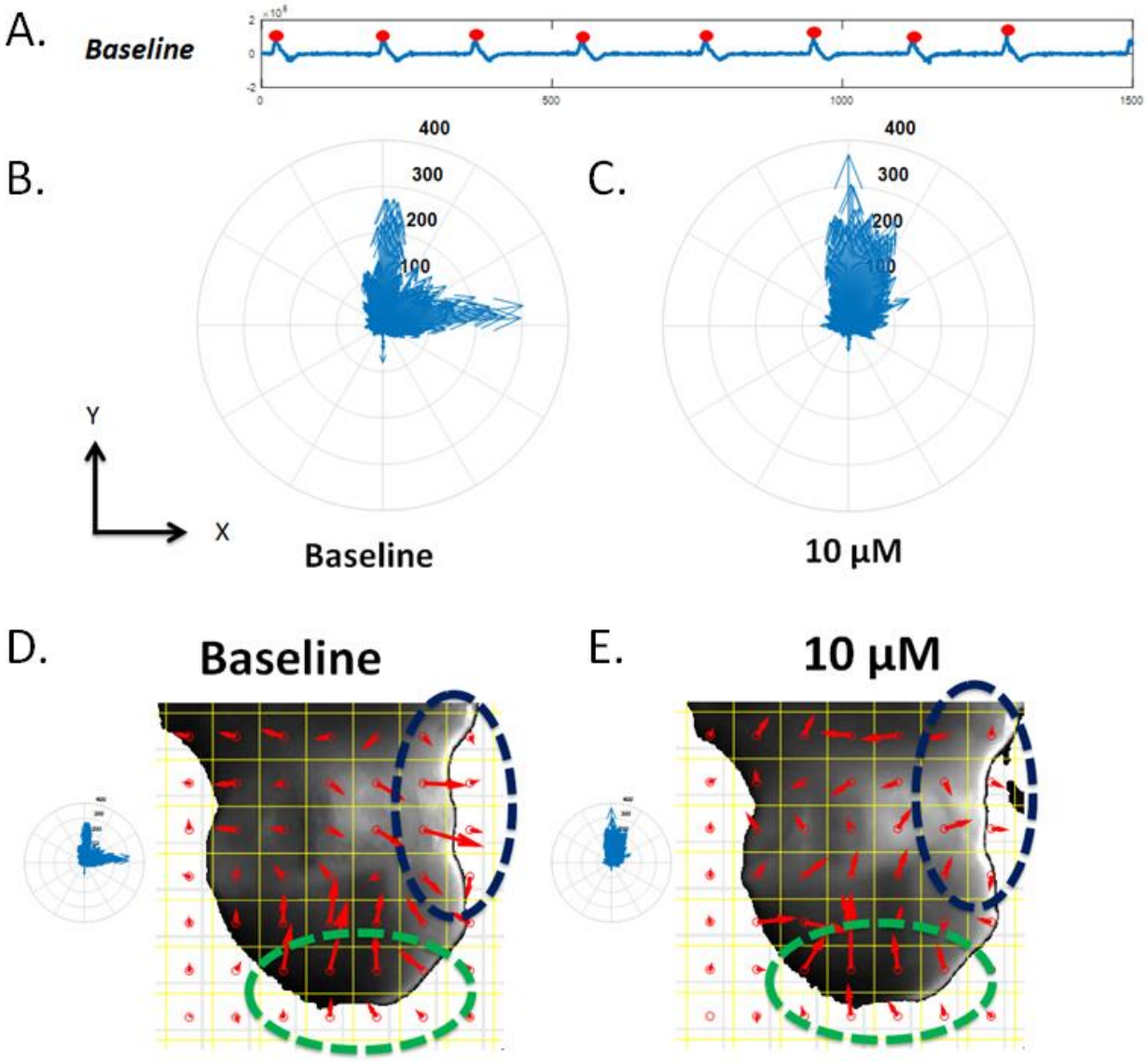

Figure 6.3 Spatial information regarding contraction of COC. A) The optical flow vectors were examined for spatial information to describe the contraction of the COC. A reference point, the peak of the contraction phase, was chosen. B) All the vectors at each peak were binned by their directionality (to the nearest whole degree). In each bin, vectors' magnitudes were summed and displayed in a polar coordinate plane. At baseline, it appears that the COC had two preferential directions, upwards and to the right. C) At 10 µM, only one preferential direction, upwards, was seen indicating changes in pumping pattern. D) Vectors were overlaid over original image. At one of the peaks, the upwards direction referred to bottom of the COC contracting (Green Trace). The rightward direction was the right wall distending out (Blue Trace). E) Visual inspection of the COC exposed to 10 µM isoproterenol at the peak reference point showed that the right wall was no longer distending (Blue Trace).

6.4 Summary

While hPSC-CM tissues with simple geometry (e.g. monolayer or spheroidal clusters) offer the high-throughput capabilities to screen for cardioactivity, there is still a need for organoids that recapitulate the pumping functions of the heart. A subset of cardioactive compounds elicit their effects the most pronounced at the organ level. The COC developed by the Costa group offers a solution as the organoid chamber exhibits positive stroke work and the Frank-Starling mechanism. In this chapter, we have preliminarily shown that the brightfield approach with optical flow (previously used for monolayer cultures) can be applied to videos of COC. The optical flow vectors can capture changes to the way COC pumps with spatial resolution, which the one dimensional pressure readouts cannot provide. This capability provides a potential method to screen for compounds (e.g. dromotropic compounds) that perturb electrical propagation across the cardiac surface. However, the brightfield approach with optical flow still needs to be optimized for COC videos. Through the analysis of other COC videos, the high frame rate of 100 fps is very sensitive to environmental noise (surrounding vibrations) and granularity in images (imbalance between light source, camera gain, and quality of camera sensors). As optical flow assumes constant brightness, videos of COCs should be taken in a standardized manner, such as consistent light sources, set working distance between lens and object, and a space that minimizes vibrations (e.g. optical table). With this standardization, the brightfield approach can be utilized on the COC videos to provide information-rich readouts for the screening of cardioactivity.

CHAPTER 7: Summary and future work

7.1 Summary of the work

In this work, we present a strategy to create a platform for enhanced detection of drug induced-cardiotoxicity with human pluripotent stem cell-derived cardiomyocytes (hPSC-CMs). We provide both hardware- and software-based solutions that address pitfalls that current platforms experience. To monitor the behavior of hPSC-CMs exposed to cardioactive compounds, we incorporated a brightfield technique that leverages optical flow to quantify videos of cardiomyocytes beating (Chapter 2). This combined approach is non-invasive, allowing for longitudinal studies, and it requires minimal equipment. As hPSC-CMs express a fetal-like phenotype, we propose a biomimetic substrate to align cells along the substrate's anistropic wrinkled surfaces (Chapter 3). The alignment of cardiomyocytes has been shown to invoke phenotypes more similar to the native myocardium. hPSC-CMs seeded on the wrinkled substrates demonstrated a more sensitive response to cardioactive compounds. In consideration of commercial use, the substrates were adapted for high-throughput capacity by patterning multiple islands of cardiomyocytes that act as independent samples within a single surface (Chapter 4). In order to analyze the complex yet rich data provided by screening platforms, a holistic approach in supervised machine learning was implemented (Chapter 5). Machine learning has the advantage of simultaneously evaluating multiple parameters and any underlying relationships. Utilizing both binary and multi-class SVM, we have developed a suite of tools that can determine an unknown compound's level of cardioactivity, predict its cardioactive mechanism and report its drug response relationship to other compounds. Finally, we further demonstrate the flexibility of the brightfield technique by analyzing videos of a 3D tissue model, cardiac organoid chamber (Chapter 7). The optical flow vectors provide spatial information

regarding the organoid's pumping, which can be crucial in screening compounds that disrupt the electrical propagation across cardiac surfaces.

7.2 Concluding remarks

In this dissertation, hardware and software components were designed to resolve various challenges of current screening platforms that employ hPSC-CMs. All of the components are modular such that they can be easily and independently applied to existing platforms for improved detection of drug-induced cardiotoxicty. At the same time, these components can and should be integrated into a single system to collectively leverage each component's advantages. If the system were to be created, it should be constructed as an organ-on-a-chip that can be easily connected to chips that model other organs within a single network. One of the major reasons for drug-induced cardiotoxicty in market approved drugs is unexpected rises in serum levels of unmetabolized compounds. Typically, the body is able to metabolize a compound via isozymes found in the liver, kidney, skin, gastrointestinal tract and lungs. However, when a patient is taking multiple medications, drugs can compete for the same enzyme receptor site and therefore cause elevated concentrations in circulation.[120] For example, mibefradil was withdrawn due to its potentially fatal drug-drug interactions with 25 other medications. Through the competition of cytochrome P450 3A, increased concentration of mibefradil resulted in the prolongation of the QT interval and the possibility of cardiotoxicity-related deaths. With a network of organ-on-a-chips, it may be feasible to predict drug-drug interactions and estimate therapeutic windows in an *in vivo* setting, leading to better preclinical detection of drug-induced cardiotoxicity.

Through the emergence of various methodologies to monitor hPSC-CM behavior when exposed to cardioactive compounds, it has become evident that in order to accurately predict a

compound's *in vivo* cardiotoxic effects, a consortium of platforms examining different aspects or phenotypes (e.g electrophysiology, contractility, or cell shape) of cardiomyocytes will be required.[75,104,121] This concerted effort is due to the various ways drug-induced cardiotoxicity occurs. The work in this dissertation has referred to some of these ways, ranging from drug-drug interaction to manifestation of cardioactive effects on the organ level through the perturbation of pumping mechanisms. The presented machine learning approaches can be used on different forms of signals (e.g calcium transients, MEA and optical recordings) and has the potential to integrate data of multiplex systems or even those across platforms. Moreover, machine learning can be utilized on a grander scale by incorporating past clinical data to determine the optimal combination of *in vitro* and *in silico* data for the prediction of drug-induced cardiotoxicity in patients.

Lastly, a key advantage of using stem cell-derived cardiomyocytes is the opportunity for personalized medicine. Specifically, chemotherapeutic agents, such as doxorubicin and the anthracycline family, can cause cardiotoxicity that is irreversible and cumulative dose-dependent.[122] However, the cardiotoxic effects of such agents vary from person to person. Dr. Joseph Wu's research group has recently shown that patient induced stem cell-derived cardiomyocytes were able to recapitulate the prevalence of doxorubicin-induced cardiotoxicity that matched patients' clinical data.[123] The ability to asses a compound's propensity to induce carditoxicity in a specific patient will allow physicians to create a custom theraputic regimen best suited for each patient. The methods proposed in this dissertation can be readily applied to create a high-throughput platform suitable for personalized medicine, as well.

References

1. Pharmaceutical Research and Manufacturers of America. *2013 Biopharmaceutical Research Industry Profile*. (2013).
2. Shah, R. R. Can pharmacogenetics help rescue drugs withdrawn from the market? *Pharmacogenomics* **7,** 889–908 (2006).
3. Om, A., Agarwal, T., Antakia, R., Shariff, U. & Rl, N. Cisapride for Intestinal Constipation (Review). *Cochrane Database Syst. Rev.* 1–37 (2011).
4. Dick, E., Rajamohan, D., Ronksley, J. & Denning, C. Evaluating the utility of cardiomyocytes from human pluripotent stem cells for drug screening. *Biochem. Soc. Trans.* **38,** 1037–45 (2010).
5. Itzhaki, I. *et al.* Modelling the long QT syndrome with induced pluripotent stem cells. *Nature* **471,** 225–9 (2011).
6. Kehat, I. *et al.* Human embryonic stem cells can differentiate into myocytes with structural and functional properties of cardiomyocytes. *J. Clin. Invest.* **108,** 407–14 (2001).
7. Schaaf, S. *et al.* Human engineered heart tissue as a versatile tool in basic research and preclinical toxicology. *PLoS One* **6,** (2011).
8. Song, L.-S. *et al.* Calcium biology of the transverse tubules in heart. *Ann. N. Y. Acad. Sci.* **1047,** 99–111 (2005).
9. Passier, R., Denning, C. & Mummery, C. Cardiomyocytes from human embryonic stem cells. *Handb. Exp. Pharmacol.* **174,** 101–122 (2006).
10. Stoelzle, S. *et al.* State-of-the-Art Automated Patch Clamp Devices: Heat Activation, Action Potentials, and High Throughput in Ion Channel Screening. *Front. Pharmacol.* **2,** (2011).
11. Malboubi, M. & Jiang, K. in *Gigaseal Formation in Patch Clamping with Application in Nanotechnology* 3–16 (Springer Berlin Heidelberg, 2014).
12. Yajuan, X., Xin, L. & Zhiyuan, L. A comparison of the performance and application differences between manual and automated patch-clamp techniques. *Curr. Chem. Genomics* **6,** 87–92 (2012).
13. Herron, T. J., Lee, P. & Jalife, J. Optical imaging of voltage and calcium in cardiac cells & tissues. *Circ. Res.* **110,** 609–23 (2012).
14. Bursac, N., Kirkton, K. R. D., C, M. L. & Liau, B. Characterizing functional stem cell–cardiomyocyte interactions. *Regen. Med.* **5,** 1–29 (2010).
15. McCombs, J. E. & Palmer, A. E. Measuring calcium dynamics in living cells with genetically encodable calcium indicators. *Methods* **46,** 152–9 (2008).
16. Navarrete, E. G. *et al.* Screening Drug-Induced Arrhythmia Events Using Human Induced Pluripotent Stem Cell-Derived Cardiomyocytes and Low-Impedance Microelectrode Arrays. *Circulation* **128,** S3–S13 (2013).
17. Clements, M. & Thomas, N. High-throughput multi-parameter profiling of electrophysiological drug effects in human embryonic stem cell derived cardiomyocytes using multi-electrode arrays. *Toxicol. Sci.* **140,** 445–61 (2014).
18. Peters, M. F., Lamore, S. D., Guo, L., Scott, C. W. & Kolaja, K. L. Human Stem Cell-Derived Cardiomyocytes in Cellular Impedance Assays: Bringing Cardiotoxicity Screening to the Front Line. *Cardiovasc. Toxicol.* (2014).
19. Xi, B. *et al.* Functional cardiotoxicity profiling and screening using the xCELLigence RTCA Cardio System. *J. Lab. Autom.* **16,** 415–21 (2011).
20. Grosberg, A., Alford, P. W., McCain, M. L. & Parker, K. K. Ensembles of engineered cardiac tissues for physiological and pharmacological study: heart on a chip. *Lab Chip* **11,** 4165–73 (2011).
21. Boudou, T. *et al.* A microfabricated platform to measure and manipulate the mechanics of engineered cardiac microtissues. *Tissue Eng. Part A* **18,** 910–9 (2012).
22. Liu, X., Iyengar, S. G. & Rittscher, J. Monitoring cardiomyocyte motion in real time through image registration and time series analysis. *IEEE Int. Symp. Biomed. Imaging From Nano to*

Macro 1308–1311 (2012).
23. Hossain, M. M. *et al.* Non-invasive characterization of mouse embryonic stem cell derived cardiomyocytes based on the intensity variation in digital beating video. *Analyst* **135,** 1624–30 (2010).
24. Ahola, A. *et al.* Video image-based analysis of single human induced pluripotent stem cell derived cardiomyocyte beating dynamics using digital image correlation. *Biomed. Eng. Online* **13,** 39 (2014).
25. Kim, S. B. *et al.* A cell-based biosensor for real-time detection of cardiotoxicity using lensfree imaging. *Lab Chip* **11,** 1801–7 (2011).
26. Maddah, M. & Loewke, K. Automated , Non-Invasive Characterization of Stem Cell-Derived Cardiomyocytes from Phase-Contrast Microscopy. *Med. Image Comput. Comput. Interv.* **17,** 57–64 (2014).
27. Hayakawa, T. *et al.* Noninvasive evaluation of contractile behavior of cardiomyocyte monolayers based on motion vector analysis. *Tissue Eng. Part C. Methods* **18,** 21–32 (2012).
28. Hayakawa, T. *et al.* Image-based evaluation of contraction-relaxation kinetics of human-induced pluripotent stem cell-derived cardiomyocytes: Correlation and complementarity with extracellular electrophysiology. *J. Mol. Cell. Cardiol.* **77,** 178–91 (2014).
29. Huebsch, N. *et al.* Automated Video-Based Analysis of Contractility and Calcium Flux in Human-Induced Pluripotent Stem-Derived Cardiomyocytes Cultured over Different Spatial Scales. *Tissue Eng. Part C. Methods* **21,** 1–13 (2014).
30. Maddah, M. *et al.* A Non-invasive Platform for Functional Characterization of Stem-Cell-Derived Cardiomyocytes with Applications in Cardiotoxicity Testing. *Stem cell reports* **4,** 621–631 (2015).
31. Tompkin, J. Optical Flow An Introduction. *Univ. Coll. London Comput. Sci. Dept., Mach. Vision-Practical* **2,** 1–13 (2008).
32. Fleet, D. J. & Weiss, Y. in *Mathematical Models in Computer Vision: The Handbook* 239–258 (Springer, 2005).
33. Horn, B. K. P. & Schunck, B. G. Determining optical flow. *Artif. Intell.* **17,** 185–203 (1981).
34. Sun, D., Roth, S. & Black, M. J. Secrets of optical flow estimation and their principles. *Proc. IEEE Comput. Soc. Conf. Comput. Vis. Pattern Recognit.* 2432–2439 (2010).
35. Chen, A. *et al.* Integrated platform for functional monitoring of biomimetic heart sheets derived from human pluripotent stem cells. *Biomaterials* **35,** 675–83 (2014).
36. Ringnér, M. What is principal component analysis? *Nat. Biotechnol.* **26,** 303–4 (2008).
37. Han, T. X. Computing Principal Components with the Eigen-decomposition of a Low Dimensional Matrix. **1,** 1–3
38. Veerman, C. C. *et al.* Immaturity of Human Stem-Cell-Derived Cardiomyocytes in Culture : Fatal Flaw or Soluble Problem ? **24,** (2015).
39. Robertston, C., Tran, D. D. & George, S. C. Concise Review: Maturation Phases of Human Pluripotent Stem Cell-Derived Cardiomyocytes. *Stem Cells* **31,** 1–17 (2014).
40. Xu, C., Police, S., Rao, N. & Carpenter, M. K. Characterization and Enrichment of Cardiomyocytes Derived From Human Embryonic Stem Cells. *Circ. Res.* **91,** 501–508 (2002).
41. Yang, X., Pabon, L. & Murry, C. E. Engineering Adolescence: Maturation of Human Pluripotent Stem Cell-Derived Cardiomyocytes. *Circ. Res.* **114,** 549–561 (2014).
42. Xu, X. Q., Soo, S. Y., Sun, W. & Zweigerdt, R. Global Expression Profile of Highly Enriched Cardiomyocytes Derived from Human Embryonic Stem Cells. *Stem Cells* **27,** 2163–2174 (2009).
43. Pillekamp, F. *et al.* Contractile Properties of Early Human Embryonic Beta-Adrenergic Stimulation Induces Positive Chronotropy and Lusitropy but Not Inotropy. *Stem Cells Dev.* **21,** 2111–2121 (2012).
44. Lundy, S. D., Zhu, W.-Z., Regnier, M. & Laflamme, M. A. Structural and Functional Maturation of Cardiomyocytes Derived from Human Pluripotent Stem Cells. *Stem Cells Dev.* **22,** 1991–2002 (2013).
45. Eng, G. *et al.* Autonomous beating rate adaptation in human stem cell-derived cardiomyocytes.

Nat. Commun. **7,** 1–10 (2016).
46. Nunes, S. S. *et al.* Biowire: a platform for maturation of human pluripotent stem cell-derived cardiomyocytes. *Nat. Methods* **10,** 781–7 (2013).
47. Ravenscroft, S. M., Pointon, A., Williams, A. W., Cross, M. J. & Sidaway, J. E. Cardiac Non-myocyte Cells Show Enhanced Pharmacological Function Suggestive of Contractile Maturity in Stem Cell Derived Cardiomyocyte Microtissues. *Toxicol. Sci.* **152,** 99–112 (2016).
48. Liu, J. *et al.* Facilitated maturation of Ca 2 + handling properties of human embryonic stem cell - derived cardiomyocytes by calsequestrin expression. *Am J Physiol Cell Physiol* **297,** 152–159 (2009).
49. Kim, D.-H. *et al.* Nanoscale cues regulate the structure and function of macroscopic cardiac tissue constructs. *Proc. Natl. Acad. Sci. U. S. A.* **107,** 565–70 (2010).
50. Pins, G. D., Christiansen, D. L., Patel, R. & Silver, F. H. Self-Assembly of Collagen Fibers. Influence of Fibrillar Alignment and Decorin on Mechanical Properties. *Biophys. J.* **73,** 2164–2172 (1997).
51. Lam, M. T., Chen, W. C. & Takayama, S. Reversible on-demand cell alignment using reconfigurable microtopography. *Biomaterials* **29,** 1705–1712 (2009).
52. Bettinger, C. J., Langer, R. & Borenstein, J. T. Engineering substrate topography at the micro- and nanoscale to control cell function. *Angew Chem Int Ed Engl* **48,** 5406–15 (2009).
53. Nathan, A. S., Baker, B. M., Nerurkar, N. L. & Mauch, R. L. Mechano-Topographic Modulation of Stem Cell Nuclear Shape on Nanofibrous Scaffolds. *Acta Biomater.* **7,** 57–66 (2012).
54. Chen, A. *et al.* Shrink-film configurable multiscale wrinkles for functional alignment of human embryonic stem cells and their cardiac derivatives. *Adv. Mater.* **23,** 5785–91 (2011).
55. Kita-matsuo, H. *et al.* Lentiviral Vectors and Protocols for Creation of Stable hESC Lines for Fluorescent Tracking and Drug Resistance Selection of Cardiomyocytes. *PLoS One* **4,** (2009).
56. Laflamme, M. A. *et al.* Cardiomyocytes derived from human embryonic stem cells in pro-survival factors enhance function of infarcted rat hearts. *Nat. Biotechnol.* **25,** 1015–1024 (2007).
57. Bray, M. P. *et al.* Nuclear morphology and deformation in engineered cardiac myocytes and tissues. *Biomaterials* **31,** 5143–5150 (2010).
58. Drew, N. K., Johnsen, N. E. & Core, J. Q. Multiscale Characterization of Engineered Cardiac Tissue Architecture. *J. Biomech. Eng.* **138,** (2016).
59. Zhou, Z. *et al.* Properties of HERG channels stably expressed in HEK 293 cells studied at physiological temperature. *Biophys. J.* **74,** 230–41 (1998).
60. Redfern, W. S. *et al.* Relationships between preclinical cardiac electrophysiology , clinical QT interval prolongation and torsade de pointes for a broad range of drugs : evidence for a provisional safety margin in drug development q. *Cardiovasc. Res.* **58,** 32–45 (2003).
61. Waldeck, B. B-Adrenoceptor agonists and asthma — 100 years of development. *Eur. Jounral Pharmacol.* **445,** 1–12 (2002).
62. Li, X., Zhang, R., Zhao, B., Lossin, C. & Cao, Z. Cardiotoxicity screening: a review of rapid-throughput in vitro approaches. *Arch. Toxicol.* **90,** 1803–1816 (2016).
63. Maddox, C. B., Rasmussen, L. & White, E. L. Adapting Cell-Based Assays to the High-Throughput Screening Platform: Problems Encountered and Lessons Learned. *JALA Charlottsv* **13,** 168–173 (2008).
64. Alom, S., Chen, C. S. & Chen, C. S. Microcontact printing : A tool to pattern. *Soft Matter* **3,** 1–11 (2007).
65. Reinhoudt, D. N. & Huskens, J. Microcontact Printing : Limitations and Achievements. *Adv. Mater.* **21,** 2257–2268 (2009).
66. Tan, J. L. *et al.* Simple Approach to Micropattern Cells on Common Culture Substrates by Tuning Substrate Wettability. *Tissue Eng.* **10,** (2004).
67. Ribeiro, A. J. S., Zaleta-rivera, K., Ashley, E. A. & Pruitt, B. L. Stable , Covalent Attachment of Laminin to Microposts Improves the Contractility of Mouse Neonatal Cardiomyocytes. *ACS Appl. Mater. Interfaces* **6,** 15516–15526 (2014).

68. Hillborg, H. *et al.* Crosslinked polydimethylsiloxane exposed to oxygen plasma studied by neutron reflectometry and other surface specific techniques. *Polymer (Guildf).* **41,** 6851–6863 (2000).
69. Chu, M., Nguyen, T. T., Lee, E. K., Morival, J. L. & Khine, M. Plasma free reversible and irreversible microfluidic bonding. *Lab Chip* **17,** 267–273 (2017).
70. Sirenko, O. *et al.* Multiparameter in vitro assessment of compound effects on cardiomyocyte physiology using iPSC cells. *J. Biomol. Screen.* **18,** 39–53 (2013).
71. Lu, H. R. *et al.* High throughput measurement of Ca++ dynamics in human stem cell-derived cardiomyocytes by kinetic image cytometery: A cardiac risk assessment characterization using a large panel of cardioactive and inactive compounds. *Toxicol. Sci.* **148,** 503–516 (2015).
72. Rodriguez, M. L. *et al.* Measuring the contractile forces of human induced pluripotent stem cell-derived cardiomyocytes with arrays of microposts. *J. Biomech. Eng.* **136,** 51005 (2014).
73. Bielawski, K. S., Leonard, A., Bhandari, S., Murry, C. E. & Sniadecki, N. Real-Time Force and Frequency Analysis of Engineered Human Heart Tissue Derived from Induced Pluripotent Stem Cells Using Magnetic Sensing. *Tissue Eng. Part C Methods* **22,** ten.TEC.2016.0257 (2016).
74. Huebsch, N. *et al.* Miniaturized iPS-Cell-Derived Cardiac Muscles for Physiologically Relevant Drug Response Analyses. *Sci. Reports* **6,** 1–12 (2016).
75. Dempsey, G. T. *et al.* Cardiotoxicity screening with simultaneous optogenetic pacing , voltage imaging and calcium imaging. *J. Pharmacol. Toxicol. Methods* **81,** 240–250 (2016).
76. Millard, D. C. *et al.* Identification of Drug–Drug Interactions In Vitro : A Case Study Evaluating the Effects of Sofosbuvir and Amiodarone on hiPSC-Derived Cardiomyocytes. *Toxicol. Sci.* **154,** 1–9 (2016).
77. Burges, C. J. C. A Tutorial on Support Vector Machines for Pattern Recognition. *Data Min. Knowl. Discov.* **2,** 121–167 (1998).
78. Ben-hur, A. & Weston, J. A User's Guide to Support Vector Machines. 1–18 (2012). Available at: http://pyml.sourceforge.net/doc/howto.pdf.
79. Berwick, R. An Idiot's guide to Support vector machines (SVMs) SVMs. (2003). Available at: http://www.cs.ucf.edu/courses/cap6412/fall2009/papers/Berwick2003.pdf.
80. Cristianini, N. Kernel Methods for General Pattern Analysis. (2007). Available at: http://www.kernel-methods.net/tutorials/KMtalk.pdf.
81. Fletcher, T. Support Vector Machines Explained. (2009). Available at: http://www.tristanfletcher.co.uk/SVM Explained.pdf.
82. Hather, C., Roquemore, L. & Thomas, N. High-content analysis of a live multiplexed cytotoxicity study using Cytiva ™ Cardiomyocytes and IN Cell Analyzer 2000. *Healthc. Life Sci. Newsl. - Discov. Matters* 13 (2011).
83. Olsen, C., Hesley, J. & Sirenko, O. High-Throughput Multiparameter. *Genet. Eng. Biotechnol. News* **33,** 36–37 (2013).
84. Soloveva, V., Larocque, J. & Mckillip, E. When Robots Are Good:Fully Automated Thermo LAS Robotic Assay System with Dual FLIPR TETRA and TAP SelecT Robotic Cell Culture System. *J. Assoc. Lab. Autom.* **11,** 145–156 (2006).
85. Okada, Y., Ogawa, S., Sadanaga, T. & Mitamura, H. Assessment of reverse use-dependent blocking actions of class III antiarrhythmic drugs by 24-hour Holter electrocardiography. *J. Am. Coll. Cardiol.* **27,** 84–9 (1996).
86. Kirsch, G. E. *et al.* Variability in the measurement of hERG potassium channel inhibition: effects of temperature and stimulus pattern. *J. Pharmacol. Toxicol. Methods* **50,** 93–101 (2004).
87. Haft, J. I. & Habbab, M. A. Treatment of Atrial Arrhythmias Effectiveness of Verapamil When Preceded by Calcium Infusion. *Arch. Intern. Med.* **146,** 1085–1089 (1986).
88. Mattiazzi, A. & A, G. Negative inotropic effect of verapamil, nifedipine and prenylamine and its reversal by calcium or isoproterenol. *Arch. Int. Physiol. Biochem.* **91,** 133–144 (1983).
89. Kovács, M., Tóth, J., Hetényi, C., Málnási-Csizmadia, A. & Sellers, J. R. Mechanism of blebbistatin inhibition of myosin II. *J. Biol. Chem.* **279,** 35557–63 (2004).
90. Rifkin, R. Multiclass Classification. (2008). Available at:

http://www.mit.edu/~9.520/spring09/Classes/multiclass.pdf.
91. Aisen, B. A Comparison of Multiclass SVM Methods. (2006). Available at: http://courses.media.mit.edu/2006fall/mas622j/Projects/aisen-project/.
92. Harris, K. *et al.* Comparison of electrophysiological data from human-induced pluripotent stem cell-derived cardiomyocytes to functional preclinical safety assays. *Toxicol. Sci.* **134,** 412–426 (2013).
93. Martin, R. L., Lee, J., Cribbs, L. L., Perez-reyes, E. & Hanck, D. A. Mibefradil Block of Cloned T-Type Calcium Channels 1. *J. Pharmacol. Exp. Ther.* **295,** 302–308 (2000).
94. Steinberg, S. F. The Molecular Basis for Distinct B-Adrenergic Receptor Subtype Actions in Cardiomyocytes. *Circ. Res.* **85,** 1101–1111 (1999).
95. Fearnley, C. J., Roderick, H. L. & Bootman, M. D. Calcium Signaling in Cardiac Myocytes. *Cold Spring Harb Perspect Biol* **3,** 1–20 (2011).
96. Katz, A. *et al.* Selectivity of digitalis glycosides for isoforms of human Na,K-ATPase. *J. Biol. Chem.* **285,** 19582–19592 (2010).
97. Ziupa, D. *et al.* Pronounced Effects of HERG-Blockers E-4031 and Erythromycin on APD , Spatial APD Dispersion and Triangulation in Transgenic Long-QT Type 1 Rabbits. *PLoS One* **9,** (2014).
98. Wong, B. S., Manabe, N. & Camilleri, M. Role of prucalopride, a serotonin (5-HT4) receptor agonist, for the treatment of chronic constipation. *Clin. Exp. Gastroenterol.* **3,** 49–56 (2010).
99. Brown, N. J. & Vaughan, D. E. Angiotensin-Converting Enzyme Inhibitors. *Circulation* **97,** 1411–1420 (1998).
100. Williams, G. H. Converting-enzyme inhibitors in the treatment of hypertension. *N. Engl. J. Med.* **319,** 1517–1525 (1988).
101. Weng, Z. *et al.* A Simple, Cost-Effective but Highly Efficient System for Deriving Ventricular Cardiomyocytes from Human Pluripotent Stem Cells. *Stem Cells Dev.* **23,** 1704–1716 (2014).
102. Serrao, G. W. *et al.* Myocyte-depleted engineered cardiac tissues support therapeutic potential of mesenchymal stem cells. *Tissue Eng. Part A* **18,** 1322–1333 (2012).
103. Lee, E. K., Kurokawa, Y. K., Tu, R., George, S. C. & Khine, M. Machine learning plus optical flow: a simple and sensitive method to detect cardioactive drugs. *Sci. Rep.* **5,** (2015).
104. Clements, M., Millar, V., Williams, A. S. & Kalinka, S. Bridging functional and structural cardiotoxicity assays using human embryonic stem cell-derived cardiomyocytes for a more comprehensive risk assessment. *Toxicol. Sci.* **148,** 241–260 (2015).
105. Scott, C. W. *et al.* An impedance-based cellular assay using human iPSC-derived cardiomyocytes to quantify modulators of cardiac contractility. *Toxicol. Sci.* **142,** 331–338 (2014).
106. Cerignoli, F. *et al.* High throughput measurement of Ca^{2+} dynamics for drug risk assessment in human stem cell-derived cardiomyocytes by kinetic image cytometry. *J. Pharmacol. Toxicol. Methods* **66,** 246–56 (2012).
107. Harmer, A. R. *et al.* Validation of an in vitro contractility assay using canine ventricular myocytes. *Toxicol. Appl. Pharmacol.* **260,** 162–172 (2012).
108. Guo, L. *et al.* The Electrophysiological Effects of Cardiac Glycosides in Cardiomyocytes and in Guinea Pig Isolated Hearts. *Cell. Physiol. Biochem.* **27,** 453–462 (2011).
109. Puppala, D. *et al.* Comparative gene expression profiling in human-induced pluripotent stem cell-derived cardiocytes and human and cynomolgus heart tissue. *Toxicol. Sci.* **131,** 292–301 (2013).
110. Guo, L. *et al.* Refining the Human iPSC-Cardiomyocyte Arrhythmic Risk Assessment Model. **136,** 581–594 (2013).
111. Peters, M. F., Scott, C. W., Ochalski, R. & Dragan, Y. P. Evaluation of Cellular Impedance Measures of Cardiomyocyte Cultures for Drug Screening Applications. **10,** 525–532 (2012).
112. Reif, D. M. *et al.* ToxPi GUI: An interactive visualization tool for transparent integration of data from diverse sources of evidence. *Bioinformatics* **29,** 402–403 (2013).
113. Pointon, A. *et al.* High-Throughput Imaging of Cardiac Microtissues for the Assessment of Cardiac Contraction during Drug Discovery. *Toxicol. Sci.* **155** (2016).

114. Pointon, A. *et al.* Assessment of cardiomyocyte contraction in human-induced pluripotent stem cell-derived cardiomyocytes. *Toxicol. Sci.* **144,** 227–237 (2015).
115. Lancaster, M. C. & Sobie, E. A. Improved Prediction of Drug-Induced Torsades de Pointes Through Simulations of Dynamics and Machine Learning Algorithms. *Clin. Pharmacol. Ther.* **100,** 371–379 (2016).
116. Taboureau, O. & Jørgensen, F. S. In Silico Predictions of hERG Channel Blockers in Drug Discovery : From Ligand-Based and Target-Based Approaches to Systems Chemical Biology. *Comb. Chem. High Throughput Screen.* **14,** 375–387 (2011).
117. Bryant, B. & Knights, K. *Pharmacology for Health Professionals*. (Mosby Australia, 2010).
118. Zipes, D. P. & Wellens, H. J. Sudden Cardiac Death. *Circulation* **98,** 2334–2351 (1998).
119. Lee, E. J., Kim, D. E., Azeloglu, E. U. & Costa, K. D. Engineered cardiac organoid chambers: toward a functional biological model ventricle. *Tissue Eng. Part A* **14,** 215–25 (2008).
120. Ogu, C. C. & Maxa, J. L. Drug interactions due to cytochrome P450. *BUMC Proc.* **13,** 421–423 (2000).
121. Sheehy, S. P. *et al.* Quality metrics for stem cell-derived cardiac myocytes. *Stem Cell Reports* **2,** 282–294 (2014).
122. Menna, P. & Salvatorelli, E. Primary Prevention Strategies for Anthracycline Cardiotoxicity : A Brief Overview. *Chemotherapy* **62,** 159–168 (2017).
123. Burridge, P. W. *et al.* Human induced pluripotent stem cell–derived cardiomyocytes recapitulate the predilection of breast cancer patients to doxorubicin-induced cardiotoxicity Paul. *Nat. Med.* **22,** (2016).